12-2003

Directional Solidification, Microstructures and Mechanical Properties of Cr-Cr3Si Eutectic Alloys

Hongbin Bei
University of Tennessee - Knoxville

To the Graduate Council:

I am submitting herewith a dissertation written by Hongbin Bei entitled "Directional Solidification, Microstructures and Mechanical Properties of Cr-Cr3Si Eutectic Alloys." I have examined the final electronic copy of this dissertation for form and content and recommend that it be accepted in partial fulfillment of the requirements for the degree of Doctor of Philosophy, with a major in Materials Science and Engineering.

George M. Pharr, Major Professor

We have read this dissertation and recommend its acceptance:

Easo P. George, Peter K. Liaw, Madhu S. Madhukar

Accepted for the Council:

Carolyn R. Hodges

Vice Provost and Dean of the Graduate School

(Original signatures are on file with official student records.)

To the Graduate Council:

I am submitting herewith a dissertation written by Hongbin Bei entitled "Directional Solidification, Microstructures and Mechanical Properties of Cr-Cr_3Si Eutectic Alloys". I have examined the final electronic copy of this dissertation for form and content and recommend that it be accepted in partial fulfillment of the requirements for the degree of Doctor of Philosophy, with a major in Materials Science and Engineering.

George M. Pharr

Major Professor

We have read this dissertation and
recommend its acceptance:

Easo P. George

Peter K. Liaw

Madhu S. Madhukar

Accepted for the Council:

Dr. Anne Mayhew

Vice Provost and
Dean of Graduate Studies

(Original signatures are on the file with official student records)

Directional Solidification, Microstructures and Mechanical Properties of Cr-Cr_3Si Eutectic Alloys

A Dissertation
Presented for the
Doctor of Philosophy Degree
The University of Tennessee, Knoxville

Hongbin Bei
December 2003

To my family and friends who have motivated and supported me throughout the completion of this dissertation.

Acknowledgment

I would like to express my sincere appreciation to my major professors Dr. George M. Pharr and Dr. Easo P. George for their scientific guidance, encouragement, and kindness throughout my graduate study and completion of this dissertation. The enormous inspiration and confidence which they gave me makes me believe that I can continue my academic dream. I am grateful to my committee members Dr. Peter K. Liaw and Dr. Madhu S. Madhukar for their constructive advice and enormous support. All of them, with their wisdom, experience, patience, and kindness, have been and will always be great mentors to me.

I am also grateful to my fellow graduate students and staff members in the Department of Materials Science and Engineering, The University of Tennessee, Knoxville, and the Metals and Ceramics Division, Oak Ridge National Laboratory for the wonderful time we spent together.

This research was sponsored by the Division of Materials Sciences and Engineering, Office of Basic Energy Sciences, U. S. Department of Energy, and the SHaRE Collaborative Research Center at Oak Ridge National Laboratory, under contract DE-AC05-00OR22725 with UT-Battelle, LLC.

Abstract

Alloys based on intermetallics have been considered for high temperature structural applications. However, many of these alloys suffer from intrinsic brittleness and low fracture toughness at ambient temperature. Therefore, ductile-phase-toughened intermetallic composites are being investigated as a means to improve the fracture toughness. A subset of this class of materials is in-situ composites produced by directional solidification of intermetallic eutectics. In this study, the Cr-Cr_3Si eutectic system is selected as a model system to investigate composites by directional solidification, where the strong, but brittle Cr_3Si is combined with a more ductile Cr-rich solid solution.

A series of binary Cr-Si alloys with silicon concentrations ranging from 13 to 24 at.% were produced by arc melting and drop casting. These compositions span the composition (15 at.% Si) at which a eutectic reaction is reported in the phase diagram. The microstructure of the Cr-16.05 at.% Si alloy is fully lamellar and devoid of any pro-eutectic phases suggesting that the best composition for obtaining a fully lamellar structure is Cr-16.05 at.% Si, rather than the eutectic composition (Cr-15 at.% Si) indicated in the phase diagram. The eutectic microstructure consists of alternating lamellae of Cr (solid solution) and Cr_3Si (intermetallic). Uniform and well-aligned lamellar structures were obtained over a fairly wide range of solidification conditions, but not at very low or very high growth rates where degenerate and cellular structures, respectively, were obtained. The lamellar spacing was found to increase with decreasing

solidification rate, in agreement with the Jackson-Hunt theory. In addition, for a fixed growth rate, the lamellar spacing was found to increase with increasing rotation rate. The growth directions in the lamellar eutectic were found to be <100> for the Cr_3Si phase and <111> for the Cr solid solution phase. Eutectic microstructures (rod or lamellar) could also be produced at off-eutectic compositions, but only for a limited range of growth conditions.

The mechanical properties of the individual lamellae and the Cr-Cr_3Si composites were examined by nanoindentation, Vicker's hardness testing and three-point bend testing. It was found that the Vicker's hardness of Cr-Cr_3Si composites is about HV847, independent of the lamellar spacing. The Young's modulus of the Cr-Cr_3Si eutectic composites measured by ultrasonic techniques is 312 GPa, which is in reasonably good agreement with the nanoindentation results (within ~5%). The fracture toughness of single crystals of Cr_3Si is very low (~2.6 MPa$\sqrt{m}$). Combination with a more ductile phase (Cr-rich solid solution) to make "ductile phase toughened" composites increases the fracture toughness to maximum 8.5 MPa$\sqrt{m}$. The fracture toughness of lamellar microstructures with fine spacings is slightly higher than that of microstructures with coarse spacings.

Table of Contents

List of Tables

List of Figures

Part One: An Overview of Directionally Solidified Intermetallic Composites for High-Temperature Structural Applications

1.1 Introduction

With advances in high temperature technology, the need for materials with superior strength, rigidity and ductility at elevated temperatures has been growing. Nickel-based superalloys [1-6] have been among the most widely used of such materials since the second world war. However, their high temperature capability is inherently limited by the melting points of nickel (1453ºC), and other lower melting constituents, such as Ni_3Al [7-10], which are the principal strengthening phases in Ni-based superalloys. To meet the challenge of higher operation temperatures, alloys based on refractory intermetallics with melting points $T_m > 1600$ºC have recently been investigated, several of which have attractive properties for elevated temperature structural applications, including good oxidation resistance and creep strength [11-24]. However, many of these intermetallic compounds suffer from intrinsic brittleness and low fracture toughness at ambient temperature. Therefore, ductile-phase-toughened intermetallic composites have been investigated as a way to improve the fracture toughness. A subset of this class of materials is in-situ composites [19-24].

In-situ composites are multi-phase materials where the reinforcing phase is synthesized during composite fabrication, in contrast to ex-situ composites where the reinforcing phase is produced separately and then introduced into the matrix during a subsequent processing step such as infiltration or powder processing [25]. There are a number of processes for producing in-situ composites, which can be divided broadly into two groups depending on whether the reinforcements first appear in the liquid or solid state [26]. Solid-state in-situ processes include internal oxidation [27], displacement

reaction [28], reactive milling [29], mechanical alloying [30], and cryomilling [31]. The well known eutectoid reaction in steels can also be considered an in-situ solid state reaction with cementite acting as the reinforcement and ferrite as the matrix. Liquid-state processes include rapid solidification [32-36], traditional casting, and directional solidification of eutectic alloys. We restrict our discussion here to just one of these processes, namely directional solidification of eutectics.

The role of eutectics in the development of ductile phase toughened intermetallic composites has been discussed by Mazdiyasni and Miracle [37]. They listed several advantages of producing in-situ composites by directional solidification of eutectics, specifically: directional solidification allows components to be produced from the melt in a single stage process; there is intrinsic thermodynamic stability and chemical compatibility between the matrix and reinforcements; and the microstructure can be controlled over a wide range, from well-aligned lamellae to finely dispersed particles or fibers, by adjusting the solidification conditions [21-24, 37-40]. In their work [37], several eutectic systems (e.g., Cr-Cr_2Zr, Cr-Cr_2Hf, Cr-Cr_2Ta, Cr-Cr_3Si, Ta-Cr_2Ta and Ta-Ta_5Si) were surveyed as potential materials for high temperature applications.

Directional solidification of binary or pseudo-binary eutectics can produce well-aligned regular structures consisting of fibrous (rod-like) or lamellar constituents. Such structures may offer substantial increases in high-temperature strength, fracture properties, or creep resistance over those of conventionally cast alloys. Therefore, directionally solidified high-temperature eutectics are possible candidates for the eventual replacement of superalloys.

1.2 Candidate eutectics for high temperature applications

A primary requirement for many high temperature structural applications is adequate oxidation resistance at temperatures above 1000ºC. Therefore, attention has been focused on those alloys that have high concentrations of aluminum, chromium and silicon, since these elements have been shown to produce protective oxide scales of alumina, chromia, and silica, respectively [41]. To achieve useful strengths at temperatures of 1000-1600ºC, melting points in excess of 1600ºC are required. Most materials retain significant strength to approximately 0.5-0.6 of their absolute melting temperature, T_m. Using this criterion, Anton et al. [41] examined intermetallic compounds that have melting temperatures of 1600-2700ºC, and concluded that materials based on the *C*14/*C*15 structure (Laves phase, e.g., Cr_2Nb and Cr_2Ta), *A*15 structure (e.g., Cr_3Si and Nb_3Al), $D8_8$ structure (sigma phase, e.g., Ti_5Si_3), *A*12 structure (α-Mn phase, e.g., Re_3Nb) and Nb alloys are potential candidates for high temperature structural applications.

Table 1-1 lists several eutectic systems having melting points higher than 1600ºC that have been studied recently as candidate materials. Some of these alloys have densities that are lower than those of currently used Ni-based superalloys (typically, around 8 g/cm^3 [42]), which gives them an advantage in aerospace applications, especially in rotating parts such as turbine blades or disks, where the strength to density ratio is important.

Table 1-1. Binary eutectics having melting points T_m > 1600 ºC that have been recently investigated.

Binary eutectic	*Crystal structure*	T_E [2] *(ºC)*	C_E [3] *(at.%)*	*Density of intermetallic*[4]	*Expected structure*	*Observed structure*	*Ref.*
Cr-Cr_3Si	*A*2-*A*15	1705	15.0 Si	6.5 g/cm^3	Lamellar	Lamellar	15, 24
V-V_3Si	*A*2-*A*15	1870	13.0 Si	5.7 g/cm^3	Lamellar	Rod	15
Nb-Nb_3Si[1]	*A*2-*L*1_2	1883	18.7 Si	7.3 g/cm^3	Lamellar/rod	Lamellar/rod	15
Hf-Hf_2Si[1]	*A*2-*C*16	2050	10.0 Si	11.7 g/cm^3	Rod	-	-
Mo_5Si_3-$MoSi_2$	$D8_m$-$C11_b$	1900	54.0 Si	8.12-6.3g/cm^3	Lamellar	Lamellar	43
Cr-Cr_2Ta[1]	*A*2-*C*14	1760	13.0 Si	11.2 g/cm^3	Lamellar	Lamellar/rod	44
Cr-Cr_2Hf[1]	*A*2-*C*14	1665	13.0 Hf	10.2 g/cm^3	Lamellar	-	-
Cr-Cr_2Nb[1]	*A*2-*C*14	1620	12.0 Nb	7.6 g/cm^3	Lamellar/rod	-	-
Nb-Cr_2 Nb[1]	*A*2-*C*14	1650	50.0 Cr	7.6 g/cm^3	Lamellar/rod	Lamellar	12
Ru-RuAl	*A*3-*B*2	1920	30.0 Al	8.3 g/cm^3	Lamellar	Lamellar	45

[1] *Intermetallic phase undergoes phase transformation during cooling.*

[2] *T_E – Eutectic temperature*

[3] *C_E – Eutectic composition from phase diagram [46]*

[4] *All densities are from the ASTM Powder Diffraction File (PDF).*

1.3 Microstructure morphology

The microstructures of binary eutectic alloys can exhibit a wide variety of geometrical arrangements of the two constituent phases. In general, the eutectic structure will exhibit a regular morphology (rod-like or lamellar) if both phases possess a low entropy of fusion, typically, $\Delta S/R_g < 2$, where ΔS is the entropy of fusion and R_g is the gas constant [47]. The relative stabilities of the lamellar and rod-like structures have been discussed in detail by Jackson and Hunt [48] and Hillert [49]. When the volume fractions (V_f) of the two eutectic phases are approximately the same ($0.3 < V_f < 0.5$), which is encouraged by a phase diagram that is symmetrical about the eutectic composition, there is a preference for the formation of lamellar structures. However, the total interface energy is less for a rod-like morphology (compared to the lamellar morphology) if the difference in the volume fractions of the two phases is large (i.e., if one of the phases has $V_f > 70\%$). In such cases, a rod-like structure is preferred with the major phase becoming the continuous matrix and the minor phase the discontinuous rods. Figure 1-1 schematically shows regular eutectic structures: lamellar and rod-like .

A fully eutectic structure, devoid of any cellular and dendritic regions, can be obtained not only in alloys having the exact eutectic composition but also at off-eutectic compositions if the growth conditions are carefully selected. This is of interest because it can be used to control the relative volume fractions of the constituent phases and, therefore, the properties of the composite. In order to obtain eutectic-like structures in off-eutectic alloys one has to maintain a stable, planar solid-liquid interface during directional solidification. According to the theory of constitutional supercooling, the

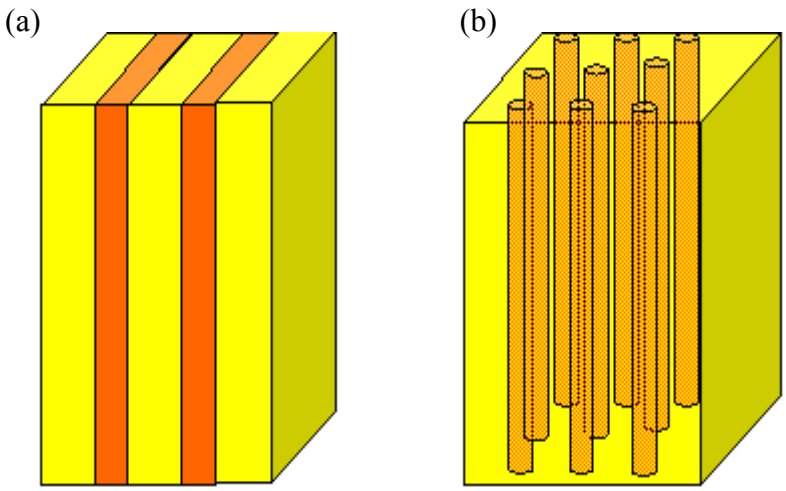

Figure 1-1. Schematic representations of (a) lamellar and (b) rod-like eutectic structures.

growth condition for producing such an interface, in the absence of convection, is

$$\frac{G_L}{R} \geq -\frac{m_L (C_E - C_0)}{D} \qquad (1\text{-}1)$$

where G_L is the temperature gradient in the liquid ahead of the interface, m_L is the slope of the liquidus, C_E is the eutectic composition, C_0 is the initial composition of the solidifying alloy, and D is the solution diffusion coefficient [45, 50]. For a given alloy, the right hand side of Eq. 1-1, which consists entirely of material parameters, is a constant. Similarly, for a given directional solidification system, the temperature gradient is a constant. Therefore, the only variable parameter is the growth rate, R, which has to be as slow as possible to favor a planar liquid-solid interface.

1.4 Effects of solidification parameters on interphase spacing

Regular eutectic growth depends on an interplay between the diffusion required for phase separation and the energy required for the formation of interphase boundaries. The interphase spacing is the result of a balance between two competing tendencies: on the one hand, to minimize the interphase spacing in order to shorten the diffusion path in the liquid near the interface, and on the other hand, to increase the spacing to minimize the interfacial area and hence the total interfacial energy. The most comprehensive treatment of this balance is that by Jackson and Hunt [48]. Under maximum growth velocity assumptions, they obtained the following relationship between growth rate, *R,* and interphase spacing, λ, for both lamellar and rod-like eutectic structures:

$$\lambda^2 R = constant \qquad (1\text{-}2)$$

where the constant is related to the magnitudes of the liquidus slopes at the eutectic temperature, the composition difference between the two phases, their volume fractions, the solid-liquid interface energies of the two phases, and the liquid–solid interface shape.

The dependence of lamellar spacing on growth rate has been found to be in agreement with the Jackson-Hunt theory in the Ni-Ni_3Si eutectic [51], although this eutectic system is not considered a candidate for high temperature applications because its melting point T_m is only about 1300ºC. In the case of ternary eutectic systems, Rios et al. [52] have directionally solidified Nb-Al-Ni eutectic alloys (T_m = ~1550ºC), and rod-like microstructures with three different phases (Al_3Nb, Nb_2Al and AlNbNi) were observed with the interphase spacing λ again decreasing with increasing solidification rate.

The influence of fluid convection is not included in the Jackson-Hunt theory. However, there is usually forced convection in the molten zone during solidification, especially during directional solidification of materials with high melting points using the floating zone technique in which specimen rotation is employed to ensure uniform heating and homogeneous composition [39]. Limited theoretical analyses and experimental studies have shown that convective flow results in a change of the eutectic spacing during directional solidification. Quenisset *et al.* [53,54] obtained a theoretical solution for the effect of convection on the eutectic spacing as follows:

$$\lambda^2 R = \frac{A}{1 - BG_u\lambda^2 / D} \qquad (1\text{-}3)$$

where G_u is the gradient of flow velocity, A and B are constants, and D is the solution diffusion coefficient. Their analysis was for an ideal system in which the volume fractions of the two eutectic phases are the same, i.e., $V_f = 0.5$. Baskaran and Wilcox [55] and Chandrasekhar *et al.* [56] extended the analysis for alloys in which the eutectic phases have significantly different volume fractions and obtained the following result:

$$\frac{\lambda}{\lambda_0} = 1 + A'\varepsilon_0^2 \qquad \text{for } V_f = 0.1 \sim 0.5 \qquad (1\text{-}4)$$

where $\varepsilon_0 = G_u\lambda_0^2 / D$, λ_0 is the eutectic spacing without convection, and A' is a constant.

Because the gradient of flow velocity is proportional to the rotation speed [57], the above theoretical analyses predict that the interphase spacing increases with increasing rotation speed. This prediction has been verified in the Ti-Ti_5Si_3 eutectic systems[39].

1.5 Mechanical behavior

The mechanical behavior of conventional composite materials reinforced by relatively large wires or fibers (~100 μm diameter) can be modeled by considering the load partitioned between the matrix and the reinforcing phases in proportion to their volume fractions. In contrast, the much finer microstructures (~1 μm) associated with in-situ composites can lead to substantial additional, or indirect strengthening. This indirect strengthening has been explained with the help of continuum models and dislocation density effects (e.g., single dislocation-particle interaction models, multiple dislocation-particle interaction models and forest hardening models), as discussed in detail in refs. [25,58].

Even without the additional strengthening effect of the composite, many intermetallic compounds by themselves offer high strength and good creep resistance at elevated temperature. For example, Shah and Anton [59] evaluated refractory intermetallics having the *A*15 structure (e.g., Cr_3Si) and found a significant (200ºC) advantage over superalloys in terms of creep strength. Table 1-2 lists the microhardness and elastic modulus of several intermetallic compounds with high melting points. Most of these materials have very high hardness and elastic modulus, reflecting the strong interatomic bonding in these materials. However, a critical disadvantage is their intrinsic brittleness at low temperatures. Combining them with a ductile phase to produce "ductile-phase-toughened" in-situ composites [19-24], therefore, has been the focus of attempts to improve the damage tolerance of high-temperature intermetallics at low temperatures.

Table 1-2. Hardness, Young's modulus, and brittle-ductile transition temperature of monolithic intermetallics with high melting points.

Intermetallic	T_m (*°C*)	*Hardness (HV)*	*Modulus E (GPa)*	T_{bd}*	*Ref.*
Cr_3Si	1770	1200	351	>1200	60
V_3Si	1870	1250	213	~1200	61,62
Mo_3Si	2025	1285	300	1000	63
Mo_2Si	2030	800	430	-	63
Mo_5Si_3	2180	1200	~300	1250	64
Cr_2 Zr	1760	800	166	-	65
Cr_2Ta	2020	-	175	-	66
Cr_2Nb	1620	1000	218	-	61
RuAl	2060	310	267	-	61
Nb_3Al	1960	910	-	~1000	67

* *T_{bd} – Brittle-ductile transition temperature.*

This contrasts with the approach in traditional metal matrix composites where the principal goal often is to enhance strength with the help of fiber reinforcements.

The results of three point bend tests show that the fracture toughness of single-phase V_3Si can be significantly improved by incorporating a ductile V solid solution in the microstructure by directional solidification of V-V_3Si eutectic alloys [68]. The fracture toughness of V-V_3Si composites depends on their microstructure and interstitial impurity content. For eutectic composites containing nearly equal volume fractions of the continuous ductile V solid solution phase and discontinuous V_3Si rods, fracture toughnesses of over 20 MPa√m have been reported, a significant increase when compared to that of the V_3Si single phase (~1.3 MPa √m). Similar improvements in fracture toughness have been realized in Nb-Nb_5Si_3 in-situ composites, where the ductile phase is (Nb) particles [69].

In addition to interspersing ductile metal layers between the brittle intermetallic layers to enhance toughness, it is important also to improve the properties of the ductile phase itself. The use of body-center cubic metals as the ductile phase in many in-situ intermetallic composites (e.g., V, Cr, Nb and Hf in Table 1-1) requires a better understanding of the factors contributing to the toughness of the ductile phase, including the role of interstitials and the effects of constraint on the evolution of stresses [70-72].

1.6 Cr-Cr_3Si eutectic system

The intermetallic compound Cr_3Si has been identified as a promising candidate for high temperature structural applications in aggressive environments because of

several desirable properties, e.g., high melting point, good oxidation resistance, high strength and hardness, as well as relatively low density [11-18]. However, its application is limited by its intrinsic brittleness and low fracture toughness at temperatures below 1200°C caused by insufficient slip systems due to its complicated *A*15 crystal structure [18]. Therefore, in the present study the Cr-Cr_3Si eutectic system was selected to produce ductile phase toughened Cr_3Si composites by directional solidification, where the strong, but brittle Cr_3Si can be combined with a ductile solid solution. As can be seen from the binary Cr-Si phase diagram (Fig. 1-2), a eutectic reaction occurs at around 15 at.% Si [46]. Therefore, an alloy with this composition, upon solidification from the melt, should have a microstructure that consists of Cr (solid solution) and Cr_3Si (intermetallic). It should be noted, however, that the liquidus lines on either side of the eutectic are dotted indicating that there is some uncertainty about the true eutectic composition.

For the Cr-Cr_3Si system, both the Cr-rich phase and Cr_3Si have low entropies of fusion ($\Delta S(Cr)$ is 6.5 J/K mole and $\Delta S(Cr_3Si)$ is 15.3 J/K mole [73]), and the volume fractions of both phases are close to 0.5 [46]. Hence regular lamellar structures are predicted under optimal growth conditions. Previous work using the Czochralski cold-crucible crystal growth system has shown the feasibility of producing well-aligned lamellar structures of Cr-Cr_3Si [15, 24]. Therefore, the Cr-Cr_3Si system was chosen as a model system to study the relationships among processing parameters, microstructures, thermal stability and mechanical behavior and hence obtain a fundamental understanding of in-situ lamellar eutectic composites. Several Cr-Cr_3Si alloys with different compositions were directionally solidified by changing the solidification conditions

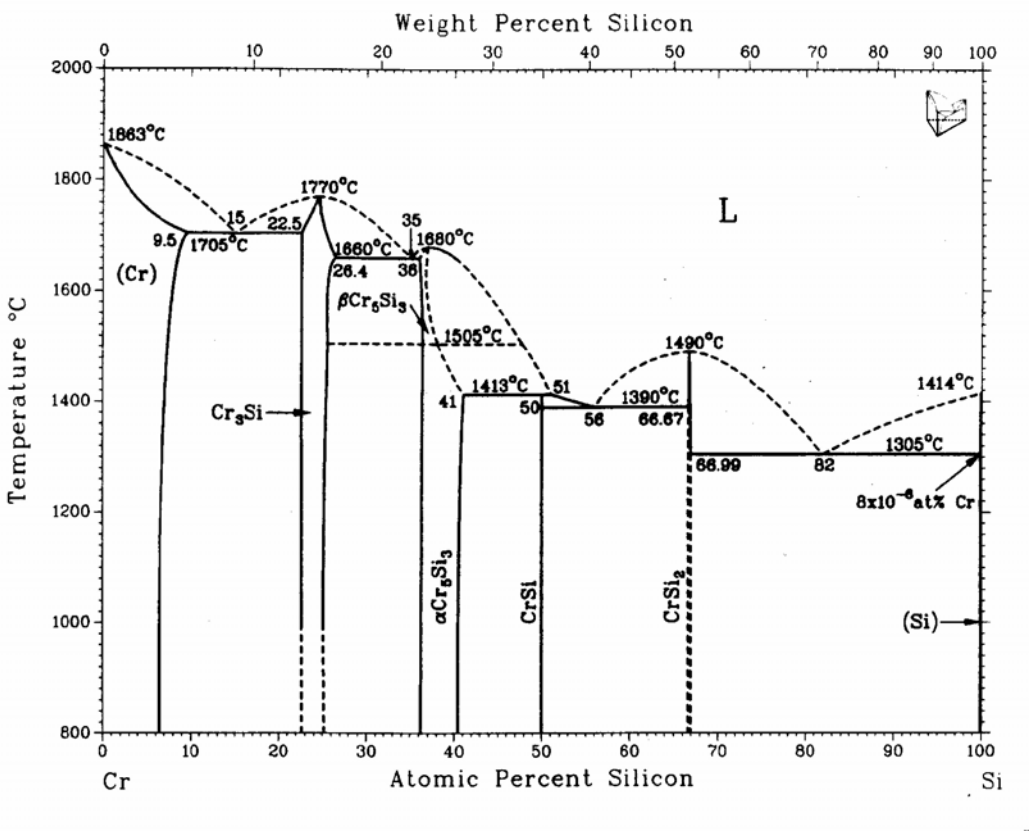

Figure 1-2. The Cr-Si phase diagram[46].

(namely growth rate and specimen rotation rate) in an optical floating zone furnace to study how the composition of the alloy and the solidification conditions affect the microstructures. Additional investigations were carried out on the orientation relationships between the lamellae, the mechanical properties of the individual lamellae as well as the overall composites, and their microstructural stability.

References:

1. F. L. Versnyder and R. W. Guard, *Transactions of the Metallurgical Society of AIME* 52 (1960) 485.
2. F. E. Heredia and D. P. Pope, in Superalloys 1988, S. Reichman, D.N. Duhl, G. Maurer, S. Antolovitch and C. Lund, editors, (The Minerals Metals and Materials Society, Warrendale, 1988) p. 315.
3. S. S. Babu, M. K. Miller, J. M. Vitek and S. A. David, *Acta Materialia* 49 (2001) 4149.
4. J. M. Vitek, S. A. David and L. A. Boatner, *Science and Technology of Welding and Joining* 2 (1997) 109.
5. R. Jayaram; M. K. Miller, *Acta Metallurgica et Materialia* 43 (1995) 1979.
6. M. K. Miller, R. Jayaram, L. S. Lin and A. D. Cetel, *Applied Surface Science* 76 (1994) 172.
7. J. K. Tien and R. P. Gamble, *Materials Science and Engineering* 8 (1971) 152.
8. A. K. Bhambri, T. Z. Kattamis and J. E. Morral, *Metallurgical Transactions B* 6 (1975) 523.
9. C. T. Liu, in Structural Intermetallics, R. Darolia, J. J. Lewandowski, C. T. Liu, P. L. Martin, D. B. Miracle and M. V. Nathal, editors, (The Minerals, Metals & Materials Society, Warrendale, 1993) p. 365.
10. E. P. George and C. T. Liu, in Structural Intermetallics 1997, M. V. Nathal, R. Darolia, C. T. Liu, P. L. Martin, D. B. Miracle, R. Wagner and M. Yamaguchi, editors, (The Minerals, Metals & Materials Society, Warrendale, 1996) p. 693.
11. W. Arbiter, WADC Technical Report 53-190, part I, 1953.
12. D. M. Shah, D. L. Anton, D. P. Pope, S. Chin, *Materials Science and Engineering A* 192/193 (1995) 658.
13. G. Sauthoff, in “Intermetallics” (VCH Publishers, New York,1995).

14. B. P. Bewlay, H. A. Lipsitt, M. R. Jackson, W. J. Reeder, J. A. Sutliff, *Materials Science and Engineering A* 192/193 (1995) 534.

15. B. P. Bewlay, J. A. Sutliff, M. R. Jackson, K. M. Chang, *Materials and Manufacturing Processes* 9 (1994) 89.

16. S. V. Raj, *Materials Science Engineering A* 192/193 (1995) 583.

17. S. V. Raj, J.D. Whittenberger, B. Zeumer, G. Sauthoff, *Intermetallics* 7 (1999) 743.

18. C. S. Chang, *Dissertation Abstracts International (USA)* 52 (1992) 206.

19. K. M. Chang, B. P. Bewlay, J. A. Sutliff, M. R. Jackson, *JOM-Journal of the Minerals Metals and Materials Society* 44 (1992) 59.

20. J. W. Newkirk, J. A. Sago, in Intermetallic Matrix Composites, D. L. Anton, R. McMeeking, D. B. Miracle and P. L. Martin, editors, (Materials Research Society, Pittsburgh, 1990) p.183.

21. J. W. Newkirk, J. E. Price, in High-Temperature Ordered Intermetallic Alloys VI, J. Horton, I. Baker, S. Hanada, R. D. Noebe and D. S. Schwartz, editors, (Materials Research Society, Pittsburgh, 1995) p. 955.

22. B. P. Bewlay, K. M. Chang, J. A. Sutliff, M. R. Jackson, in Intermetallic Matrix Composites II, D. B. Miracle, J. A. Graves and D. L. Anton, editors, (Materials Research Society, Pittsburgh, 1992) p. 417.

23. H. Bei, E. P. George, G. M. Pharr, *Intermetallics* 11 (2003) 283.

24. H. Bei, E. P. George, G. M. Pharr, in Defect Properties and Related Phenomena in Intermetallic Alloys, E. P. George, H. Inui, M. J. Mills and G. Eggeler, editors, (Materials Research Society Warrendale, 2003) p. 71.

25. R. M. Aikin, Jr., *JOM- Journal of the Minerals Metals and Materials Society* 49 (1997) 35.

26. S. G. Fishman, in In Situ Composites: Science and Technology, M. Singh and D. Lewis, editors, (The Minerals, Metals and Materials Society, Warrendale, 1994) p. 1.

27. S. Guruswamy, S. M. Park, J. P. Hirth, R. A. Rapp, *Oxidation of Metals* 26 (1998) 77.

28. C. H. Henager, J. L. Brimhall, J. P. Hirth, *Materials Science and Engineering A* 155 (1992) 109.

29. B. S. Murty, S. Ranganathan, *International Materials Reviews* 43 (1998) 101.

30. C. Suryanarayana, *International Materials Reviews* 40 (1995) 41.

31. C. C. Koch, *Materials Science and Engineering A* 244 (1998) 39.

32. D. Lewis III and M. Singh, in In Situ Composites: Science and Technology, M. Singh and D. Lewis, editors, (The Minerals, Metals and Materials Society, Warrendale, 1994) p. 21.

33. L. Christodoulou, P. A. Parrish and C. R. Crowe, in High Temperature/High Performance Composites, F. D. Lemkey, S. G. Fishman, A. G. Evans and J. R. Strife, editors, (Materials Research Society, Pittsburgh, 1988) p. 29.

34. N. P. Suh, *U.S. Patent* 4278622 (1981).

35. V. Shtessell, S. Sampath and M. Koczak, in In Situ Composites: Science and Technology, M. Singh and D. Lewis, editors, (The Minerals, Metals and Materials Society, Warrendale, 1994) p. 37.

36. A. Mortensen, S. Suresh, *International Materials Reviews* 40 (1995) 239.

37. S. Mazdiyasni and D.B. Miracle, in Intermetallic Matrix Composites, D.L. Anton, P. L. Martin, D. B. Miracle and R. McMeeking, editors, (Materials Research Society, Pittsburgh, PA 1990) p. 155.

38. W. T. King and B. F. Oliver, in Conference on In Situ Composites – III, Boston, December, 1978, J. L. Walter, M. F. Gigliotti, B. F. Oliver, H. Bibring, editors, (Ginn Custom Publishing, Lexington, 1978) p. 17.

39. J.M. Quenisset, J. Girol and R. Naslain, in Conference on In Situ Composites – III, Boston, December, 1978, J. L. Walter, M. F. Gigliotti, B. F. Oliver, H. Bibring, editors, (Ginn Custom Publishing, Lexington, 1978) p. 78.

40. M. K. Thomas, in Conference on In Situ Composites – III, Boston, December, 1978, J. L. Walter, M. F. Gigliotti, B. F. Oliver, H. Bibring, editors, (Ginn Custom Publishing, Lexington, 1978) p. 451.

41. D. L. Anton, D. M. Shah, D. N. Duhl and A. F. Giamei, *JOM-Journal of the Minerals Metals and Materials Society* 41 (1989) 12.

42. H. E. Boyer and T. L. Gall (editors), Metals Handbook – Desk Edition, (American Society for Metals, Metals Park 1985) p. 16.5.

43. S. M. Borowicz, L. Heatherly, R. H. Zee and E. P. George, in High-Temperature Ordered Intermetallic Alloys VIII, E. P. George, M. Yamaguchi and M. J. Mills, editors, (Materials Research Society, Warrendale, PA 1999), p. KK5.28.

44. Y. H. He, P. K. Liaw, Y. Lu, C. T. Liu, L. Heatherly, E. P. George, *Materials Science and Engineering A* 329 (2002) 696.

45. T. Reynolds and D. Johnson, in Defect Properties and Related Phenomena in Intermetallic Alloys, edited by E. P. George, H. Inui, M. J. Mills and G. Eggeler, (Materials Research Society Warrendale, 2003) p. 375.

46. T. B. Massalski (editor-in-chief), in "Binary Alloy Phase Diagrams", (American Society for Metals, Metals Park, Ohio, 1986).

47. J. D. Hunt, K. A. Jackson, *Transactions of the Metallurgical Society of AIME 236* (1966) 843.

48. K. A. Jackson and J. D. Hunt, *Transactions of the Metallurgical Society of AIME* 236 (1966) 1129.

49. M. Hillert, in Conference on In Situ Composites – III, Boston, December, 1978, J. L. Walter, M. F. Gigliotti, B. F. Oliver, H. Bibring, editors, (Ginn Custom Publishing, Lexington, 1978) p. 1.

50. M. C. Flemings, in "Solidification Processing", (McGraw-Hill, Inc., New York, 1974) p. 36.

51. R. Caram and S. Milenkovic, *Journal of Crystal Growth* 198/199 (1999) 844.

52. C. T. Rios, S. Milenkovic, S. Gama and R. Caram, *Journal of Crystal Growth* 237–239 (2002) 90.

53. J. M. Quenisset, R. Naslain, *Journal of Crystal Growth* 54 (1981) 465.

54. J. M. Quenisset, R. Sokolwski, M. E. Glicksman, *Journal of Crystal Growth* 63 (1983) 389.

55. V. Baskaran, W. R. Wilcox, *Journal of Crystal Growth* 679 (1984) 343.

56. S. Chandrasekhar, G. F. Eisa, W. R. Wilcox, *Journal of Crystal Growth* 76(1986) 485.

57. V. G. Levich, in "Physicochemical Hydrodynamics", (Prentice Hall, Englewood Cliffs 1962).

58. M. Mclean, in "Directionally Solidified Materials for High Temperature Service", (The Metals Society, London, 1983), p. 207.

59. D. M. Shah and D. L. Anton, *Materials Science and Engineering A* 153 (1992) 402.

60. R. L. Fleisher, in Intermetallic Matrix Composites, D.L. Anton, R. McMeeking, D. B. Miracle and P. L. Martin, editors, (Materials Research Society, Pittsburgh, 1990) p. 249.

61. R. L. Fleisher, R. S. Gilmore and R. J. Zabala, *Acta Metallurgica* 37 (1989) 2801.

62. R. L. Fleisher and R. J. Zabala, *Metallurgical Transaction A* 21 (1990) 2709.

63. G. V. Samsonov and I. M. Vinitskii, in "Handbook of refractory compounds", (IFI/Plenum Data company, New York, 1980).

64. F. Chu, D. J. Thoma, K. J. McClellan, P. Peralta, *Materials Science and Engineering A* 261(1999) 44.

65. R. L. Fleisher, *Scripta Metallurgica et Materialia* 27 (1992) 799.

66. S. Hong, C. L. Fu and M. H. Yoo, *Intermetallics* 7 (1999) 1169.

67. E. P. Barth, J. K. Tien, S. Uejo and S. Kambara, *Materials Science and Engineering A* 153 (1992) 398.

68. G. A. Henshall, M. J. Strum, B. P. Bewlay and J. A. Sutliff, *Metallurgical and Materials Transactions A* 28 (1997) 2555.

69. J. J. Lewandowski, in In Situ Composites: Science and Technology, M. Singh and D. Lewis, editors, (The Minerals, Metals and Materials Society, Warrendale, 1994) p. 159.

70. A. R. Rosenfield, G. T. Hahn and J. D. Embury, *Metallurgical Transactions* 3 (1972) 2797.

71. J. M. Hyzak and I. M. Bernstein, *Metallurgical Transactions A* 7 (1976) 1217.

72. D. C. Lemmon and O. D. Sherby, *Journal of Materials* 4 (1969) 444.

73. S. V. Meschel, O. J. Kleppa. *Journal of Alloys and Compounds* 267 (1998) 128.

Part Two: Experimental Procedures

In order to understand the relationships among processing, microstructures and mechanical properties of Cr-Cr_3Si alloys, various experimental techniques were employed in this study. These techniques can be roughly divided into three categories, including materials processing (e.g. alloy preparation, directional solidification, single crystal growth), microstructural examination (e.g. metallography, orientation imaging) and mechanical properties testing (e.g. nanoindentation, microhardness testing, fracture toughness testing).

2.1 Alloy preparation

Several Cr-Cr_3Si alloys were arc melted and drop cast in a cylindrical copper mold measuring 10 mm in diameter and 100 mm in length. The chromium and silicon starting materials (>99.995% pure) were carefully weighed and then mixed by arc melting, with the buttons flipped and re-melted five times to ensure good mixing before drop casting. Total weight losses after melting and casting were less than 0.2%, which led to negligible changes in alloy composition after melting. For example, for an alloy with nominal composition Cr - 16 at.% Si, even if all the weight loss is assumed to be the result of Cr evaporation (since Cr has the higher vapor pressure), the final alloy composition after drop casting changes to only Cr - 16.02 at.% Si. Therefore, all compositions discussed in this paper are nominal compositions (atomic %) unless otherwise stated.

2.2 Directional solidification of Cr-Cr_3Si eutectic

The drop cast ingots were directionally solidified using an optical floating zone furnace (shown in Fig. 2-1). Infrared radiation emitted from a xenon arc lamp was focused on specimens enclosed in a quartz tube which was first evacuated and back filled with flowing argon gas. Drop-cast polycrystalline rods were used as the feed material, and pieces cut from several different directionally solidified rods were used for the seed. The seed rod and the feed rod were rotated in opposite directions during the zone melting to form a homogeneous molten zone. A stable molten zone, about 15 mm long, was maintained during directional solidification by monitoring its length with a video camera and adjusting the power of the lamp as needed. The temperature gradient in the hot zone was about 250-330°C cm^{-1} [1].

While there was negligible weight loss ($\leq$ 0.2%) during arc melting and drop casting, there was somewhat more weight loss (~0.7%) during the subsequent directional solidification step. As a result, the composition after directional solidification was slightly Cr-depleted (~0.1 at%), when compared to the nominal composition, assuming that all the weight loss is caused by Cr evaporation. Excess Cr was added to compensate for this evaporation during directional solidification. Therefore, the starting compositions that we used for directional solidification were always slightly Cr-rich compared to those used for drop casting. To get a fully lamellar eutectic structure devoid of any pro-eutectic phases, the nominal composition used for drop casting was Cr - 16.05% Si, whereas that used for directional solidification was Cr - 15.95 at.% Si.

The effects of growth conditions on lamellar microstructures were systematically

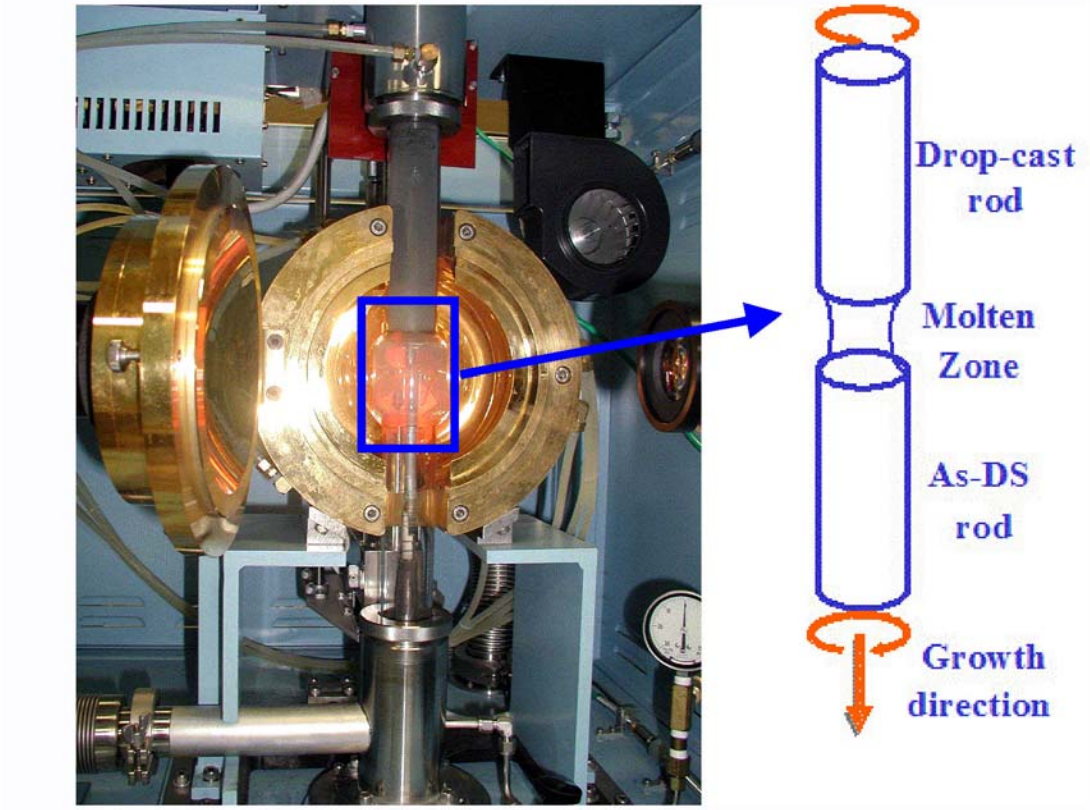

Figure 2-1. High temperature xenon arc lamp optical floating zone furnace.

investigated in an alloy having the eutectic composition. Growth rates were varied from 10 to 150 mm/h and specimen rotation rates from 10 to 60 rpm. In addition, off-eutectic alloys were used to investigate effects of volume fractions on the microstructural morphologies.

2.3 Cr_3Si single crystal preparation

An alloy with starting composition 76 at% Cr – 24 at% Si was arc melted and drop cast. Although the drop-cast Cr_3Si rods were brittle and normally broke into several pieces, occasionally some rods as long as 70 mm were obtained. The longer drop cast ingots were used as feed rods for single crystal growth in the optical floating zone melting furnace with a previously grown crystal used as the seed. Necking during the initial stages of directional solidification was utilized to promote single crystal growth as discussed in Chang's work [2]. The crystal growth rate was 20 mm/h, and the rotation rate was 60 rpm in this study.

Laue back scattered X-ray diffraction revealed that the growth direction was near [120]. This single crystal Cr_3Si was reoriented and cut normal to the [100] and [110] directions and used as seeds to produce two additional single crystals with growth directions oriented along [100] and [110], respectively.

2.4 Metallography

The directionally solidified rods were cut transversely and longitudinally using electro-discharge machining, and representative samples were mounted in epoxy. After grinding the samples flat through 600 grit SiC paper, they were polished with diamond paste (particle size 0.5 μm) using an automatic vibratory polishing machine. To reveal the microstructure of the eutectics, the samples were etched with Murakami's solution (1 part 10% *KOH* and 1 part 10% $K_3Fe(CN)_6$). The etched specimens were examined by both optical and scanning electron microscopy (SEM).

2.5 Orientation relationships between the lamellae

Electron back-scatter diffraction (EBSD) patterns were acquired in a FEI XL30FE6 scanning electron microscope using an accelerating voltage of 20 kV and a 20 mm working distance. Patterns from individual Cr_3Si and Cr solid-solution lamellae were recorded and indexed. The Kikuchi-line patterns were automatically indexed by the *OIM ANALYSIS* package (release version 3.08, *TSL*™ http://www.tsl-oim.com/). To determine the crystallographic orientation relationships of the lamellae, it was most convenient to present the results as pole figures showing the {100}, {110} and {111} poles.

2.6 Nanoindentation

Nanoindentation experiments were conducted at 23˚C using a Nanoindenter® II (Nano Instruments Innovation Center, MTS corporation, Knoxville, TN). Displacements

and loads were measured with a resolution of 0.16 nm and 0.3 μN, respectively. A Berkovich diamond indenter (3-sided pyramidal tip) was used. The area function of the tip and the compliance of the nanoindentation system were calibrated by testing fused quartz standard specimens using the method of Oliver and Pharr [3]. The continuous stiffness measurement mode was used for all the experiments. The experiments were run in load control at constant $\dot{P}/P$ rate to a prescribed maximum load that ranged from 3 mN to 20 mN.

2.7 Ultrasonic measurement of elastic constants of Cr_3Si single crystal

Two cylindrical single crystals with axes along [100] and [110], were used to determinee elastic constants by measuring the propagation velocities of longitudinal and transverse ultrasonic waves. The details of this technique are discussed elsewhere [4].

For an isotropic material, two independent elastic constants can be obtained from two ultrasonic measurements made on one specimen, namely the longitudinal velocity V_1 and transverse (shear) velocity V_2. From these measurements, Possion's ratio can be computed as:

$$\upsilon = \frac{V_1^2 - 2V_2^2}{2(V_1^2 - V_2^2)}, \qquad (2\text{-}1)$$

and Young's modulus is

$$E = \rho \cdot V_1^2 \cdot \frac{(1+\upsilon)(1-2\upsilon)}{1-\upsilon} \qquad (2\text{-}2)$$

where ρ is the density of the specimen.

For a cubic system, the three independent elastic constants can be calculated by making measurements on two different samples with axis directions [100] and [110]. For the [100] direction,

$$V_1 = \left(\frac{C_{11}}{\rho}\right)^{1/2} \qquad \text{(longitudinal)} \qquad (2\text{-}3)$$

$$V_2 = \left(\frac{C_{44}}{\rho}\right)^{1/2} \qquad \text{(transverse)} \qquad (2\text{-}4)$$

and for the [110] direction

$$V_1 = \left(\frac{C_{11} + C_{12} + 2C_{44}}{2\rho}\right)^{1/2} \qquad \text{(longitudinal)} \qquad (2\text{-}5)$$

where ρ is the density of the specimens and V_1 and V_2 are the longitudinal and transverse wave velocities.

The densities of the specimens were measured with an AccuPyc^{TM} 1330 pycnometer. Weights and volumes were measured with a precision of 0.0001 g and 0.03%, respectively, and density with an accuracy better than 0.01 g/cm^3.

2.8 Fracture toughness testing

Fracture toughness was measured using a 3-point bend method. Figure 2-2 shows the geometry of the bend specimen containing a chevron notch machined with an electro-discharge machine. A 20 mm span and 45º notch angle were used in all tests. The bend tests were performed in an Instron 4501 screw driven mechanical testing machine at a

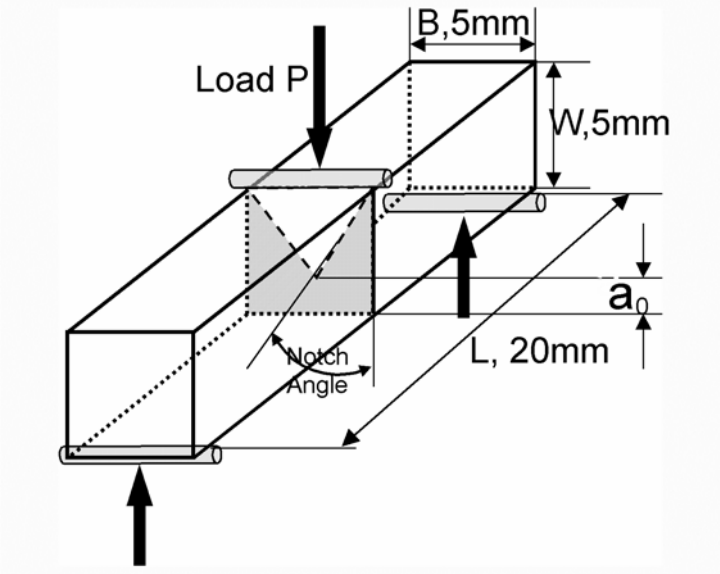

Figure 2-2. Geometry of three-point bend specimen with chevron notch [5].

crosshead speed of 10 μm/s. The fracture surfaces were examined and photographed in a scanning electron microscope (SEM).

References:

1. T. Hirano, National Institute for Materials Science, Japan, private communication.
2. C. S. Chang, *Dissertation Abstracts International (USA)* 52 (1992) 206.
3. W. C. Oliver, and G. M. Pharr, *Journal of Materials Research* 7 (1992) 1564.
4. W. P. Mason, in "American Institute of Physics Handbook", D. N. Fischel, et al., editors, (McGraw-Hill Book Company, New York, 1972) p.3-98.
5. D. Munz, R. T. Bubsey, and J. L. Shannon, Jr., *Journal of American Ceramic Society* 63(1980) 300.

Part Three: Effects of Composition on Lamellar Microstructures of Near-Eutectic Cr-Cr_3Si Alloys

This part is a slightly revised version of a paper by the same name published in the journal *Intermetallics* in 2003 by Hongbin Bei, Easo P. George, and George M. Pharr: H. Bei, E. P. George, and G. M. Pharr. Effects of composition on lamellar microstructures of near-eutectic Cr-Cr_3Si alloys, *Intermetallics* 4 (2003) 283-385.

Among the factors that affect the growth of lamellar structures during directional solidification, composition is extremely important because the growth of fine, well-aligned two-phase structures is easiest at or near the eutectic composition.[1,2] In this chapter, the effect of composition on the lamellar structure is examined by investigating the microstructures of drop-cast and directionally solidified Cr-Cr_3Si alloys for a number of near-eutectic compositions.

3.1 Drop cast alloys

Several Cr-Cr_3Si alloys with compositions given in Table 3-1 were arc melted and drop cast in a cylindrical copper mold measuring 10 mm in diameter and 100 mm in length. Optical micrographs of the drop cast rods (Fig. 3-1) showed that a regular lamellar eutectic structure was present in all the samples. In the off-eutectic compositions, an excess of either the pro-eutectic Cr-rich phase or Cr_3Si phase was present. The pro-eutectic phases were identified both by their relative hardnesses (the Vickers hardness of the pro-eutectic Cr-rich phase is about HV530 and that of Cr_3Si is about HV1200) and by the presence or absence of cracks during microhardness testing (Fig. 3-2 a and b). Figure 3-2c shows that the cracking behavior of the single-phase Cr_3Si alloy (Cr - 24% Si) is

Table 3-1. Nominal compositions and phases present in drop-cast Cr-Cr_3Si alloys investigated in this study.

Alloy designation	at% Cr	at% Si	Microstructure	Micrograph
CS-3	87	13	(Cr)+E	Figure 3-1 (a)
CS-4	86	14	(Cr)+E	Figure 3-1 (b)
CS-1	85	15	(Cr)+E	Figure 3-1 (c)
CS-7	84.5	15.5	(Cr)+E	Figure 3-1 (d)
CS-5	84	16	(Cr)+E	Figure 3-1 (e)
CS-10	83.95	16.05	E	Figure 3-1 (f)
CS-9	83.9	16.1	E+(Cr_3Si)	Figure 3-1 (g)
CS-8	83.5	16.5	E+(Cr_3Si)	Figure 3-1 (h)
CS-6	83	17	E+(Cr_3Si)	Figure 3-1 (i)
CS-2	76	24	Cr_3Si	Figure 3-2 (c)

Note: (Cr) is chromium rich solid-solution phase, and E refers to eutectic.

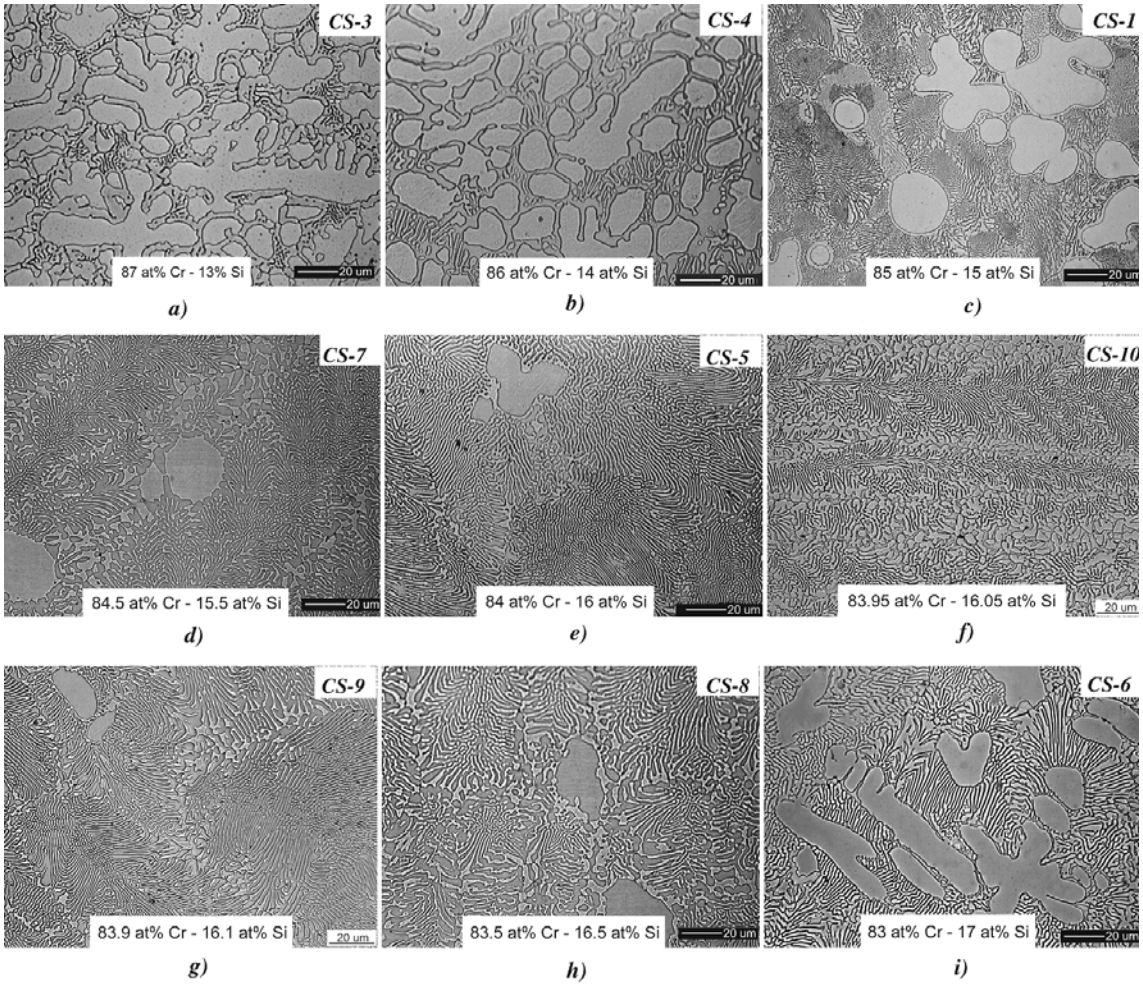

Figure 3-1. Optical micrographs showing the microstructures of drop-cast Cr-Si alloys.

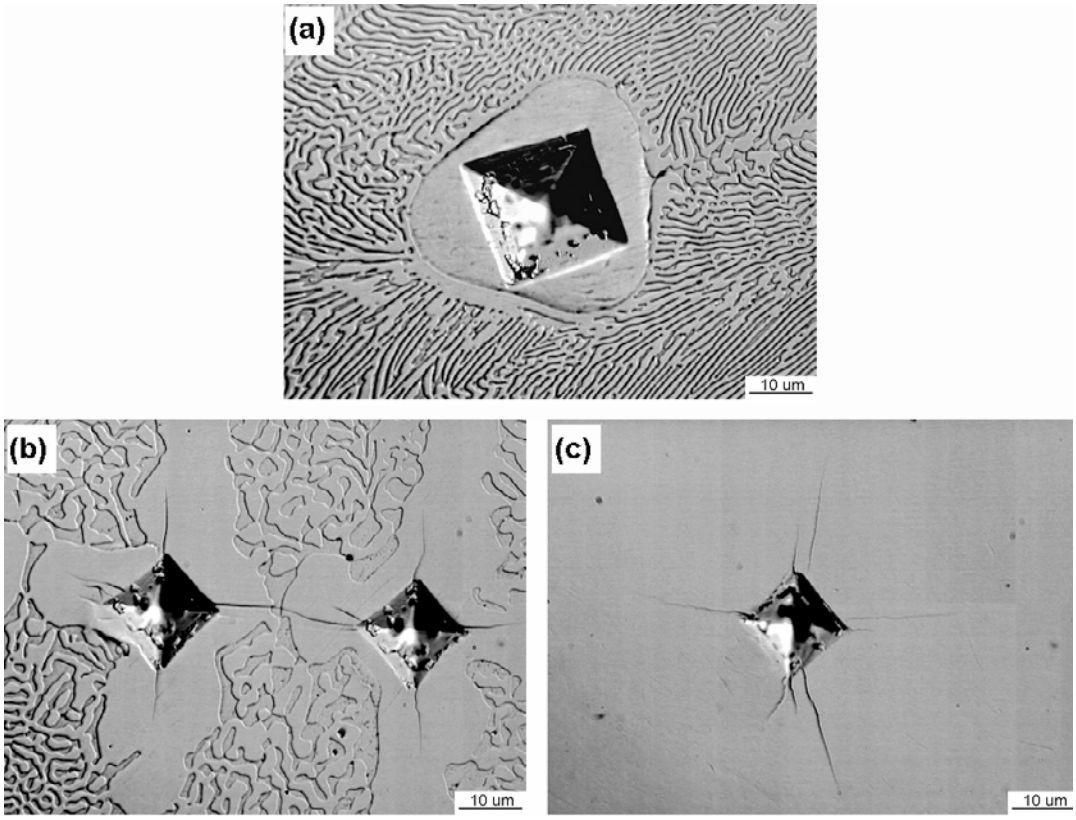

Figure 3-2. Microhardness impressions showing that (a) the pro-eutectic phase in the 84% Cr-16% Si alloy is the softer and more ductile Cr-rich phase with a microhardness of HV523; (b) the pro-eutectic phase in the 83.9% Cr-16.1% Si alloy is the brittle Cr_3Si phase with a microhardness of HV1200; and (c) the brittle Cr_3Si single phase structure of the 76% Cr-24% Si alloy has a hardness comparable to that of the pro-eutectic Cr_3Si phase in (b) (all samples tested at 300 g load).

similar to that of the pro-eutectic Cr_3Si phase (Figure 3-2b). The phases present in the various alloys are summarized in Table 3-1.

As can be seen in Fig. 3-1, the alloys containing 16.0, 16.05, and 16.1% Si are almost fully lamellar (Figure 3-1e, f and g). For the purpose of accurately determining whether any pro-eutectic phases were present in these alloys, their entire cross sections were thoroughly examined at low magnification (Fig. 3-3). It was found that the 16.05% Si alloy was the only one that exhibited an almost fully lamellar microstructure (Fig. 3-3b). Deviations from this composition on either side, even by small amounts (Fig. 3-3 a & c) result in the formation of pro-eutectic phases. Microhardness tests showed that the pro-eutectic phase in the 16.0% Si alloy is the Cr-rich solid solution and that in the 16.1% Si alloy is the Cr_3Si intermetallic (Fig. 3-3 a, c). In contrast, the 16.05% Si alloy (Fig. 3-3 b) is almost entirely devoid of any pro-eutectic phases. These microstructural observations suggest that the best composition for obtaining fully lamellar eutectic structures is closer to 16.05% Si rather than the 15% Si eutectic composition indicated in the phase diagram [3].

3.2 Directionally solidified alloys

The 16.05% Si alloy was chosen for growth of lamellar structures by directional solidification. The directionally solidified microstructures are shown in Fig. 3-4. A well-aligned lamellar structure was formed (Fig. 3-4a) in the center of the rod. However, a Cr_3Si pro-eutectic phase was observed in the sample, but only near the outer edge of the rod (Fig. 3-4b). This result appears to be in conflict with the result discussed above for

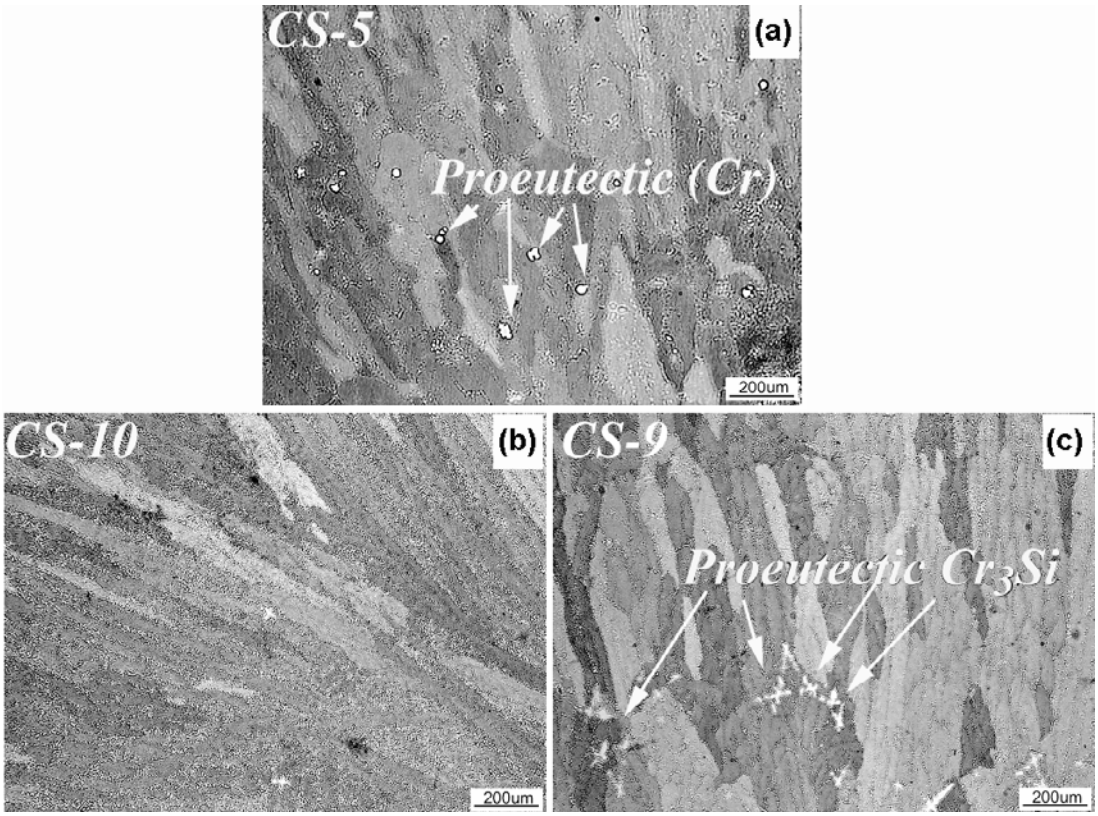

Figure 3-3. Low magnification optical micrographs showing the microstructures of drop cast Cr-Cr_3Si alloys: (a) 84% Cr-16% Si; (b) the fully eutectic structure at 83.95% Cr-16.05% Si; and (c) 83.9% Cr-16.1% Si.

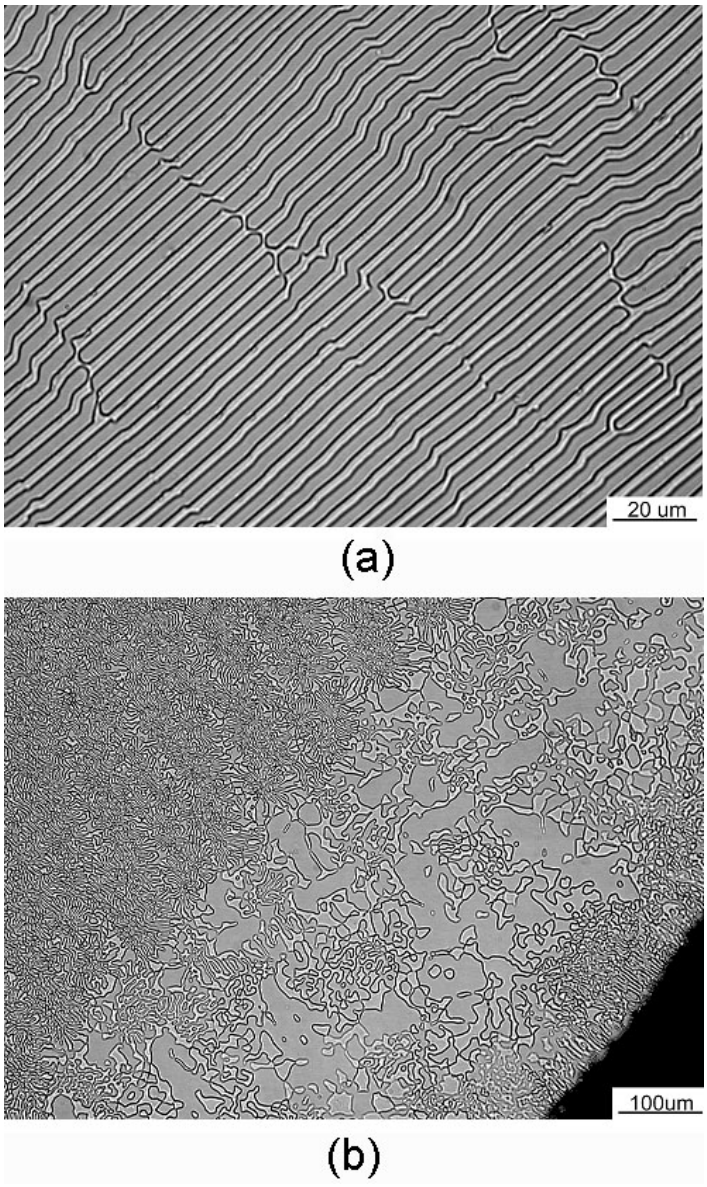

Figure 3-4. Microstructures of a directionally solidified alloy with composition 83.95% Cr-16.05% Si grown at 40 mm/h and 60 rpm: (a) Well-aligned lamellar structure in the center of the rod; (b) Cr_3Si pro-eutectic phase embedded in a poorly-aligned lamellar structure near the edge of the rod.

the drop-cast alloy. One possible explanation is that there was weight loss during the directional solidification, amounting to about 0.7% of the total weight of the feed and seed rods. Because the vapor pressure of chromium is relatively high, about ten times the vapor pressure of silicon at the processing temperatures, [4] it is reasonable to assume that the weight loss is caused by the evaporation of chromium during directional solidification. As a result, the molten zone that started out as the best composition for obtaining the fully lamellar structure becomes slightly enriched in silicon.

When an off eutectic alloy solidifies from the melt, the pro-eutectic phase precipitates first with the composition of the remaining liquid gradually approaching the eutectic composition. During the directional solidification discussed here, the edge of the rod solidified first because the cooling at the edge was faster than in the center. As a result, in both hypoeutectic and hypereutectic alloys the pro-eutectic phases are found near the edge. However, after the pro-eutectic phases have precipitated, the composition of the remaining liquid is very close to the eutectic composition leading to a well-aligned lamellar eutectic structure in the center of the rod.

To compensate for the 0.7% weight loss caused by the Cr evaporation, a new alloy with a slightly higher chromium concentration, 84.05% Cr –15.95% Si, was drop cast and directionally solidified. Its microstructures are shown in Fig. 3-5. The lamellar eutectic structure is observed not only in the center but also near the edge of the rod, although the lamellar structure near the edge is not well aligned, possibly because the heat flux at the edge is not strictly parallel to the solidification direction. These results indicate that the growth of fully lamellar Cr-Cr_3Si is best achieved by starting with a

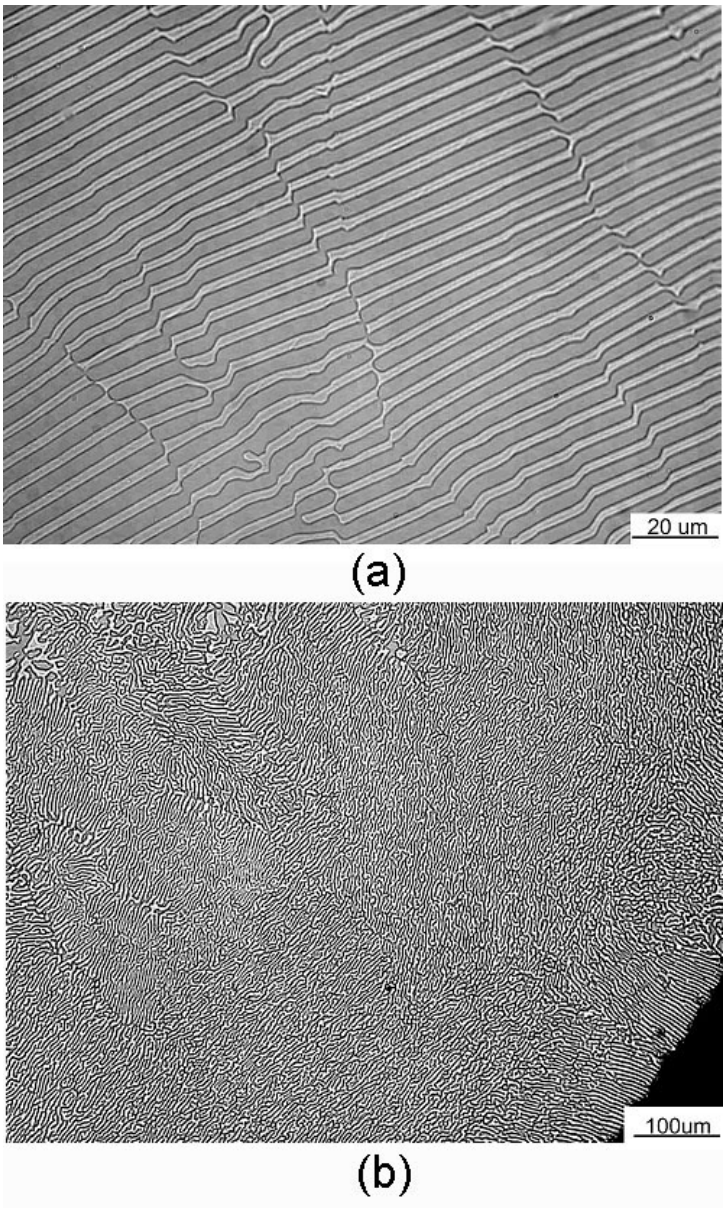

Figure 3-5. Micrographs showing fully lamellar microstructures throughout the cross-section of a directionally solidified alloy with starting composition 84.05% Cr-15.95% Si grown at 40 mm/h and 60 rpm: (a) Well-aligned lamellar structure in the center of the rod; (b) Poorly-aligned lamellar structure near the edge of the rod. No pro-eutectic phase was found anywhere in the rod.

composition of 84.05% Cr - 15.95% Si, which becomes 83.95% Cr - 16.05% Si due to Cr evaporation during directional solidification.

The normally accepted value of the Cr-Cr_3Si eutectic composition based on Chang's work [5] is 85% Cr - 15% Si. However, the results of the current work show thatan alloy with the nominal composition of 85% Cr- 15% Si has large amounts of a distinct Cr-rich pro-eutectic phase in the drop cast microstructure (Fig. 3-1c). As shown in Figure 3-6, although directional solidification produces a well-aligned lamellar structure at this composition, a Cr-rich pro-eutectic phase is observed not only near the edge, but also in the center of sample. Upon examination of a longitudinal section of the sample (Fig. 3-6c), it was found that the morphology of the Cr-rich pro-eutectic is dendritic with growth in the solidification direction. The presence of the Cr-rich pro-eutectic phases in both the drop-cast and directionally solidified alloys of composition 85% Cr-15% Si suggests that the normally accepted value of the Cr-Cr_3Si eutectic composition is not the best for obtaining a fully lamellar eutectic structure.

There are several reasons why the fully lamellar structure does not occur at the eutectic point indicated in the phase diagram. First, it is possible that the structure is not in equilibrium whereas the phase diagram indicates the equilibrium structures. Second, it is possible that the eutectic composition shown in the phase diagram is incorrect and the true eutectic composition is that which is identified in this study, namely, 83.95% Cr-16.05% Si. To verify the latter possibility, additional tests are needed, such as differential scanning calorimetry (DSC), but the very high melting point of the alloy (T_m=1705°C) makes such measurements difficult.

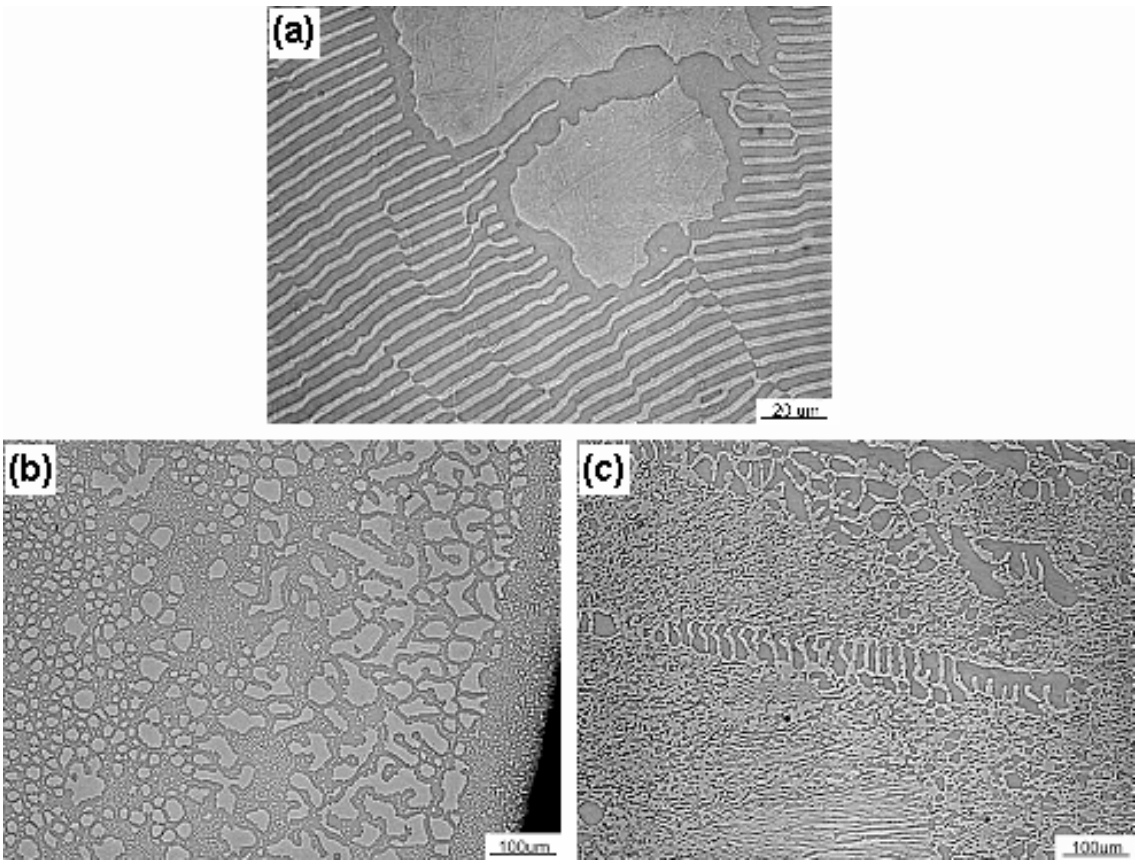

Figure 3-6. Microstructures of an alloy with composition 85% Cr-15% Si grown at 40 mm/h 60 rpm: (a) Cr-rich phase embedded in a well-aligned lamellar structure in the center of the rod; (b) Large amounts of Cr-rich phase embedded in not well-aligned lamellar structure near the edge of the rod; (c) Longitudinal section showing the dendritic nature of the pro-eutectic phase.

3.3 Conclusion

Fully lamellar microstructures devoid of pro-eutectic phases are produced in drop-cast specimens of Cr-Cr_3Si at a composition of 83.95% Cr – 16.05% Si. Deviations from this composition on either side result in the formation of pro-eutectic phases.

In directionally solidified alloys, fully lamellar microstructures through the entire cross section of the specimen are produced at the nominal composition 84.05%Cr – 15.95%Si. Compared to the eutectic composition, this slightly higher chromium concentration is needed because there is preferred evaporation of chromium during directional solidification due to its high vapor pressure. The lamellar structures are well aligned in the center of the specimen, but lose their alignment near the edges, probably because the heat flux at the edge is not parallel to the solidification direction.

Collectively, these results show that the best composition for obtaining fully lamellar structure is close to 16.05% Si rather than the 15% Si, eutectic composition indicated in the phase diagram.

References:

1. J. D. Livingston, *Composites* 4 (1973) 70.
2. F. R. Mollard and M. C. Flemings, *Transactions of the Metallurgical Society of AIME* 239 (1967) 1526.
3. T. B. Massalski (editor-in-chief), in "Binary Alloy Phase Diagrams", (American Society for Metals, Metals Park (Ohio), 1986).
4. R. E. Honing, *RCA Review*, XXIII (1962) 567.
5. Y. A. Chang, *Transactions of the Metallurgical Society of AIME* 242 (1968) 1509.

Part Four: Directional Solidification and Microstructures of Near-Eutectic Cr-Cr_3Si Alloys

This part is a slightly revised version of a paper by the same name published in the journal *Acta Materialia* in 2003 by Hongbin Bei, Easo. P. George, Edward A. Kenik, and George M. Pharr:

H. Bei, E. P. George, E. A. Kenik, and G. M. Pharr. Directional solidification and microstructures of near-eutectic Cr-Cr_3Si alloys, *Acta Materialia* 51 (2003) 6241-6252.

The microstructures, orientation relationships between the lamellae, and the effects of the solidification parameters, such as growth rate and specimen rotation rate, on the lamellar microstructures of alloys containing 15.95 at.% Si are investigated in this part. In addition, alloys in which the Si concentration deviated from 15.95 at.% were also directionally solidified to change the volume fractions of the two phases and their morphologies. These alloys varied from 13 to 16.05 at.% Si. These compositions span the best range for obtaining a fully lamellar structure (15.95 at.% Si).

4.1 Microstructures of directionally solidified Cr-Cr_3Si eutectic alloys

The typical microstructure of directionally solidified Cr-Cr_3Si eutectics is lamellar (Fig. 4-1). For a wide range of solidification conditions (growth rates from 20 to 100 mm/h and rotation rates from 10 to 60 rpm), a well-aligned lamellar structure was observed in the center of the rods. A misaligned or broken lamellar structure was found in a narrow rim (about 1mm thick) near the outer surface of the rods. This surface effect may be the result of the local temperature gradient at the solidification front, which tends to fluctuate with the flowing argon gas, not being parallel to the growth direction. Typical microstructures in the transverse and longitudinal sections, as shown in Fig. 4-1, indicate

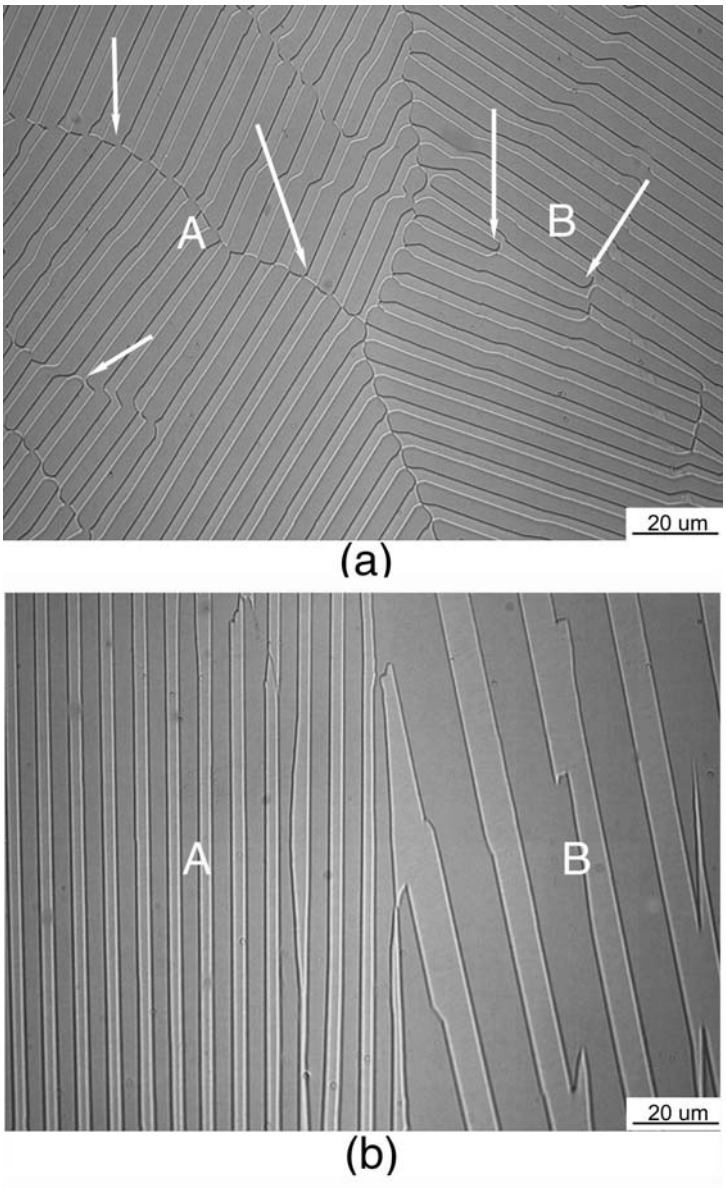

Figure 4-1. Optical micrographs showing fully lamellar microstructure of Cr-Cr_3Si eutectic alloy directionally solidified at 40 mm/h and 60 rpm: (a) transverse section and (b) longitudinal section [relative to the solidification direction, which is normal to the plane of the figure in (a) and vertical in (b)]. The thick and thin phases are Cr-rich solid solution and Cr_3Si phases, respectively.

that the lamellar spacing is almost everywhere the same on the transverse section, but large differences are apparent on the longitudinal section.

When a pure eutectic alloy is constrained to grow unidirectionally, the lamellae in all the eutectic colonies grow in an edgewise manner in a direction approximately parallel to the heat flow direction, and the solid-liquid interface remains planar throughout the solidification process. However, the rotation of the lamellae around the growth axis is not restricted. Therefore, many colonies, in which the lamellar orientation changes from colony to colony, are clearly distinguishable on the transverse sections. Since the lamellae are nearly perpendicular to the transverse section, the interlamellar spacings measured on the transverse sections are fairly constant across the various colonies, but sections parallel to the growth direction show different interlamellar spacings for different colonies due to the rotation of the lamellae about the growth direction relative to the section. For this reason, all lamellar spacings discussed in this study were measured on transverse sections. Figure 4-2 shows the lamellar microstructure in one colony. As shown this figure, the structure in any one colony is well-aligned.

Micrographs of the directionally solidified lamellar eutectic show that the structure does not consist of perfectly parallel sheets of alternating eutectic phases extending uninterrupted through the entire length of the crystal. As can be seen in Fig. 4-1a (at locations marked by arrows), discontinuous lamellae, which are referred to in the literature [1] as “terminations,” are evident on the transverse section. At most of these terminations, mismatch surfaces, or “faults,” separate two relatively perfect lamellar regions. Such lamellar faults are common features of lamellar eutectics [2], with the

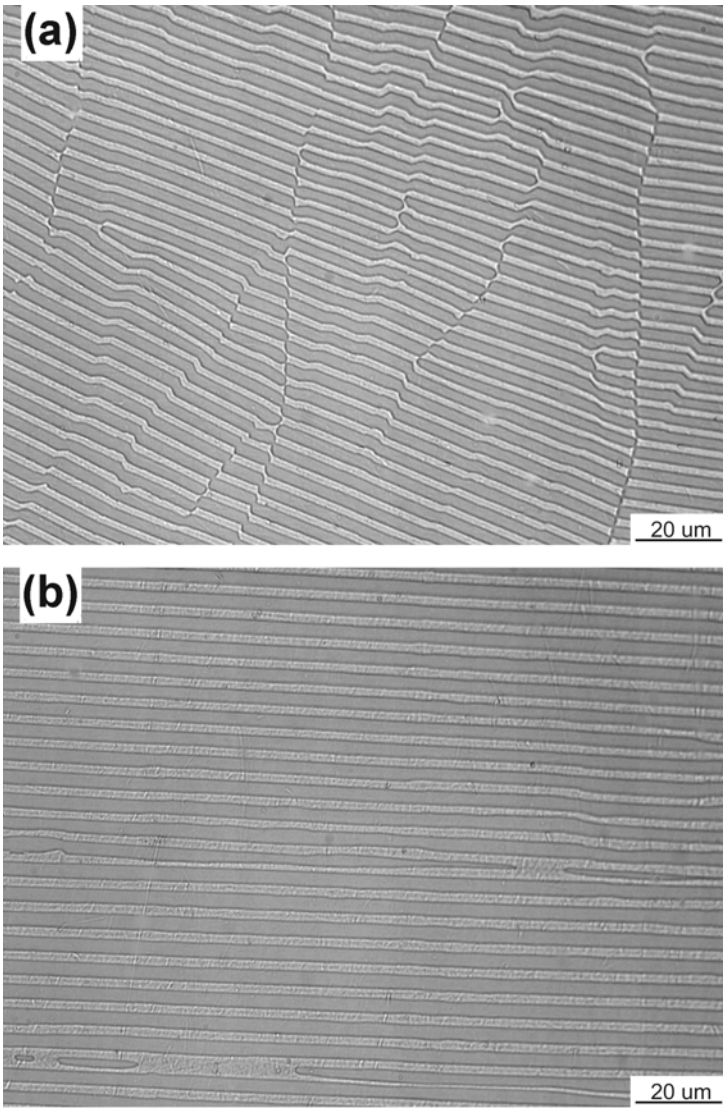

Figure 4-2. Optical micrographs showing well aligned lamellar microstructure of directionally solidified Cr-Cr_3Si eutectic alloy: (a) transverse, and (b) longitudinal section (growth at 60 mm/h and 60 rpm). The thick and thin phases are Cr_3Si and Cr-rich solid solution, respectively.

terminations believed to provide conditions for the production of a constant interlamellar spacing at a particular growth rate [3, 4].

The volume fraction of Cr_3Si was calculated from the measured area fractions on transverse sections and found to be about 0.62. This value is in agreement with that reported by Sutliff et al. [5], but in conflict with the volume fraction (~ 0.42) predicted by the equilibrium phase diagram (Fig.1-2). In part three it was shown that the eutectic composition of Cr-Cr_3Si is closer to Cr - 16.05% Si, rather than the Cr-15% Si indicated on the phase diagram. However, this alone cannot account for the difference between the measured volume fraction and that predicted by the phase diagram, suggesting that the Si concentrations of the Cr solid-solution and the Cr_3Si at the solidification temperature may be different from those indicated in the equilibrium phase diagram. To verify this possibility x-ray microprobe analysis was conducted to determine the compositions of these two phases. It was found that the Si contents of the Cr solid-solution and Cr_3Si are 7.9±0.2% and 21.1±0.2%, respectively, rather than 9.5% and 22.5% as indicated on the phase diagram (Fig. 1-2). Therefore, the eutectic reaction, for the solidification condition discussed in this study, may best be written as:

$$L(16.05\pm 0.1\%) \rightarrow (Cr)(7.9\pm 0.2\%) + Cr_3Si(21.1\pm 0.2\%),$$

where the quantities in brackets are the Si contents of the respective phases. Using the above compositions, and the densities of the two eutectic phases ($\rho_{(Cr)} = 6.91 g/cm^3$ and $\rho_{Cr_3Si} = 6.47 g/cm^3$) [5], the calculated volume fraction of the Cr_3Si phase is about 0.62, which is identical to the measured value of 0.62.

At very low growth rates, such as 10 mm/h, the lamellar microstructure is replaced with the degenerate structure shown in Fig. 4-3a. At the other extreme, a cellular structure, consisting of fine lamellae inside the colonies and coarse regions at the colony boundaries, is produced at relative high growth rates, for example, 150 mm/h (Fig. 4-3b).

The reason for the formation of the degenerate structure at low growth rates is not well understood. A speculative argument has been presented by Kraft and Albright [6]. If the interface energy of the lamellar eutectic is not the minimum, then the structure can decrease its total energy by changing to another configuration where the interphase boundary area may be larger but the product of the interphase boundary energy and the boundary area is smaller. As for the cellular structure, it is possibly caused by very small amounts of an impurity element, or because the solidified alloy deviates slightly from the exact eutectic composition, as discussed in a later section.

4.2 Crystallographic orientation relationships

The crystallographic orientation of the two phases of the eutectic, relative to the growth direction and the interface boundary between the phases, was determined by orientation imaging microscopy. Several specimens with lamellar spacings from about 2.5 to 5.0 μm were examined. Electron backscattered diffraction patterns were recorded from individual lamellae in different colonies in each sample and also from different positions within the same colonies. Figure 4-4 shows the EBSD patterns from individual Cr_3Si and Cr solid-solution lamellae in a sample solidified at 20 mm/h and 60 rpm. To describe the crystallographic orientation relationships of the lamellae relative to the

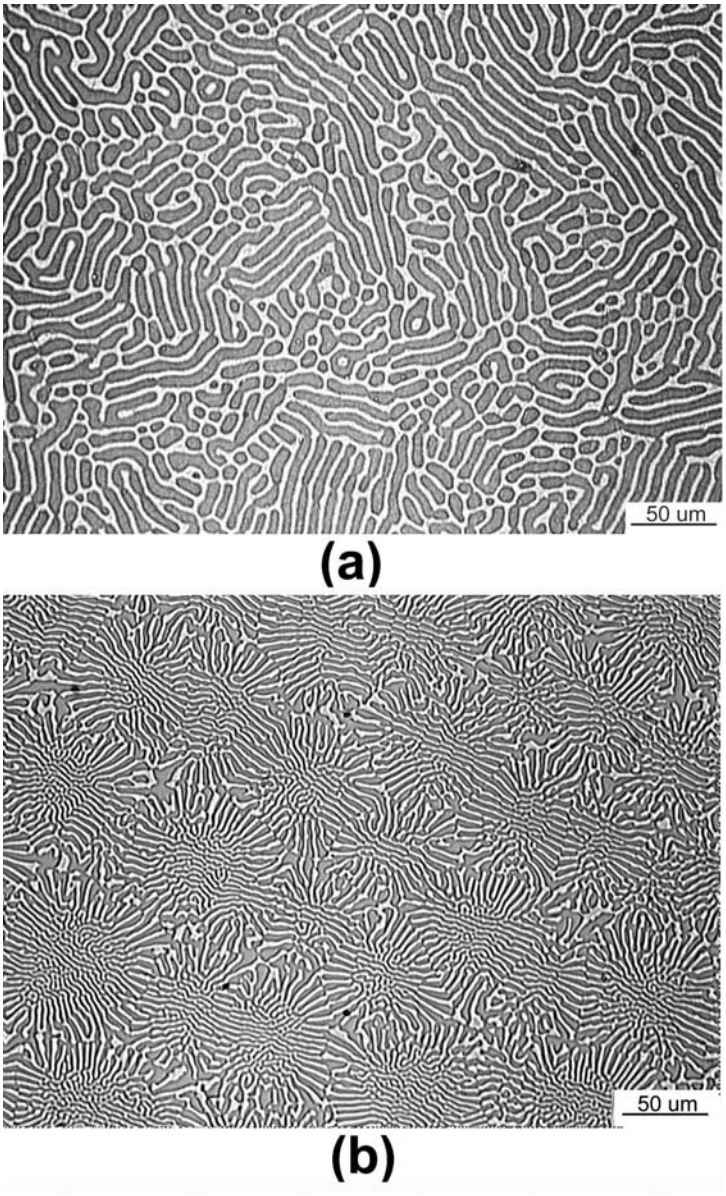

Figure 4-3. Optical micrographs showing that the well aligned lamellar structure of the Cr-Cr_3Si alloy is replaced by (a) degenerate structure at 10 mm/h growth rate, and (b) cellular structure at 150 mm/h growth rate.

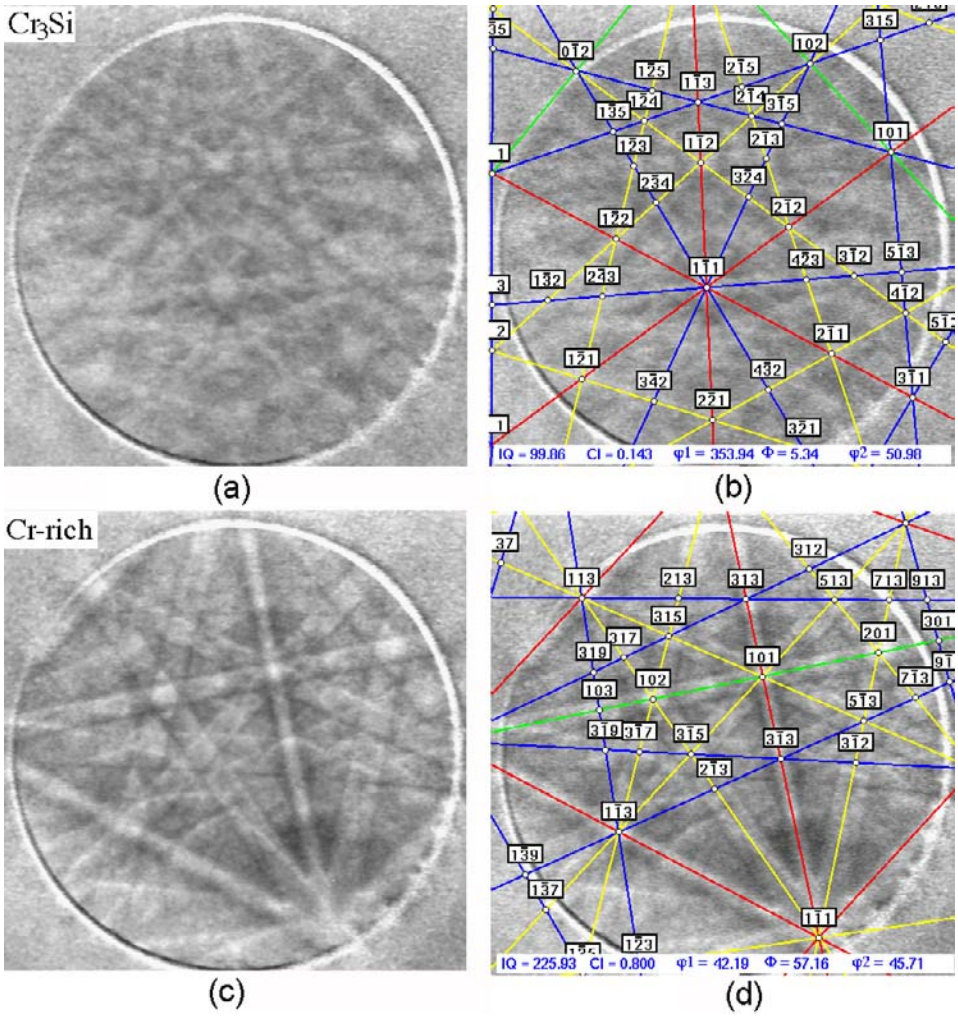

Figure 4-4. Electron backscatter diffraction (EBSD) patterns obtained from (a) Cr_3Si and (c) Cr-rich phases, respectively, on a transverse section of the directionally solidified Cr-Cr_3Si eutectic alloy; (b) and (d) are indexed EBSD patterns of (a) and (c). These images were obtained with the normal direction (ND) at 70° to the electron beam direction.

growth direction, the results are conveniently presented as pole figures showing the {100}, {110} and {111} poles because both phases have cubic crystal structures. Figures 4-5 a and b show the {100}, {110} and {111} pole figures of the Cr_3Si and Cr solid-solution phases, respectively. The normal direction (ND) is perpendicular to the plane of the paper which in turn is parallel to the growth direction of the lamellae; the rolling direction (RD) is perpendicular to the lamellar interface, and the transverse direction (TD) is parallel to the lamellar interface in the transverse cross section. As can be seen in Fig. 5, the orientation relationships between the two eutectic phases are: $(011)_{Cr_3Si} // (12\bar{3})_{Cr}$ and $[100]_{Cr_3Si} // [111]_{Cr}$.

In the present investigation the growth direction of the Cr_3Si phase is always <100> and that of the Cr solid-solution phase is always <111>. These are close-packed directions in the two phases: <100> in the Cr_3Si phase (*A*15 crystal structure), and <111> in the Cr-rich phase (BCC crystal structure). In contrast, two different relative orientations of the lamellar phases, both involving low-index planes, were observed: $(001)_{Cr_3Si} // (0\bar{1}\bar{1})_{Cr}$ and $(011)_{Cr_3Si} // (12\bar{3})_{Cr}$. However, in both these cases, the lamellar boundaries were macroscopically parallel to these planes. The orientation relationships observed in this study are not the same as those reported by Bewlay et al. [7], indicating that the relative orientations of the eutectic phases in the Cr-Cr_3Si system may depend on the specific growth conditions. A similar variability was also observed in the Al-$CuAl_2$ eutectic system [8].

In the present study, the number of colonies generally decreased as the directional solidification progressed, i.e., there were more colonies at the start of the process which

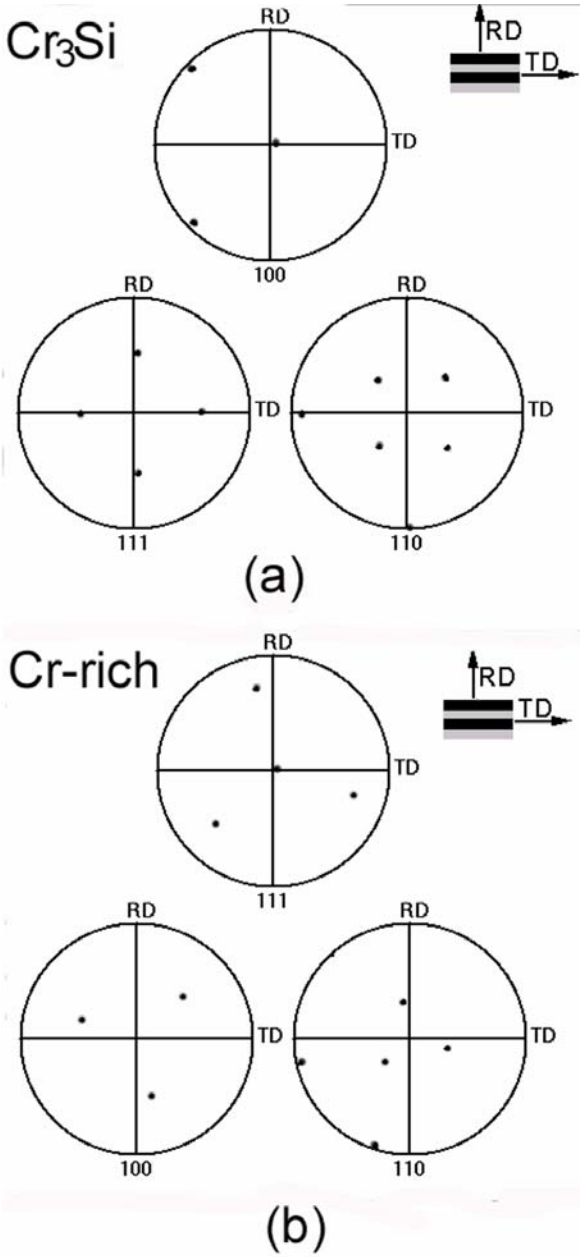

Figure 4-5. The {100}, {110} and {111} pole figures obtained from (a) Cr_3Si and (b) Cr-rich phases, respectively, on a transverse section of the directionally solidified Cr-Cr_3Si eutectic alloy showing the orientation relationships of the two phases. The growth direction (ND) is perpendicular to the plane of the paper.

merged into fewer colonies during the later stages of growth. Therefore, although the seeds came from several different directionally solidified rods, it is possible that they all had the same orientation. From the present results it is not possible to say whether the orientation relationships discussed above are dependent on the orientation of the seed used.

4.3 Effects of growth rate on lamellar structure

The interlamellar spacing, λ, defined as the distance from the center of the Cr solid-solution lamellae to the center of the Cr_3Si lamellae, was measured over a range of growth rates, R, from 20 to 100 mm/h at two different rotation rates of 10 and 60 rpm. Figure 4-6 shows the lamellar structure obtained at growth rates of R = 20 mm/h and 60 mm/h (rotation speed 60 rpm). As can be seen in Fig. 4-6, the lamellar spacing is larger at the slower growth rate and smaller at the faster growth rate. An interesting point to note here is that the Cr solid solution, rather than the Cr_3Si intermetallic, is the continuous phase (Fig. 4-6a) even though the latter has the higher volume fraction (~0.6).

Lamellar eutectic growth depends on an interplay between the diffusion required for phase separation and the energy required for formation of interphase boundaries. The interlamellar spacing is the result of a balance between two competing tendencies: on the one hand to minimize the interlamellar spacing in order to shorten the diffusion path in the liquid near the interface, and on the other hand to increase the spacing to minimize the interfacial area and hence the total interfacial energy. The most comprehensive

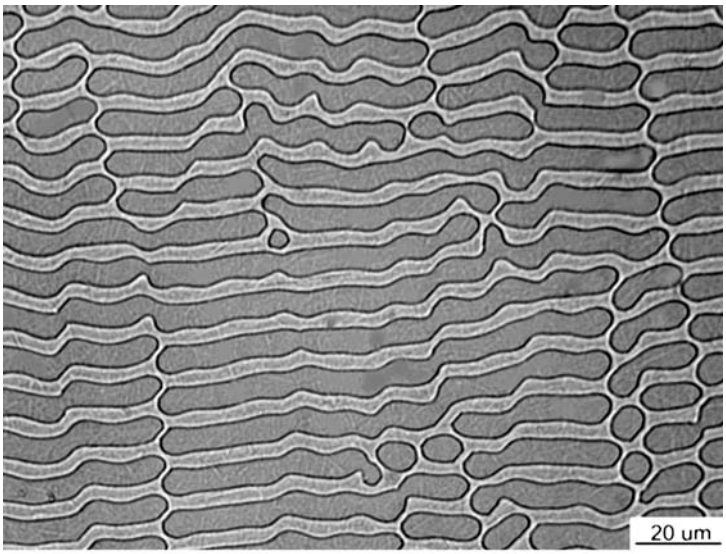

Figure 4-6. Optical micrograph showing (a) coarse lamellae (growth at 20mm/h, 60 rpm), and (b) fine lamellae (growth at 60 mm/h, 60rpm) in directionally solidified Cr-Cr_3Si eutectic alloys. The light and dark phase are Cr-rich solid solution and Cr_3Si, respectively.

treatment of this balance is that by Jackson and Hunt [9]. Under maximum growth velocity assumptions, they obtained the following relationship between growth rate R and spacing λ (Eq. 4-1).

$$\lambda^2 R = \frac{a^L}{Q^L} = constant \tag{4-1}$$

where Q^L and a^L are system constants related to the magnitudes of the liquidus slopes at the eutectic temperature, the composition difference between the two phases, their volume fractions, the solid-liquid interface energies of two phases, and the liquid–solid interface shape.

Figure 4-7 shows the change of spacing λ with changing growth rate R, from 20 mm/h to 100 mm/h. As can be seen in this figure, the data lie reasonably well on a straight line drawn through the origin when the values of the spacing λ are plotted against the reciprocal square root of growth rate $R^{-\frac{1}{2}}$ at both rotation rates, 10 and 60 rpm. The relation between the lamellar spacing and growth rate can be written as:

$$\begin{aligned} \lambda R^{1/2} &= 22.14\,\mu m \cdot mm^{1/2} / h^{1/2} @ 60 rpm \\ \lambda R^{1/2} &= 17.52 \mu m \cdot mm^{1/2} / h^{1/2} @ 10\, rpm \end{aligned} \tag{4-2}$$

Equation 4-2 shows that, at both rotation rates, the dependence of lamellar spacing on growth rate is in agreement with the Jackson-Hunt theory [9]. The fact that the straight line goes through the origin means that the solidifying melt does not have time to separate into two phases by solute inter-diffusion at infinitely fast growth rates. However, a quantitative comparison of the results of this study with the Jackson-Hunt theory is

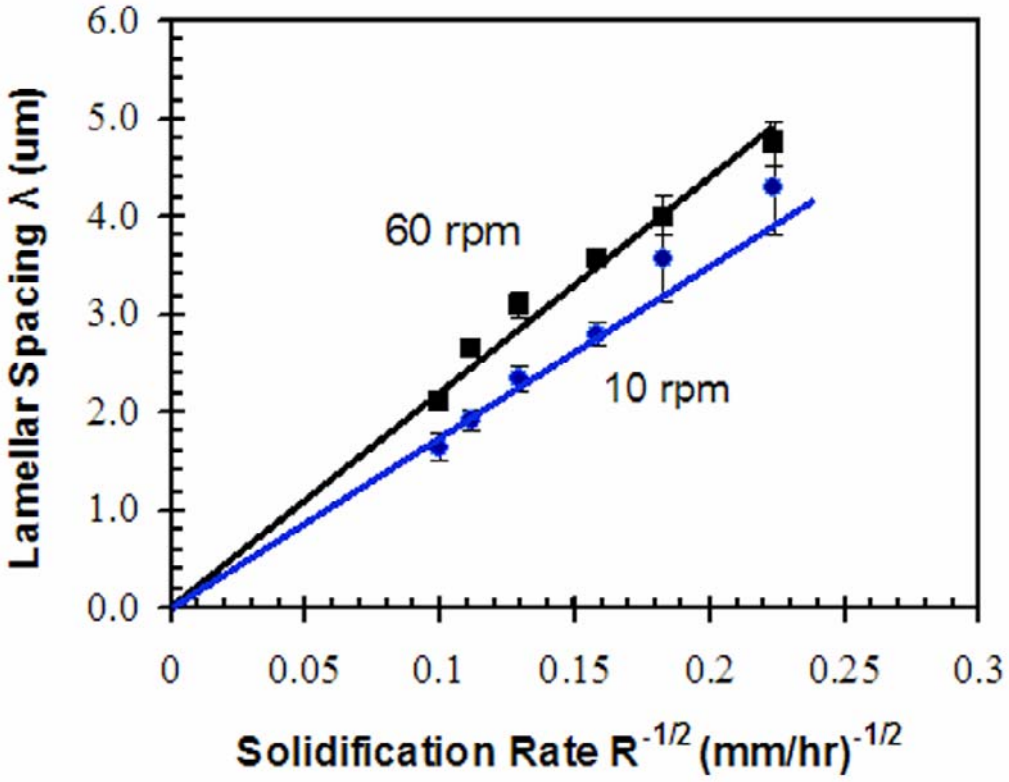

Figure 4-7. Effects of growth rate on lamellar spacings in directionally solidified Cr-Cr_3Si eutectic alloys at fixed rotation rates of 10 rpm and 60 rpm.

difficult because we lack precise values for the surface energies and other physical parameters required to calculate the constants in Eq. 4-1.

4.4 Effects of specimen rotation on lamellar structure

The influence of fluid convection is not included in the Jackson-Hunt theory. However, there is usually forced convection in the molten zone during solidification, especially during directional solidification using the floating zone technique in which specimen rotation is employed to get uniform heating. Limited theoretical analysis and experimental studies have shown that convective flow results in a change of eutectic spacing during directional solidification. Quenisset *et al.* [10, 11] first obtained a theoretical solution for the effect of convection on the eutectic spacing as follows:

$$\lambda^2 R = \frac{A}{1 - BG_u\lambda^2 / D} \qquad (4\text{-}3)$$

where G_u is the gradient of flow velocity, A and B are constants, and D is the solution diffusion coefficient. Their analysis was for an ideal system in which the volume fraction V_E=0.5. Baskaran and Wilcox [12] and Chandrasekhar *et al.* [13] extended the above analysis and obtained the following results:

$$\frac{\lambda}{\lambda_0} = 1 + A'\varepsilon_0^2 \qquad \text{at } V_E = 0.1 \sim 0.5 \qquad (4\text{-}4)$$

where $\varepsilon_0 = G_u\lambda_0^2 / D$, λ_0 is the eutectic spacing without convection, and A' is a constant.

The above theoretical analyses predict that the lamellar spacing increases with increasing rotation speed because the gradient of flow velocity, G_u, is proportional to the rotation speed [14].

The effects of rotation on the lamellar spacing of the Cr-Cr_3Si eutectic alloy at two fixed growth rates of R = 40 and 60 mm/h were examined by changing the rotation rate from 10 to 60 rpm. The results are shown in Fig. 4-8 which shows that the lamellar spacing increases with increasing rotation rate, in agreement with the theoretical predictions [10-13]. A possible explanation is that convective flow results in a slight shift of the solute concentration field in the liquid near the liquid-solid interface which tends to decrease the supercooling at the extreme condition of eutectic growth, thereby increasing the lamellar spacing [15].

4.5 Directional solidification of off-eutectic alloys

A fully eutectic-like structure, devoid of any cellular and dendritic regions, can be obtained not only in alloys having the eutectic composition but also at off-eutectic compositions if the growth conditions are carefully selected. Directional solidification of off-eutectic compositions is of interest because it can be used to control the volume fractions of the phases and, therefore, the properties of the composite. In order to obtain eutectic-like structures in off-eutectic alloys one has to maintain a stable, planar solid/liquid interface during directional solidification [16, 17]. According to the theory of constitutional supercooling, the growth condition for producing such an interface, in the absence of convection, is

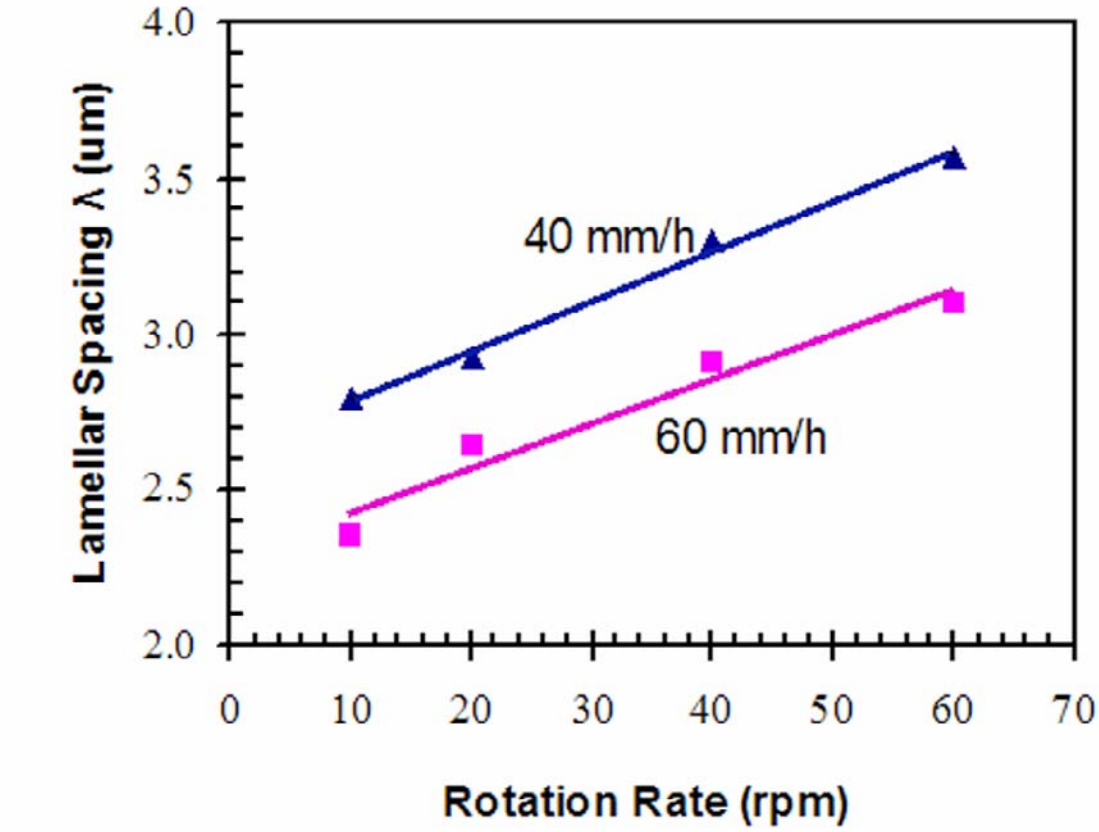

Figure 4-8. Effects of specimen rotation rate on lamellar spacings in directionally solidified Cr-Cr_3Si eutectic alloys at fixed growth rates of 40 mm/h and 60 mm/h.

$$\frac{G_L}{R} \geq -\frac{m_L\left(C_E - C_0\right)}{D} \qquad (4\text{-}5)$$

where G_L is the temperature gradient in the liquid ahead of the interface, m_L is the slope of the liquidus, C_E is the eutectic composition, and C_0 the initial composition of the solidifying alloy [18].

In this study, the temperature gradient is essentially constant (because all the experiments were performed in the same floating zone furnace). Therefore, from equation 4-5 we note that low growth rates are preferred for obtaining fully eutectic-like structures (lamellar or rod-like). Consistent with this line of reasoning, Figure 4-9 shows that for an off-eutectic (Cr-rich) alloy with a nominal composition of Cr-15% Si, the fully lamellar structure is replaced by a structure that contains both lamellae and pro-eutectic Cr-rich dendrites (Fig. 4-9a) at fast growth rates (100 mm/h) but, at low growth rates (20 mm/h), a fully lamellar structure can be obtained (Fig. 4-9b). At the eutectic composition, in contrast, a fully lamellar structure can be obtained at both these growth rates. By selecting a composition that is even more Cr-rich, a rod-like structure with the Cr solid-solution phase as the matrix and the Cr_3Si phase as fibers, can be produced in this Cr-Cr_3Si eutectic system. Figure 4-10a shows the rod-like structures for an alloy with a nominal composition of Cr-14% Si solidified at 20 mm/h. The measured volume fraction of the Cr_3Si phase is 0.59 in the Cr-15% Si alloy (Fig. 4-9b) and 0.48 in the Cr-14% Si alloy (Fig. 4-10a), compared to a volume fraction of 0.62 in the Cr-16% Si alloy (Fig. 4-1a). This result shows that it is possible to change the relative volume fractions of the eutectic phases by going to off-eutectic compositions, while still retaining a fully lamellar

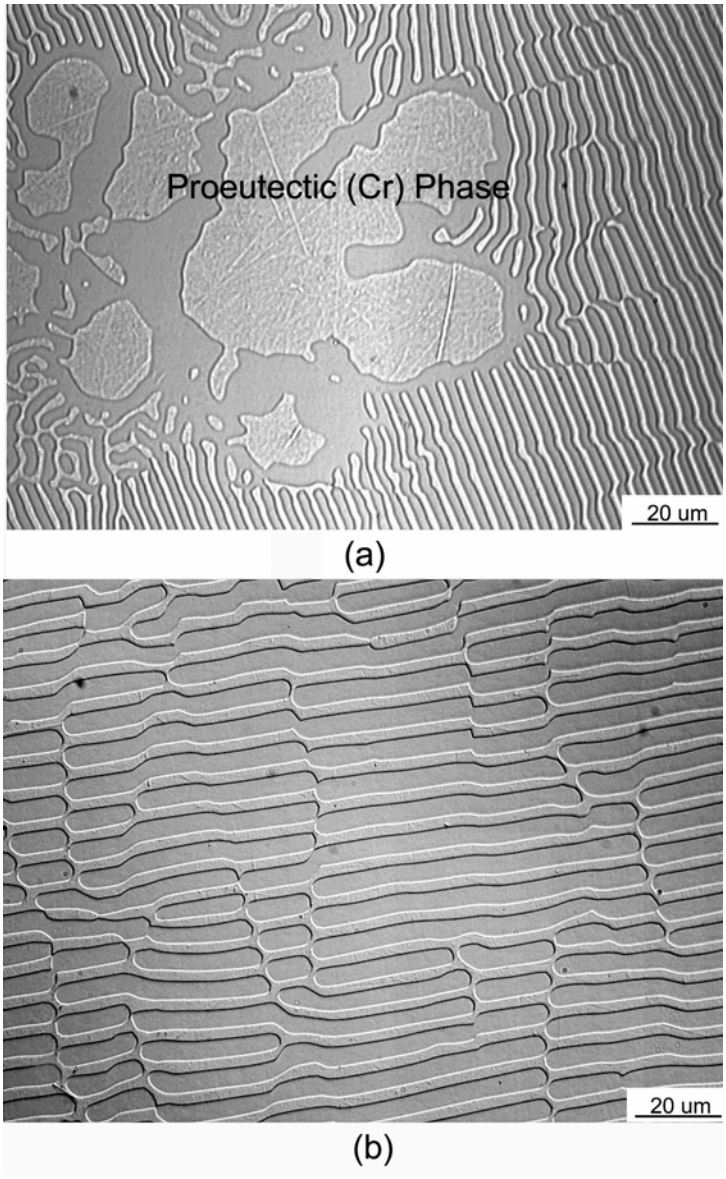

Figure 4-9. Microstructure of directionally solidified off-eutectic Cr-Cr_3Si alloys (Cr-15%Si): (a) dendritic primary Cr-rich phase embedded in the lamellar structure (growth at 100 mm/h, 60 rpm), (b) fully lamellar structure (growth at 20 mm/h, 60 rpm).

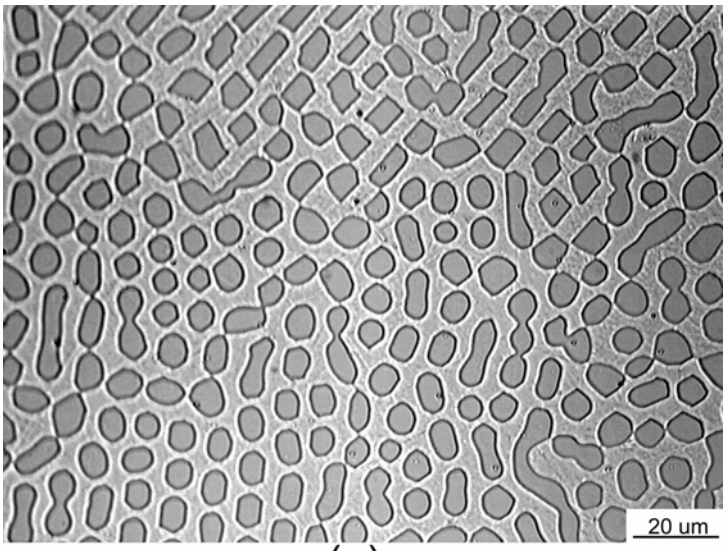

(a)

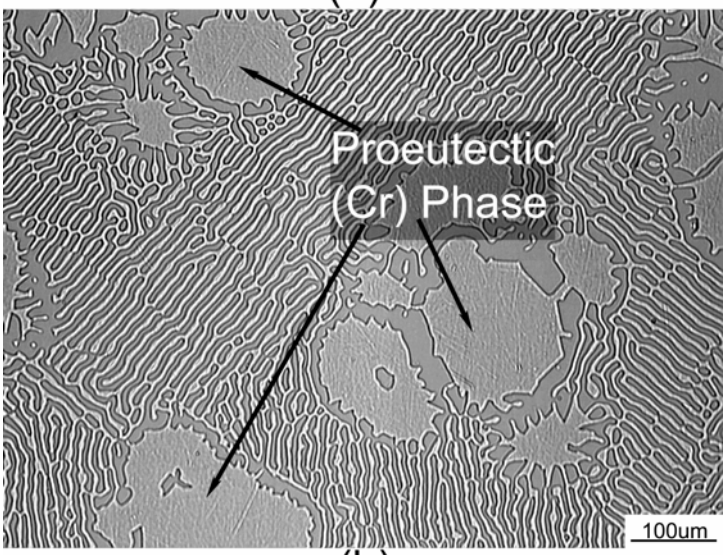

(b)

Figure 4-10. Micrographs showing (a) rod-like eutectic microstructures (Cr-14%Si), and (b) dendritic primary Cr-rich phase embedded in lamellar structure (Cr-13% Si) in directionally solidified off-eutectic alloys (growth at 20 mm/h, 60 rpm).

or rod-like microstructure.

Conditions promoting the formation of lamellar or rod-like structures have been discussed in detail by Jackson and Hunt [9]. The total interface energy is less for a rod-like morphology if the difference in the volume fractions of the two phases is large, and therefore a rod-like structure is preferred. When the volume fractions of the phases are approximately the same at the eutectic composition, there is a preference for the formation of lamellar structures. However, if the composition deviates too far from the eutectic composition, eutectic-like structures cannot be produced even at slow growth rates. Figure 4-10b shows a dendritic pro-eutectic Cr solid-solution phase embedded in the lamellar structure of an off-eutectic alloy with a nominal composition of Cr-13% Si directionally solidified at 20 mm/h.

The above results are summarized in Fig. 4-11, which is a structure selection map for different growth conditions and alloy compositions of Cr-Cr_3Si alloys. A coupled zone for eutectic-like structures (rod-like or lamellar) is also marked in Fig. 4-11 as a dotted line. It is clear that the range of growth rates over which eutectic-like structures are obtained is largest near the eutectic composition, in agreement with the theory of coupled growth of eutectic alloys [19, 20].

4.6 Conclusion

Directional solidification in an optical floating zone furnace can be used to produce well-aligned lamellar microstructures of Cr-Cr_3Si eutectic alloys. The structures consist of alternating lamellae of Cr_3Si and a Cr-Si solid solution. It is found that the Si

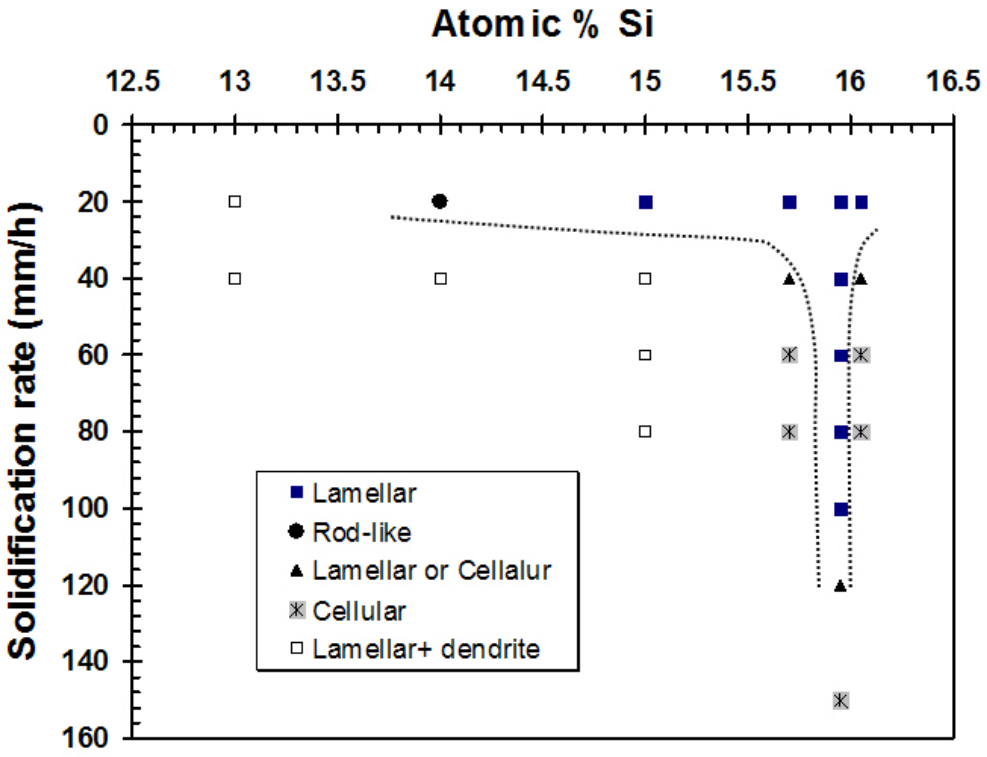

Figure 4-11. Structure selection map for various growth conditions and alloy compositions in Cr-Cr_3Si alloys. Dotted line shows schematically a coupled growth zone for eutectic-like structures (rod-like or lamellar). All alloys grown at a rotation speed of 60 rpm.

concentrations of the Cr solid solution and Cr_3Si are 7.9±0.2% and 21.1±0.2%, respectively.

By controlling the solidification conditions (growth rate and rotation speed), the lamellar spacing can be varied from ~1 - 5 μm. The relationship between the lamellar spacing (λ) and growth rate (R) is in agreement with the Jackson-Hunt theory ($\lambda \propto R^{-1/2}$). Furthermore, for a fixed growth rate, the lamellar spacing increases with increasing rotation rate. At very slow and very fast growth rates, the lamellar structure breaks down to produce degenerate and cellular structures, respectively.

In the lamellar eutectics, the growth direction of Cr_3Si was found to be <100> and that of the Cr solid solution <111>. However, different orientation relationships are observed, such as $(001)_{Cr_3Si} // (0\bar{1}\bar{1})_{Cr}$ and $(011)_{Cr_3Si} // (12\bar{3})_{Cr}$, with these planes parallel also to the lamellar boundaries.

Directional solidification of off-eutectic Cr-Cr_3Si alloys provides a way to change the relative volume fractions of the Cr solid-solution phase and the Cr_3Si intermetallic phase, but the range of solidification parameters yielding regular microstructures (lamellar or rod-like) is narrower for off-eutectic alloys than for the eutectic alloys.

Reference:

1. R. W. Kraft, D. L. Albright, *Transactions of the Metallurgical Society of AIME* 224(1962) 1176.
2. G. A. Chadwick, in "Liquids: structure, properties, solid interactions", T.J. Hughel editor, (Elsevier Publishing Company, Amsterdam (NY), 1965).
3. B. Chalmers, in "Principles of solidification", (John Wiley & Sons, Inc.,New York, 1964).
4. J. D. Hunt, K. A. Jackson, *Transactions of the Metallurgical Society of AIME* 236(1966) 843.
5. J. A. Sutliff, B. P. Bewlay, H. A. Lipsitt, *Journal of Phase Equilibria* 14 (1993) 583.
6. R. W. Kraft, D. L. Albrigh, *Transactions of the Metallurgical Society of AIME* 221 (1961) 95.
7. B. P. Bewlay, J. A. Sutliff, M. R. Jackson, K. M. Chang, *Materials and Manufacturing Processes* 9(1994) 89.
8. R. W. Kraft, D. L. Albright, *Transactions of the Metallurgical Society of AIME* 221(1961) 95.
9. K. A. Jackson, J. D. Hunt, *Transactions of the Metallurgical Society of AIME* 236(1966) 1129.
10. J. M. Quenisset, R. Naslain, *Journal of Crystal Growth* 54(1981) 465.
11. J. M. Quenisset, R. Sokolwski, M. E. Glicksman. *Journal of Crystal Growth* 63(1983) 389.
12. V. Baskaran, W. R. Wilcox, *Journal of Crystal Growth* 679(1984) 343.
13. S. Chandrasekhar, G. F. Eisa, W.R. Wilcox, *Journal of Crystal Growth* (76)1986 485.
14. V. G. Levich, in "Physicochemical Hydrodynamics", (Prentice Hall, Englewood Cliffs (NJ), 1962).

15. D. Ma, W. Q. Jie, Y. Li, S. C. Ng, *Acta Materialia* 46(1998) 3203.

16. F. R. Mollard, M. C. Flemings, *Transactions of the Metallurgical Society of AIME* 239 (1967) 1534.

17. F. R. Mollard, M. C. Flemings, *Transactions of the Metallurgical Society of AIME* 239(1967) 1526.

18. M. C. Flemings, in "Solidification Processing", (McGraw-Hill, Inc., New York, 1974).

19. W. Kurz, D. J. Fisher, *International Metals Reviews* 5/6(1979) 177.

20. W. Kurz, D. J. Fisher, in "Fundamentals of Solidification", (Trans Tech Publications Ltd. Rockport, 1984).

Part Five: Elastic Constants of Single Crystal Cr_3Si

The mechanical properties of the individual phases in the lamellar microstructures of Cr-Cr_3Si eutectics was characterized in order to understand the mechanical behavior of the composite materials. Nanoindentation, also known as depth-sensing indentation or instrumented indentation testing, is a relative new but powerful technique to characterize a variety of mechanical properties, especially hardness and elastic modulus (Young's modulus) [1]. One of the most commonly used methods for analyzing nanoindentation data is that of Oliver and Pharr [2]. However, the indentation modulus of a single crystal, or one single grain inside a polycrystal as given by the Oliver and Pharr method, is some polycrystalline average of the elastic constants for an anisotropic material. Vlassak and Nix [3-4] showed that the indentation modulus can be calculated for an arbitrary anisotropic solid and gave results that apply to solids with cubic crystal symmetry. Since Cr_3Si has the A15 cubic crystal structure, the Vlassak and Nix solution can be used to calculate the indentation modulus from the three independent elastic constants.

The elastic constants of single crystal Cr_3Si were reported in a previous study [5]; however, the quality of the crystal used in that study was not suspect, since some low angles grain boundaries were observable in the samples. In this study, a high-quality single crystal Cr_3Si was grown, and its elastic constants were determined by measuring the propagation velocities of ultrasonic waves. The elastic constants were then used to predict the indentation modulus which was compared with the experimental results obtained by nanoindentation along several crystal directions.

5.1 Theory and method

One of the most commonly used methods for analyzing nanoindentation load (P) and displacement (h) data is that of Oliver and Pharr [2]. In their method, the contact compliance C is independent of the shape of the indenter tip and is given by

$$C = \frac{dh}{dP} = \frac{\sqrt{\pi}}{2}\frac{1}{E_r}\frac{1}{\sqrt{A}} \tag{5-1}$$

where

$$\frac{1}{E_r} = \left(\frac{1-\upsilon^2}{E}\right)_{indenter} + \left(\frac{1-\upsilon^2}{E}\right)_{sample}, \tag{5-2}$$

P and h are the applied load and the indenter displacement, respectively, A is the projected contact area between the indenter and the specimen, and E and υ are Young's modulus and Poisson's ratio, respectively. The contact compliance can be measured as the reciprocal of the slope of the load-displacement curve at any given point on the unloading curve. The indentation modulus, $E/\left(1-\upsilon^2\right)$, can then be calculated from equation (5-1), provided the contact area, A, is known.

The indentation modulus for an isotropic material, $E/\left(1-\upsilon^2\right)$, depends only on E and υ and is independent of the shape of the indenter tip. In contrast, the indentation modulus for an anisotropic material is some average of its elastic constants, with the average expected to depend on the shape of the indenter tip, even for axisymmetric indenters [3, 4].

Vlassak and Nix [3, 4] derived the following formula for the contact compliance

for a flat punch and a paraboloid indenter on an anisotropic half space:

$$C = \frac{dh}{dP} = \frac{\sqrt{\pi}}{2}\frac{1}{E_r}\frac{1}{\sqrt{A}} \tag{5-3}$$

where

$$\frac{1}{E_r} = \left(\frac{1-\upsilon^2}{E}\right)_{indenter} + \left(\frac{1-\upsilon^2}{M}\right)_{sample} \tag{5-4}$$

and M is the indentation modulus of the material. Although these equations have the same forms as equations (5-1) and (5-2), the indentation modulus now is a complicated function of the elastic constants and indenter geometry. However, for a material with cubic symmetry, the indentation modulus of the *(hkl)* surface of a single crystal, $M_{(hkl)}$, can be written as the product of a correction factor $\beta_{(hkl)}$ and the indentation modulus of an isotropic, randomly oriented, polycrystalline aggregate consisting of a crystal with the same elastic properties as a single crystal. It can be written as:

$$M_{(hkl)} = \beta_{(hkl)}(E)_{isotropic} \tag{5-5}$$

where $\beta_{(hkl)} = a + c\left(A_f - A_0\right)^B$, and the constants a, c, A_0 and B are functions of the Poisson's ratio and anisotropy factor A_f of the crystal. Their values are given in reference [3]. The isotropic modulus, $(E)_{isotropic}$, can be approximated as:

$$(E)_{isotropic} = \frac{1}{2}(E_V + E_R) \tag{5-6}$$

where E_V and E_R are Voigt average modulus (iso-strain) and Reuss average modulus (iso-stress), respectively [6]. It should be noted that all the above equations are derived for a

circular flat punch. The indentation modulus for a triangular punch is about 5.8% higher than the modulus for a circular flat punch [3, 7].

5.2 Measurement of the elastic constants by ultrasonic technique

The measured speeds of ultrasonic wave propagation in single crystal Cr_3Si with axes orientated along [100] and [110], are shown in Table 5-1. The densities of these specimens measured by a pycnometer are also shown in the table. The densities of the two samples are identical to the theoretical (x-ray) density (6.46 g/cm^3).

The three independent elastic constant calculated using equations (2-3) - (2-5) and the parameters in Table 5-1 are:

$$\begin{aligned} C_{11} &= 415.5 \pm 1.5 \quad GPa \\ C_{12} &= 98.7 \pm 2.5 \quad GPa \\ C_{44} &= 12.7 \pm 0.3 \quad GPa \end{aligned} \tag{5-7}$$

The anisotropy factor for this material, $A_f = 2C_{44}/(C_{11} - C_{12})$, is equal to 0.82, indicating that it is not highly anisotropic. It should be noted that the elastic constants measured in this study agree with those reported in reference [5], although the crystal used in that study contained some low angle grain boundaries. The Young's moduli for the three different low-index directions are:

$$\begin{aligned} E_{[100]} &= 377 \quad GPa \\ E_{[110]} &= 332 \quad GPa \\ E_{[111]} &= 319 \quad GPa \end{aligned} \tag{5-8}$$

Table 5-1. The measured propagation velocities of ultrasonic waves in [100] and [110] single crystals.

Sample	*Axis Orientation*	*Length (mm)*	*Diameter (mm)*	*Density (g/cm^3)*	*Wave speed (m/s) (longitudinal)*	*Wave speed (m/s) (transverse)*
#1	[100]	10.24	12	6.46±0.1	8020	4464
#2	[110]	9.95	11	6.46±0.1	7726	---

and the isotropic modulus $(E)_{isotropic}$, defined by equation (5-6), is 342 GPa. This value will be used in equation (5-5) to predict the nanoindentation modulus.

5.3 Nanoindentation

Figure 5-1 shows a complete loading and unloading *P-h* curve from the nanoindentation of a {110} Cr_3Si single crystal. It is seen that the *P-h* curve exhibits a discrete "burst" in penetration at a specific indention load, also known as "pop-in" behavior. Pop-ins during nanoindentation have been observed in several materials, including tungsten [8], Mo_3Si [9] and Ni_3Al [10] single crystals. In a bulk single crystal, the mechanism of the pop-in has most often been associated with the nucleation of dislocations, or incipient plasticity [11-13]. The mechanisms governing the nucleation of

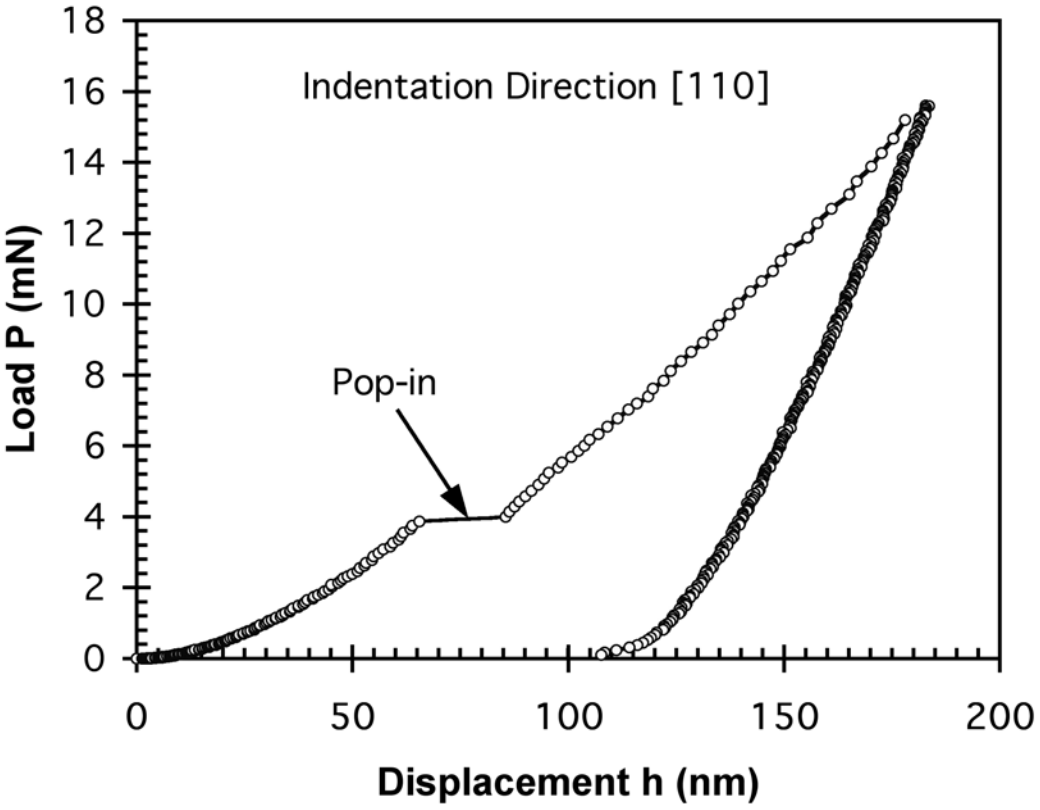

Figure 5-1. Nanoindentation load-displacement data for [110] Cr_3Si single crystal obtained with a Berkovich indenter showing pop-in behavior during loading.

dislocations during nanoindentation are not fully understood. It is believed that the contact between the indenter and the sample before first pop-in is fully elastic. The stress under the contact surface continuously increases as the indenter penetrates into the specimen. When the shear stress reaches some critical value, e.g. the theoretical strength, dislocations suddenly nucleate and move, resulting in a sudden increase in the penetration depth (pop-in). This pop-in behavior is discussed in detail in Part 6.

The indentation moduli M measured by nanoindentation (Eqs (5-3) and (5-4)) for the three low-index directions [110], [111] and [100], are shown in Fig. 5-2. For comparison the Young's modulus and the theoretical indentation modulus are also plotted in Figure 5-2. The dihedral angle in this figure is defined as the angle between the indentation direction and the [110] direction. As can be seen in the figure, the indentation modulus exhibits a polycrystalline averaging effect of the anisotropic elastic constants. The difference in the indentation modulus in the three different directions is smaller than that of Young's modulus. The indentation modulus predicted by assuming a triangular flat punch is the closest to the experimental results, which is consistent with the fact that the contact area of a Berkovich indenter is triangular rather than circular. The difference between the predicted and experimental modulus is within 5%, which is in the range of experimental error of nanoindentaion experiments.

The good agreement between the theoretical nanoindentation modulus and experimental results is potentially useful, especially if large single crystals are not available or if the material of interest is combined with other phases in a mutiphase microstructure. Nanoindentation can be used to investigate individual grains and phases

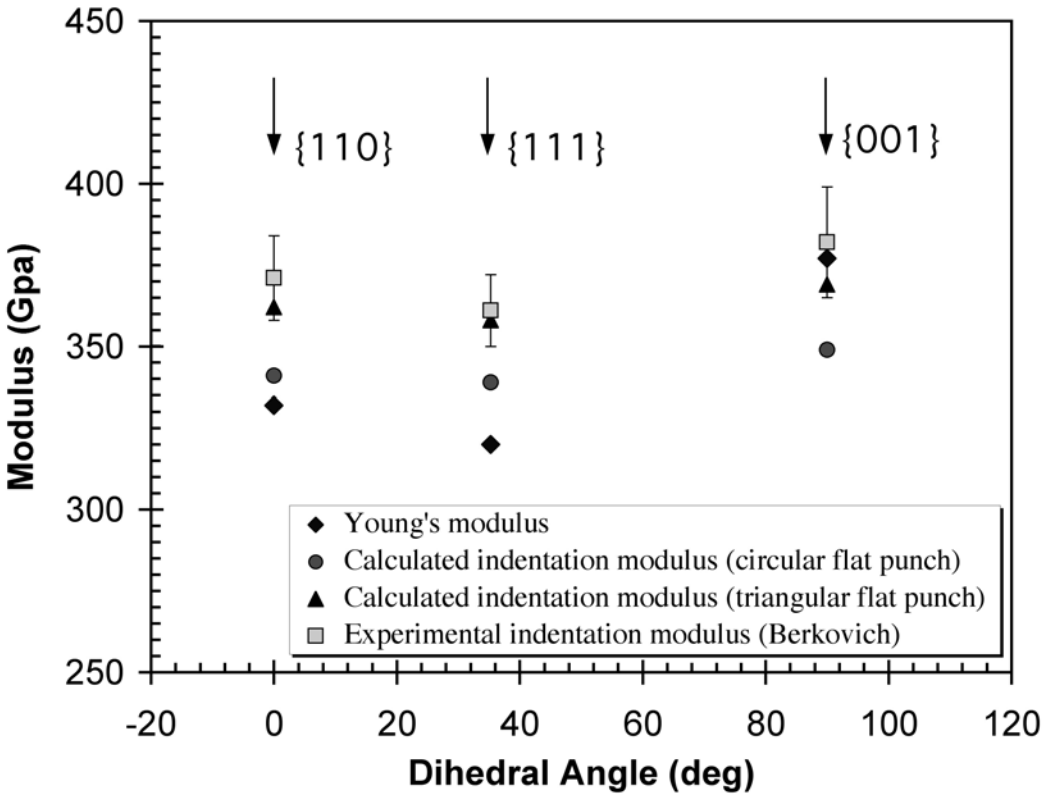

Figure 5-2. Comparison of the Young's modulus and theoretical predictions of indentation modulus with the experimental modulus obtained in nanoindentation experiments using a Berkovich indenter.

in polycrystalline and multiphase materials. Combined with crystal orientation measurement technology, e.g., electron back scattered diffraction patterns [14], the indentation modulus and direction can be used to calculate the elastic constants of an individual grain or phase, although a 'trial and error' procedure is needed. However, for many materials with high symmetry, e.g. cubic crystal systems, the 'trial and error' procedure is not cumbersome if a few simplifying assumptions are made [3-4]. Even for some complicated crystals, like β-silicon nitride, nanoindentation is still a useful tool to measure the elastic anisotropy [15].

5.4 Conclusion

A single crystal of Cr_3Si was grown and its elastic constants were determined by ultrasonic technique and nanoindentation. The elastic constants are: $C_{11} = 415.5 \pm 1.5 \ \ GPa$, $C_{12} = 98.7 \pm 2.5 \ \ GPa$, and $C_{44} = 128.7 \pm 0.3 \ \ GPa$.

The indentation modulus is a complicated average of the anisotropic elastic constants. Experimental results show good agreement with theoretical analysis, indicating that nanoindentation is a potentially useful tool for probing anisotropic elastic constants in small volumes.

Reference:

1. J. L. Hay, G. M. Pharr, in "ASM Handbook Volume 8: Mechanical Testing and Evaluation", 10th edition, H. Kuhn, D. Medkin, editors, (ASM International, Materials Park (OH), 2000), p. 232
2. W. C. Oliver, and G. M. Pharr, *Journal of Materials Research* 7 (1992) 1564.
3. J. J. Vlassak, W. D. Nix, *Journal of the Mechanics and Physics of Solids* 42(1994) 1223.
4. J. J. Vlassak, W. D. Nix, *Philosophical Magazine A* 67(1993) 1045.
5. P. Bujard, E. Walker, *Solid State Communications* 39(1981) 667
6. G. E. Dieter, in "Mechanical Metallurgy", 3th edition, (McGraw-Hill, New York, 1986).
7. R. B. King, *International Journal of Solids and Structures* 23(1987) 1657.
8. T. F. Page, W. C. Oliver, C. J. Mchargue, *Journal of Materials Research* 7(1992) 450.
9. J. G. Swadener, I. Rosales, J. H. Schneibel, *Materials Research Society Symposium Proceeding* 646(2001) p. N4.2.1
10. Y. L. Chiu, A. H. W. Ngan, *Acta Materialia* 50 (2002) 1599
11. A. Gouldstone, K. J. Van Vliet, S. Suresh, *Nature* 411(2001) 656.
12. S. Suresh, T. G. Nieh and B. W. Choi, *Scripta Materialia* 41(1999) 951.
13. A. Gouldstone, H. J. Koh, K. Y. Zeng, A. E. Giannakopoulos, S. Suresh, *Acta Materialia* 48(2000) 2277
14. A. J. Schwartz, M. Kumar, B. L. Adams, in "Electron Backscatter Diffraction in Materials Science", (Kluwer Academic Publishers, New York, 2000).
15. J. C. Hay, E. Y. Sun, G. M. Pharr, P. F. Becher, K. B. Alexander, *Journal of the American Ceramic Society* 81(1998) 2661.

Part Six: Analysis of Pop-in Behavior in Cr_3Si Single Crystals During Nanoindentation

The elastic constants of single crystal Cr_3Si were measured by nanoindentation and ultrasonic techniques in part 5. An anomalous phenomenon, a sudden displacement excursion (also called pop-in) [1-5], was observed during the loading portion of nanoindentation testing using a Berkovich diamond indenter. Experiments and simulations show that the pop-in behavior of single crystals is most likely related to dislocation nucleation (or incipient plasticity) in the crystal [4,5]. It is believed that the contact between the indenter and the specimen is perfectly elastic before the first displacement excursion or incipient plasticity. Therefore, an elastic load-displacement relationship and stress analysis is often used to explain this phenomenon.

Elastic contact between most commonly used Berkovich indenters and specimens is the result of a blunt indenter tip. Therefore, in many studies [1-5] the geometry of the indenter is simplified as a sphere. However, a large variety of tip radii, from ~20 nm to ~1000 nm, have been assumed in the literature [1-5]. In this study, the actual shape of the Berkovich indenter was determined by measuring the area function. Using this indenter shape, a series of nanoindentation tests were conducted on Cr_3Si single crystals. The load-displacement (P-h) curve, and the stress distribution in the single crystal under the indenter was analyzed in order to understand the pop-in behavior of Cr_3Si single crystals.

6.1 Theory and method

One of the most commonly used methods for analyzing nanoindentation load (P) and displacement (h) data is that of Oliver and Pharr [6]. In their method, hardness (H) and elastic modulus (E) are determined from indentation data obtained during one

complete cycle of loading and unloading. The fundamental relations from which H and E are determined are:

$$H = P/A \tag{6-1}$$

where P is the load and A is the projected area at that load, and:

$$E_r = \frac{\sqrt{\pi}}{2\beta}\frac{S}{\sqrt{A}} \tag{6-2}$$

where E_r is the reduced elastic modulus and β is a constant that depends on the geometry of the indenter. A reduced modulus, E_r, is used in Eq. 6-2 to account for the fact that elastic displacements occur in both the indenter and the specimen. The elastic modulus of the test materials, E_s, is calculated from E_r using

$$\frac{1}{E_r} = \frac{1-\upsilon_s^2}{E_s} + \frac{1-\upsilon_i^2}{E_i} \tag{6-3}$$

where E_s and υ_s are the elastic modulus and Poisson's ratio for the test materials, and E_i and υ_i are elastic modulus and Poisson's ratio of the indenter, respectively. For the commonly used diamond indenters, the elastic constants are: $E_i = 1141GPa$ and $\upsilon_i = 0.07$.

The contact stiffness (S) in Eq. 6-2 is established by analytically differentiating the unloading P-h curve and evaluating the result at the maximum depth of penetration, $h=h_{max}$, that is:

$$S = \left(\frac{dP}{dh}\right)_{h=h_{\max}} \tag{6-4}$$

The projected contact area (A), derived from the P-h data by means of an area function, which relates the cross-sectional area of the indenter (A) to contact depth (h_c).

An experimental procedure for determining the area function is discussed in detail by Oliver and Pharr [6]. The area function is written as:

$$A = f(h_c) \tag{6-5}$$

Once the area function and contact stiffness are known, the hardness and elastic modulus can be calculated from Eq. 6-1 and Eq. 6-2. Vice versa, if the elastic constants E_s and υ_s of the specimens are known, and the contact stiffness is calculated from the unloading *P-h* curve, the area function can be derived, thereby allowing the shape of the indenter to be calculated.

The problem of determining the stress distribution within an elastic half space when it is deformed by normal pressure against its boundary with a rigid punch is known as the Boussinesq problem [7]. For the axisymmetric Boussinesq problem with a punch of arbitrary profile, a solution for depth of penetration (*h*) and the total load (*P*) has been derived by Sneddon [8, 9] and generalized by Pharr [10] for the geometry shown in Fig. 6-1 [10]. A nondimensional variable $x = \rho/a$ is defined such that in the region of contact, $0 < x < 1$, the indenter shape is described by the function $z = f(x)$.

The expressions for both *P* and *h* are simple integrals of the shape function as given below:

$$h = \int_0^1 \frac{f'(x)dx}{\sqrt{1-x^2}} \tag{6-6}$$

and

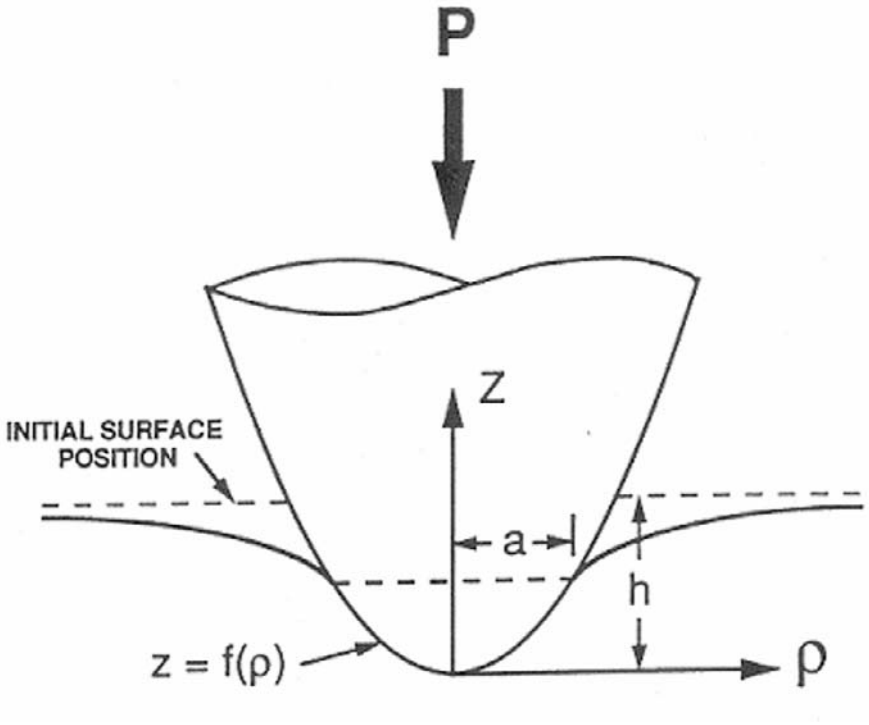

Figure 6-1. Geometry of an axisymmetric indenter in Sneddon's analysis. [10]

$$P = 2E_r a \int_0^1 \frac{x^2 f'(x) dx}{\sqrt{1-x^2}} \qquad (6\text{-}7)$$

where *f'(x)* is the first derivative of *f(x)* with respect to *x*, and *a* is contact radius (as shown in Fig. 6-1)

In Eq. 6-6 and Eq. 6-7, the *P-h* relationship is given in terms of reduced modulus E_r and indenter shape $f(x)$. The load and displacement relationship for many punches with simple geometries can conveniently be written as

$$P = Ch^m \qquad (6\text{-}8)$$

where *C* and *m* are constants. Values of the constant *C* and exponent *m* for some common punch geometries are listed in Table 6-1.

Table 6-1. Summary of the load-displacement relationships for three indenter geometries.

Indenter shape	Constant C	Exponent m	Notes
Flat cylinder	$2E_r a$	1	a is the radius of the cylinder
Sphere	$\frac{4}{3} \cdot \sqrt{R} \cdot E_r$	1.5	R is the radius of the sphere
Cone	$\frac{2}{\pi} \cdot E_r \cdot \cot\theta$	2	θ is the semivertical angle of the cone

The nature of the stresses arising from the contact between two elastic bodies is of considerable importance for understanding incipient plasticity during nanoindention. However, the analysis and calculation of the complete stress field arising from indentation with an indenter of general shape is mathematically quite complicated and, in most cases, an analytical solution is impossible. However, for indenters with simple geometries, such as sphere, cylindrical flat punch and cone, the complete stress field can be described by an analytical solution. One such example is the stress caused by a spherical indenter, known as the Hertz stress distribution. [12] The non-zero components of the stress field within the interior of the specimen in a cylindrical coordinate system, $\sigma_{rr}, \sigma_{\theta\theta}, \sigma_{zz}$ .and τ_{rz}, can be calculated from Eq. 6-9 through Eq. 6-14 [13], and the results are plotted as contours in Fig. 6-2.

$$\frac{\sigma_{rr}}{p_m} = \frac{3}{2}\left\{\frac{1-2\upsilon}{3}\frac{a^2}{r^2}\left[1-\left(\frac{z}{u^{1/2}}\right)^3\right]+\left(\frac{z}{u^{1/2}}\right)^3\frac{a^2u}{u^2+a^2z^2}+ \frac{z}{u^{1/2}}\left[u\frac{1-\upsilon}{a^2+u}+(1+\upsilon)\frac{u^{1/2}}{a}\tan^{-1}\left(\frac{a}{u^{1/2}}\right)-2\right]\right\} \tag{6-9}$$

$$\frac{\sigma_{\theta\theta}}{p_m} = -\frac{3}{2}\left\{\frac{1-2\upsilon}{3}\frac{a^2}{r^2}\left[1-\left(\frac{z}{u^{1/2}}\right)^3\right]+ \frac{z}{u^{1/2}}\left[2\upsilon+u\frac{1-\upsilon}{a^2+u}-(1+\upsilon)\frac{u^{1/2}}{a}\tan^{-1}\left(\frac{a}{u^{1/2}}\right)\right]\right\} \tag{6-10}$$

$$\frac{\sigma_{zz}}{p_m} = -\frac{3}{2}\left(\frac{z}{u^{1/2}}\right)^3\left(\frac{a^2u}{u^2+a^2z^2}\right) \tag{6-11}$$

$$\frac{\tau_{rz}}{p_m} = -\frac{3}{2}\left(\frac{rz^2}{u^2+a^2z^2}\right)\left(\frac{a^2u^{1/2}}{a^2+u}\right) \tag{6-12}$$

where:

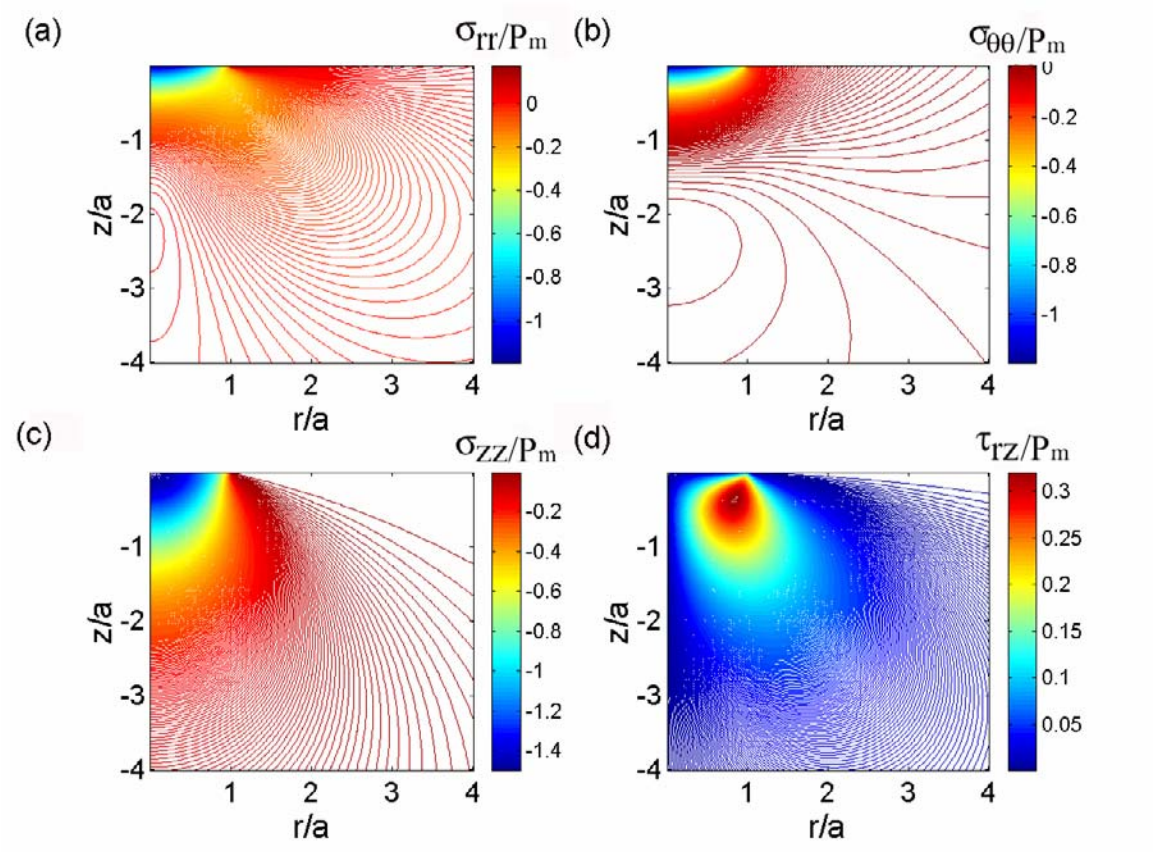

Figure 6-2. Contour plot showing Hertz stress distribution (a) σ_{rr}, (b) $\sigma_{\theta\theta}$, (c) σ_{zz}, and (d) τ_{rz}.

$$u = \frac{1}{2}\left\{\left(r^2 + z^2 - a^2\right) + \left[\left(r^2 + z^2 - a^2\right)^2 + 4a^2z^2\right]^{1/2}\right\} \qquad (6\text{-}13)$$

and the mean pressure is :

$$p_m = \left(\frac{16PE_r^{\,2}}{9\pi^3 R^2}\right)^{1/3} \qquad (6\text{-}14)$$

Previous studies showed that pop-ins occur when the maximum resolved shear stress on some particular slip system reaches a critical value which is approximately the theoretical shear strength [4, 5]. The calculated resolved shear stress τ_R, on any slip system with unit vector $\vec{n}$ as the normal direction and a unit vector $\vec{s}$ as the slip direction, is given by the sum of the contributions from all the non-zero stress components. For the stress arising by indenting an elastic half-space with a spherical indenter, the non-zero stress components are σ_{rr}, $\sigma_{\theta\theta}$, σ_{zz} .and τ_{rz} in cylindrical coordinates. Therefore, the resolved shear stress τ_R has the form:

$$\tau_R = c_{rr}\sigma_{rr} + 2c_{rz}\tau_{rz} + c_{\theta\theta}\sigma_{\theta\theta} + c_{zz}\sigma_{zz} \qquad (6\text{-}15)$$

The coefficients are the Schmid factors given by:

$$\begin{cases} c_{rr} = \vec{n}\cdot\vec{r}\times\vec{s}\cdot\vec{r} \\ c_{rz} = \dfrac{1}{2}\left[(\vec{n}\cdot\vec{r}\times\vec{s}\cdot\vec{z}) + (\vec{n}\cdot\vec{z}\times\vec{s}\cdot\vec{r})\right] \\ c_{\theta\theta} = \vec{n}\cdot\vec{\theta}\times\vec{s}\cdot\vec{\theta} \\ c_{zz} = \vec{n}\cdot\vec{z}\times\vec{s}\cdot\vec{z} \end{cases} \qquad (6\text{-}16)$$

where $\vec{r}$, $\vec{\theta}$ and $\vec{z}$ are the unit direction vectors of the stress components σ_{rr}, $\sigma_{\theta\theta}$ and σ_{zz}, respectively.

For the Cr_3Si single crystal with A15 crystal structure, the slip system is $(100)[001]$ [14]. For simplicity, the material is assumed to be elastically isotropic with E=342 GPa and υ=0.2. The maximum resolved shear stresses when indenting with a spherical indenter along the [001], [110] and [111] directions can be calculated from Eq. 6-15 and 6-16 as:

$$|\tau_{R,\max}|_{[100]} = 0.318 p_m \quad (6\text{-}17)$$

$$|\tau_{R,\max}|_{[110]} = 0.465 p_m \quad (6\text{-}18)$$

$$|\tau_{R,\max}|_{[111]} = 0.368 p_m \quad (6\text{-}19)$$

where p_m is the mean pressure under the applied load (Eq. 6-14).

6.2 Finite element simulation

The stresses arising from the contact between the indenter and specimens was simulated using the Nano SP2 package (Nano Instruments Innovation Center, MTS corporation, Knoxville, TN). The Nano SP2 package, which has the capability of using the precise area function (Eq. 6-5) to model the indenter tip, is a finite element simulation software based on the COSMOS (Structural Research & Analysis Corp., Los Angeles, CA) finite element code. The specimen was modeled as a large semi-sphere with radius 30,000 nm represented by approximately 9000 four-node axisymmetric elements. The simulations were performed to specific displacements where the first pop-in observed experimentally. An example of the detailed finite element mesh is shown in Fig. 6-3. Near the region of contact, very fine elements ~3.6 nm in width were used to achieve

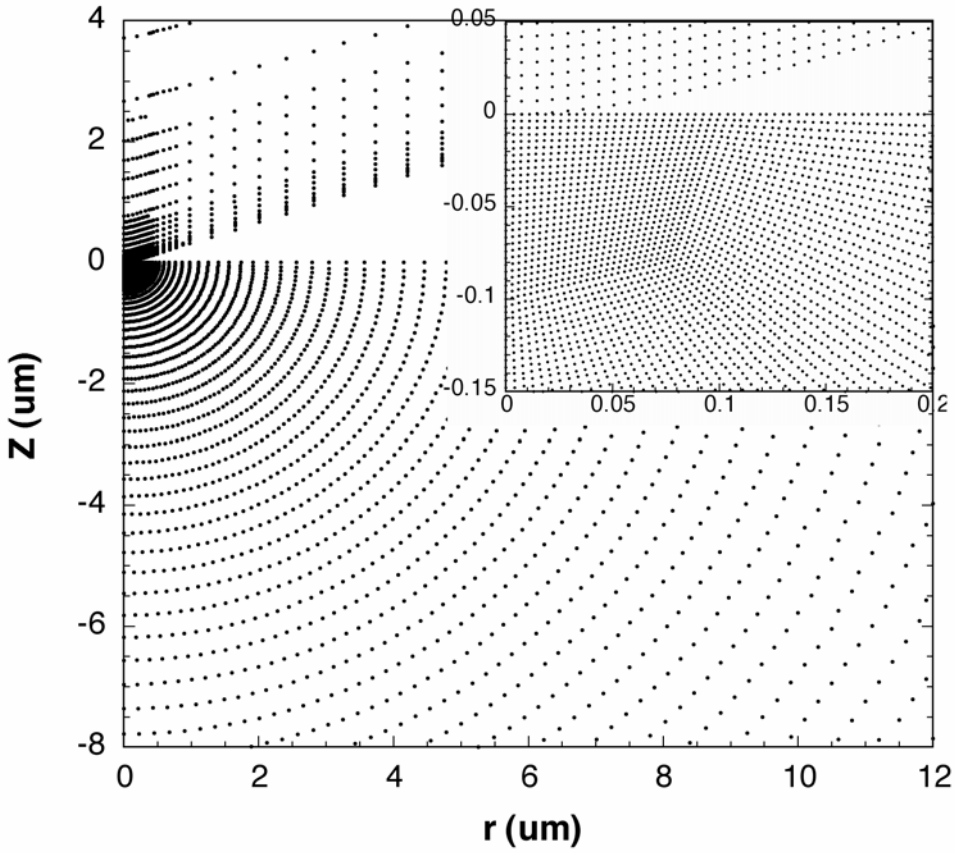

Figure 6-3. The finite element mesh used in the simulation: the figure in the upper corner shows details of the mesh near the region of contact.

accurate determination of the stress distributions. Away from the contact, a progressively coasrser mesh was employed along the radial direction. For simplicity, an isotropic modulus and Poisson's ratio (E_{iso}=342 GPa and $\upsilon = 0.2$) for the specimen were used in the simulation.

6.3 Analysis of the indenter shape

The area function of the indenter can be determined by using methods employing Eqs. 6-2, 6-3 and 6-4 by indenting a fused quartz standard sample (E_s=72 *GPa* and $\upsilon_s = 0.17$). Figure 6-4 shows the relationships $A = f(h_c)$ between the projected contact area (A) and the contact depth (h_c) for a range of contact depths below 100 nm. A simple equation, which is also plotted in Fig. 6-4, can describe the experimentally determined area function of the indenter used in this study, namely:

$$A = 25.97h_c^2 + 1457.3h_c \qquad (6\text{-}20)$$

Two other expressions for the area function are: (a) $A = 24.56h_c^2$, for an ideal sharp Berkovich indenter (normally treated as a cone with a semivertical angle $\theta = 70.3^\circ$, and (b) $A = 2\pi Rh_c - \pi h_c^2$, for an ideal spherical indenter with radius R. Equation 6-20, which describes the area function of the indenter used in this study, is a linear combination of these two expressions. Thus, when the contact area h_c is small, the term $1457.3h_c$ dominates in Eq. 6-20, which then is identical to the area function of a sphere with radius *R=232* nm. On the other hand, when the contact area is large, the term $25.97\,h_c^2$ dominates, which is the area function of an ideal sharp cone with semivertical angle

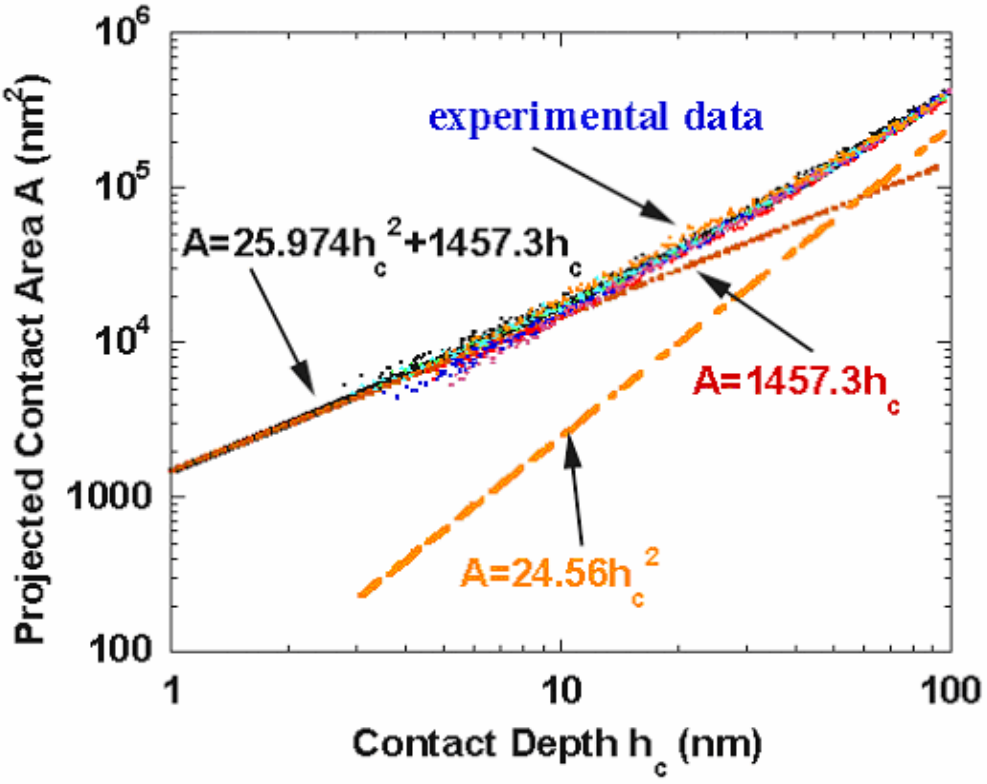

Figure 6-4. The area function used in this study is $A = 25.97h_c^2 + 1457.3h_c$. Two other area functions $A = 1457.3h_c$ (R=232 nm sphere) and $A = 24.56h_c^2$ (ideal Berkovich indenter) are also plotted in this figure for comparison.

$\theta = 70.8^\circ$. Therefore, the geometry of the indenter used in this study can be modeled as a cone with a rounded tip for contact depths below 100 nm. The relationship between the radius of the contact circle (a) and the contact depth (h_c) is expressed in Eq. 6-21:

$$a^2 = \frac{25.974}{\pi} h_c^2 + \frac{1457.3}{\pi} h_c = C_1 h_c^2 + C_2 h_c \qquad (6\text{-}21)$$

The shape of the indenter is given by Eq. 6-22, and the result is plotted in Fig.6- 5. As can be seen in the figure, the indenter used in this study can be treated as a sphere with a radius about *232* nm only when the contact depth is below *10* nm.

$$z = f(\rho) = \frac{-C_2 + \sqrt{C_2^2 + 4C_1 \rho^2}}{2C_1} \qquad (6\text{-}22)$$

It is noted that this function (Eq. 6-22), is smooth (i.e., infinitely differentiable) and *f(0)=0*. Therefore, Eq. 6-6 and Eq. 6-7 can be used to calculate the *P-h* relationship when a load is applied with this indenter onto an elastic half space.

6.4 Load-displacement relation under elastic contact

The indenter shape used in this study is well described by Eq. 6-3. Because both *h* and *P* can be expressed in terms of simple integrals of the shape functions by means of Eq. 6-7 and Eq. 6-6, the *P* - *h* curve for elastic contact can be determined. By differentiating Eq. 6-22 with respect to *x* and substituting into Eq. 6-6 and 6-7, the load is described by:

$$P = 2E_r \left\{ \frac{aC_2}{4C_1} + \frac{4C_1 a^2 - C_2^2}{16C_1\sqrt{C_1}} \left[\frac{\pi}{2} - \arcsin\left(\frac{C_2^2 - 4C_1 a^2}{4C_1 a^2 + C_2^2} \right) \right] \right\} \qquad (6\text{-}23)$$

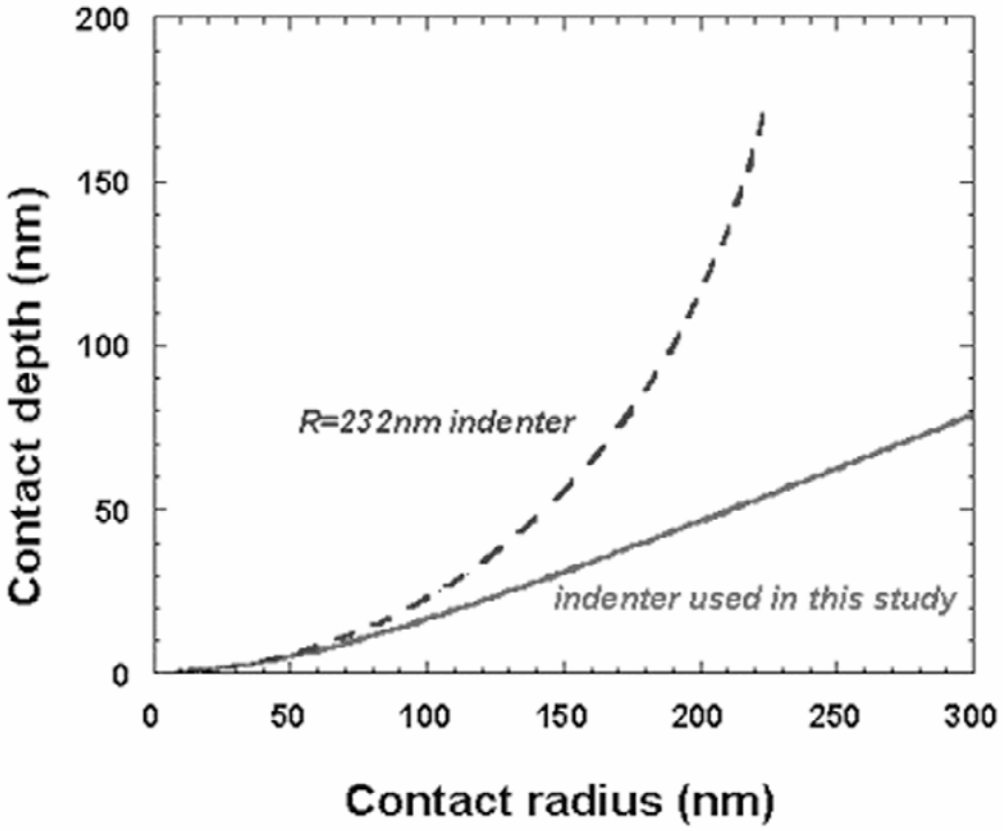

Figure 6-5. The shape of the indenter used in this study with a tip radius about 232 nm.

and displacement by:

$$h = \frac{a}{2\sqrt{C_1}}\left[\frac{\pi}{2} - \arcsin\left(\frac{C_2^2 - 4C_1a^2}{4C_1a^2 + C_2^2}\right)\right] \qquad (6\text{-}24)$$

where C_1 and C_2 are the same constants as those in Eq A.3.2 and A.3.3. Thus, both P and h are functions only of the contact radius a. By eliminating a in Eq. 6-23 and 6-24, the P-h relationship is determined.

A typical load-displacement curve for a maximum load P_{max} = *15* mN during indentation of the Cr_3Si single crystal along the [110] direction is shown in Fig. 6-6. It is clear that the pop-in occurs at a load P = ~3.9 mN. In addition, the predicted elastic loading P-h curve obtained by eliminating the contact radius and substituting the reduced modulus E_r in the Eq. 6-23 and 6-24, is also plotted in Fig. 6-6. It can be seen that the theoretical *P-h* curve matches the experimental loading curving very well before the pop-in occurs. Perfectly elastic loading and unloading curves for a maximum load P_{Max} = *3* mN are shown in Fig. 6-7. The results shown in Fig. 6-6 and 6-7 indicate that the contact between the specimen and the indenter before the first pop-in occurs is perfectly elastic, and the load-displacement relationship can be well described by Sneddon's equation (Eq. 6-23 and 6-24). In addition, it is noted that the elastic load-displacement relationship follows a power law relation (Eq. 6-8), $P=Ch^{1.69}$. The exponent m (1.69) is neither 1.5 (for a spherical indenter) nor 2 (for a conical indenter).

The elastic modulus and nanoindentation hardness measured along the three low-index directions [100], [110] and [111], are shown in Table 6-2 and 6-3 for a maximum load of 15 mN. All the data are calculated by using a Poisson's ratio of $\upsilon = 0.2$. It is

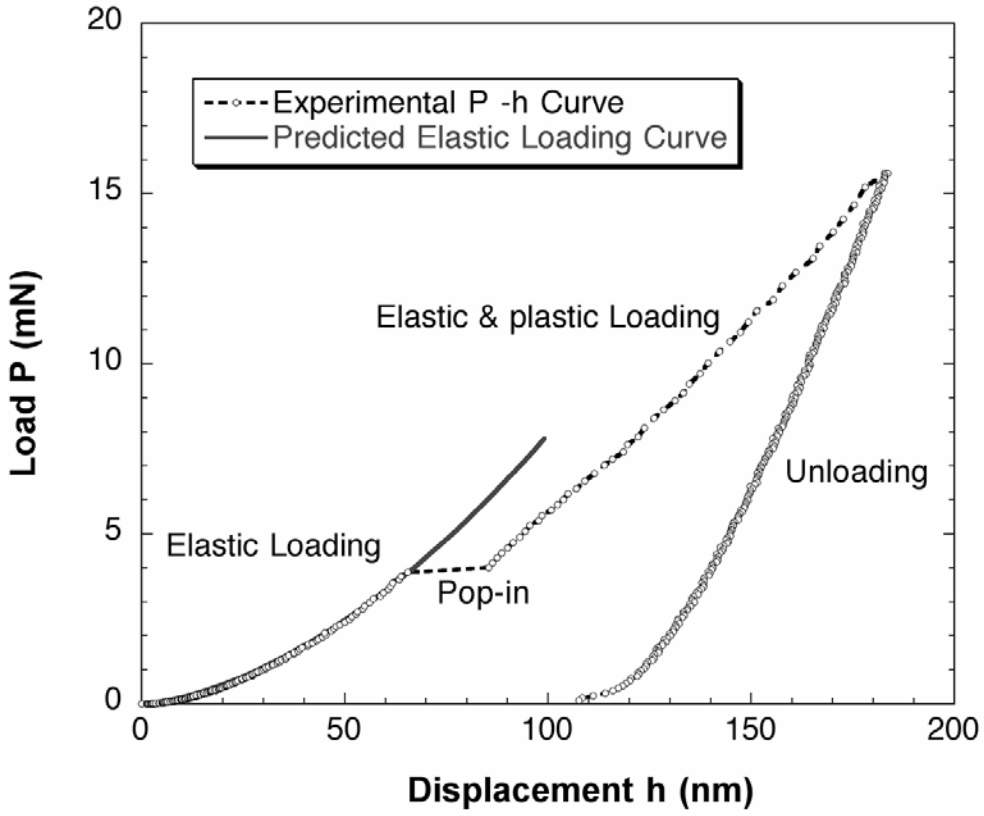

Figure 6-6. Load and displacement curve obtained in Cr_3Si single crystal showing pop-in behavior during loading. The loading curve before pop-in can be reproduced by Sneddon's elastic contact solution.

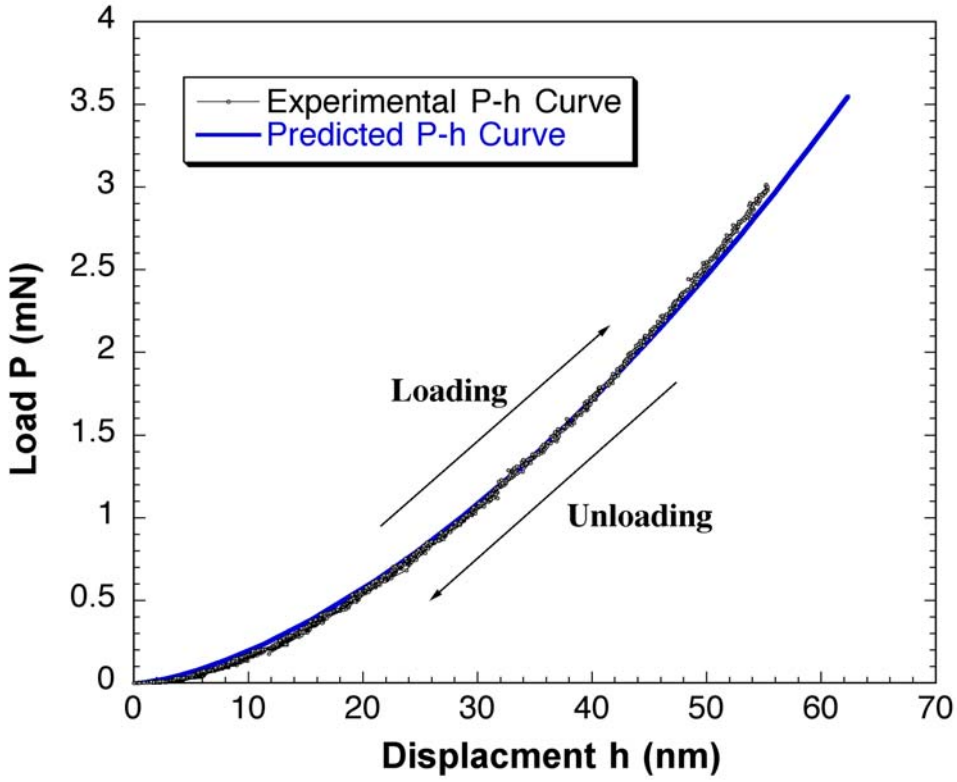

Figure 6-7. Perfectly elastic loading and unloading curve below a maximum load of 3 mN.

Table 6-2. Measured nanoindentation modulus and hardness of single crystal Cr_3Si.

Indentation direction	[100]	[110]	[111]
Modulus (GPa)	382±17	367± 13	361±11
Hardness (GPa)	22.5±0.8	20.3±1.1	21.6±0.9

Table 6-3. The measured load, displacement at first pop-in and the calculated maximum resolved shear stress at pop-in load.

Indentation direction	[100]	[110]	[111]
Load *P* at pop-in (measured) (mN)	5.41	3.91	4.67
Displacement *h* at pop-in (nm)	83	61	74
Contact radius at pop-in (nm)	197	158	184
Effective sphere radius $R_{eff} = \frac{a^2}{h}$ (nm)	468	409	458
Max. τ_R (FEM) (GPa)	18.1	22.3	21.7
Max. τ_R (Hertz R=232nm) (GPa)	23.93	31.41	26.37
Max. τ_R (Hertz R=R_{eff}) (GPa)	14.61	21.35	16.63

observed that the pop-in occurs at different loads in different indentation directions. The pop-in loads are 5.41, 3.91 and 4.67 mN for the [100], [110] and [111] directions, respectively (Table 6-3).

6.5 Stress analysis

The stress field distribution within the interior of the specimen is of interest. Figure 6-8 shows contour plots of the 2D finite element simulation of the non-zero stress components for an indent depth of 60nm. The stress field arising from the indenter tip described in this study is similar to that of a spherical tip. The maximum absolute values of σ_{rr}, $\sigma_{\theta\theta}$ and σ_{zz} are along the *z* axis, and somewhere under the surface near the contact edge for τ_{rz} (Fig. 6-2 & 6-8). The normal pressure(σ_{zz}) on the surface along the *z* direction is a finite value rather than the infinite value for an ideal sharp indenter.

The maximum resolved shear stress on the (100)[001] slip system was calculated from the results of FEM analysis for specific indentation displacements of 83, 61 and 74 nm for different indentation directions [100], [110] and [110], and the results are listed in Table. 6-3. The position of maximum resolved shear stress is plotted in Fig. 6-9.

It is clear that the maximum resolved shear stress occurs at different positions beneath the contact surface when indenting along the [100] (Fig 6-9a.), [110] (Fig. 6-9b), and [110] (Fig. 6-9c) directions. The difference between all three maximum resolved shear stresses and the estimated theoretical strength of Cr_3Si (Eq. 6-25 [15]), or the stress for homogeneous nucleation of a dislocation τ_{th} is within 10%.

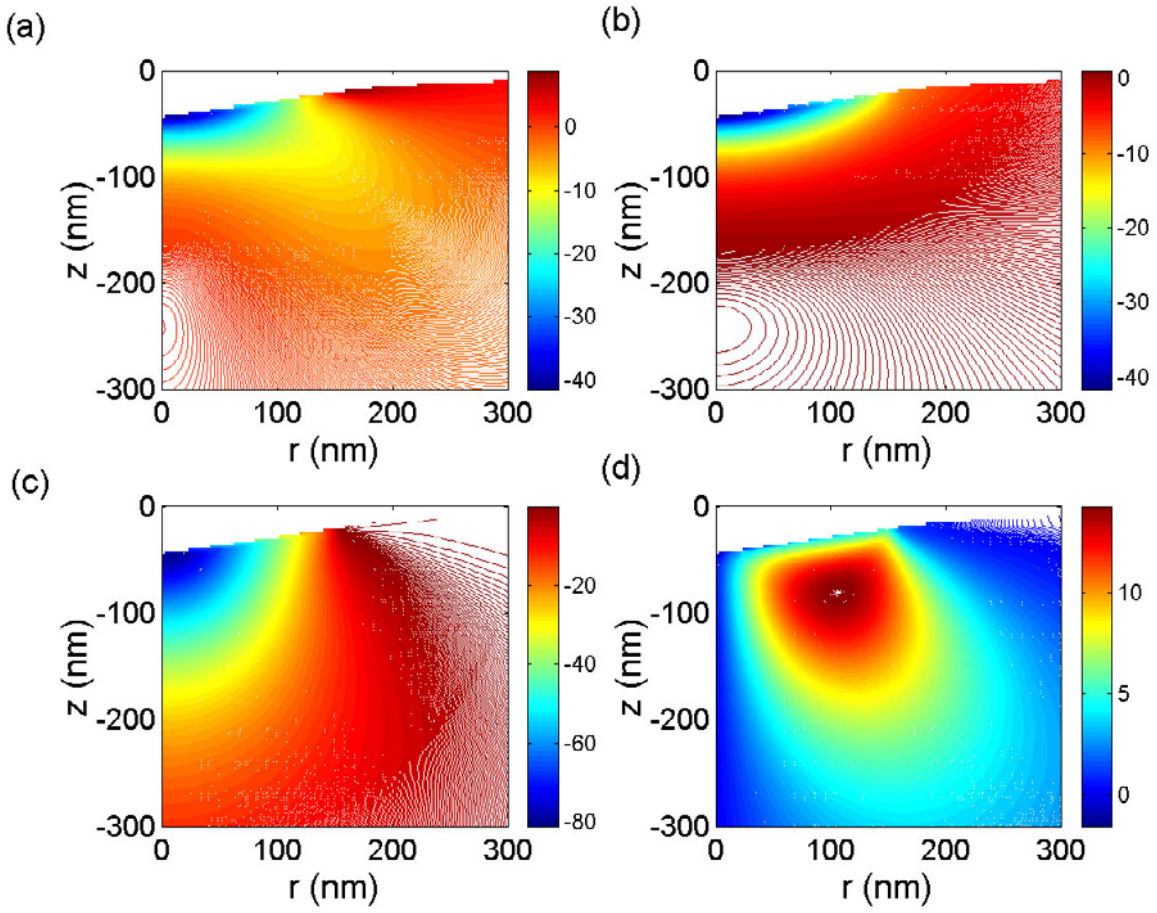

Figure 6-8. Contour plot showing 2D finite element simulation of the non-zero stress components for indentation depths at 60nm: (a) σ_{rr}, (b)$\sigma_{\theta\theta}$, (c)σ_{zz}, and (d)τ_{rz}.

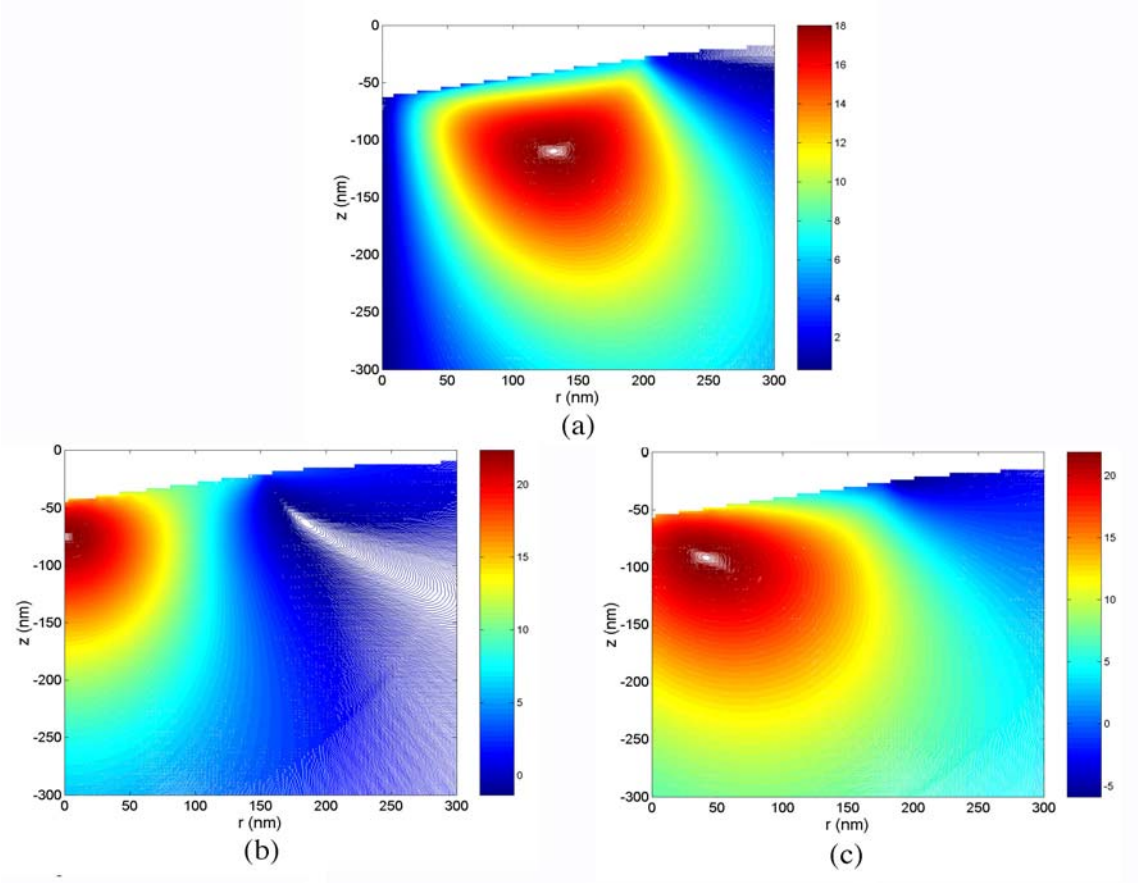

Figure 6-9. Contour plot showing that the maximum resolved shear stress occurs at different positions beneath the contact surface when indenting along the (a) [100], (b) [110], and (c) [110] directions.

$$\tau_{th} = \frac{G}{2\pi} = 20.53GPa \qquad (6\text{-}25)$$

where G is the shear modulus of Cr_3Si, which is 129 GPa.

The perfectly elastic contact between the indenter and specimen before pop-in and the maximum resolved shear stress at the pop-in load which is comparable to the theoretical strength, indicate that the pop-in behavior observed in this study may be able to probe incipient plasticity in Cr_3Si single crystals, and the maximum resolved shear stress is a good estimate of the stress for homogeneous dislocation nucleation.

For comparison, the resolved shear stress calculated using the commonly used Hertz stress field is also listed in Table. 6-3. Here two sphere radii are used for calculating the maximum resolved shear stress with Eq. 6-17, 6-18 and 6-19, namely the tip radius (*232* nm) and effective radius (R_{eff}), respectively. The effective radius is defined as the radius of a sphere which has the same contact radius (a) at the same displacement (h), [11] that is:

$$R_{eff} = \frac{a^2}{h} \qquad (6\text{-}26)$$

The results listed in Table. 6-3 show that in all three directions, the maximum resolved shear stress is overestimated when the tip radius is used for calculation, and underestimated when the effective tip radius is used for calculation. The overestimate can be as large as 40% and the under estimate can be as large as 23%.

6.6 Conclusion

Single crystal Cr_3Si was grown in a high temperature optical floating zone furnace, and nanoindentation testing performed along the [100], [110], and [111] crystal directions using a Berkovich indenter. The Berkovich indenter was found to be well described by the area function $A = 25.97h_c^2 + 1457.3h_c$, which can be modeled as a cone with a rounded tip for contact depths less than 100 nm.

Pop-ins were observed during the loading portion of nanoindentation testing, and the load-displacement relationship before pop-in can be well described in terms of a perfectly elastic contact using Sneddon's equation.

The stress distribution in the specimen at the pop-in load was simulated by finite element analysis. The difference between the maximum shear stress resolved along the slip systems of the crystal and the theoretical shear strength ($G/2\pi$) are within 10%.

Collectively, these results indicate that the pop-in is caused by dislocation nucleation (incipient plasticity) at the theoretical strength of the material.

References:

1. T. F. Page, W. C. Oliver, C. J. Mchargue, *Journal of Materials Research* 7(1992) 450.
2. J. G. Swadener, I. Rosales, J. H. Schneibel, *Materials Research Society Symposium Proceedings* 646(2001) p. N4.2.1
3. Y. L. Chiu, A. H. W. Ngan, *Acta Materialia* 50 (2002) 1599
4. A. Gouldstone, K. J. Van Vliet, S. Suresh, *Nature* 411(2001) 656.
5. S. Suresh, T. G. Nieh and B. W. Choi, *Scripta Materialia* 41(1999) 951.
6. W. C. Oliver, G. M. Pharr, *Journal of Materials Research* 7 (1992) 1564.
7. J. Boussinesq, in "Applications des Potentiels a l'étude de équilibre et du mouvement des solides élastiques", (Gauthier-Villars, Paris, 1885).
8. I. N. Sneddon, *International Journal of Engineering Science* 3 (1965) 47.
9. J. W. harding, I. N. Sneddon, *Proceedings of Cambridge Philosophical Society* 41(1945) 12.
10. G. M. Pharr, W. C. Oliver, F. R. Brotzen, *Journal of Materials Research* 7(1992) 613.
11. K. L. Johnson, in "Contact Mechanics", (Cambridge University Press, Cambridge, 1985).
12. H. Hertz, *J. reine und angewandte Mathematik* 92 (1882) 156.
13. A. C. Fishcher-Crippes, in "Introduction to Contact Mechanics",1st edition, (Springer Verlag, 2000).
14. C. S. Chang, *Dissertation Abstracts International (USA)* 52 (1992) 206.
15. G. E. Dieter, in "Mechanical Metallurgy", 3th edition, (McGraw-Hill, New York, 1986).

Part Seven: The Mechanical Properties and Thermal Stability of Cr-Cr_3Si Eutectic Composites

Even without the additional strengthening effect of the composite, many intermetallic compounds by themselves offer high strength and good creep resistance at elevated temperatures. Combining them with a ductile phase to produce "ductile-phase-toughened" in-situ composites has thus been the focus of attempts to improve the damage tolerance of high-temperature intermetallics at low temperatures. In this part, the mechanical properties of the individual lamellae are examined by nanoindentation. The fracture toughness of the Cr-Cr_3Si eutectic as well as the individual phases that form this eutectic (Cr_3Si and Cr-rich solid solution) are examined by three-point bend testing. In addition, the thermal stability of the lamellar structure is discussed in the last section.

7.1 The hardness and elastic modulus of individual lamellae in Cr-Cr_3Si eutectics

The hardness and elastic modulus of individual lamellae in directional solidified Cr-Cr_3Si alloy were measured by nanoindentation under a maximum load of 16 mN. Forty-five nanoindentations were performed in a 9×5 array with indent spacings of 10 μm, as shown in Fig. 7-1a. After nanoindentation, the hardness impressions were photographed in a microscope and then marked 1, 2, 3 …to 45 in the same sequence as in the nanoindentation testing. Figure 7-1a shows that several indents fall entirely with one of the two phases (e.g., indents 2, 5, 28 etc. are located in the Cr_3Si phase, and indents 10, 15, 22 etc. are in the Cr-rich solid solution). For the same load, the indent impression in the Cr_3Si phase is much smaller than that in the Cr-rich phase indicating that the former is much harder than the latter. Their load and displacement (*P*-*h*) curves during a complete loading and unloading cycle are shown in Fig. 7-1 b and c for the Cr_3Si and Cr-

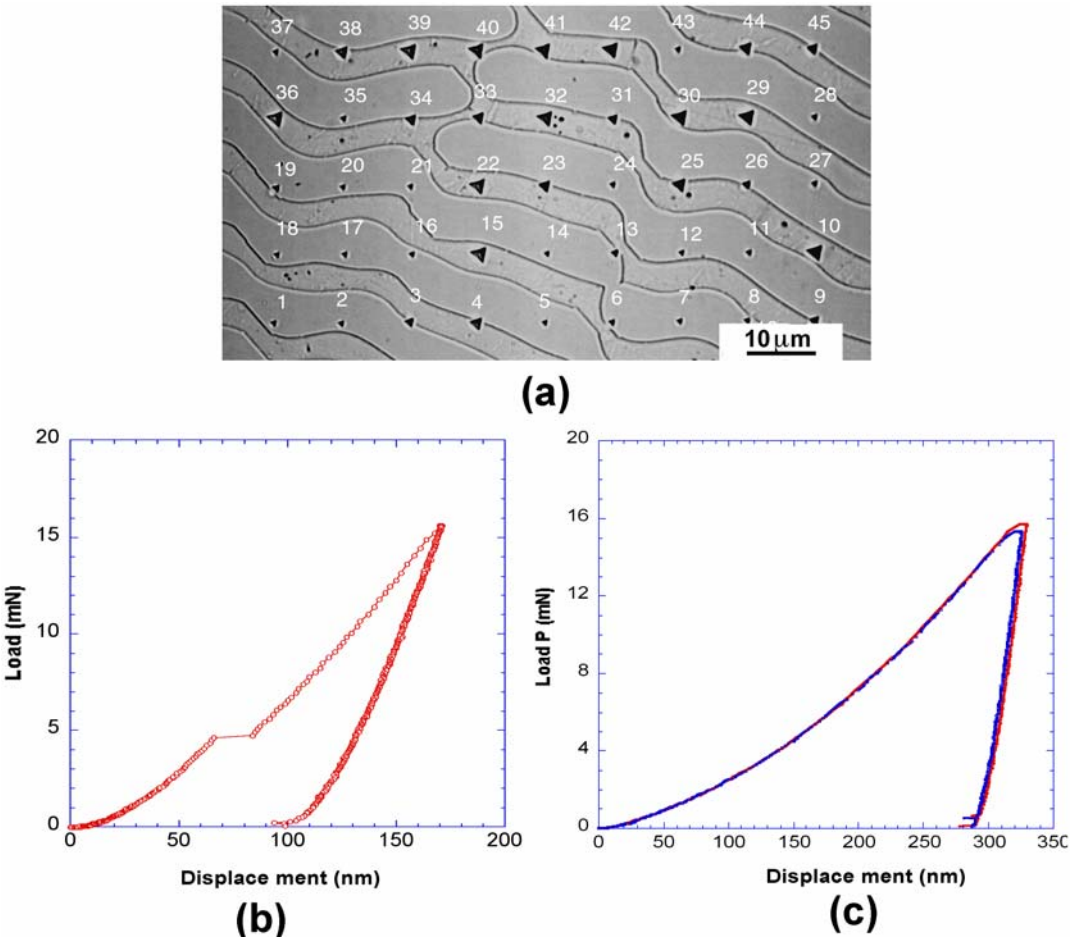

Figure 7-1. Nanoindentation of Cr-Cr_3Si lamellar eutectic. (a) Optical micrographs showing the locations of the nanoindents in a fully lamellar structure of directionally solidified Cr-Cr_3Si eutectic alloy; (b) Typical load and displacement curve obtained in the Cr_3Si phase, showing pop-in behavior during loading; (c) Typical load and displacement curve obtained in Cr-rich solid solution, indicating that this phase is softer than the Cr_3Si phase.

rich phase, respectively. At the maximum value of load, 16mN, the penetration depth in the softer Cr-rich phase is about 320 nm, about 2 times deeper than in Cr_3Si. The unloading *P-h* curve clearly shows that the deformation in the Cr-rich solid solution is almost all irreversible (plastic deformation), whereas, a significant fraction of the deformation in Cr_3Si phase is reversible (elastic deformation), indicating that Cr-rich solid solution is softer than Cr_3Si. Note also that pop-in behavior is observed only in the Cr_3Si loading curve (the details of this behavior are discussed in part 6).

The indentation modulus was calculated from the unloading *P-h* curve using Oliver and Pharr's method at a maximum load of 16mN. This results in a maximum indent depth of ~180 nm in the Cr_3Si phase and ~320 nm in the Cr-rich solid solution phase. Poisson's ratio of 0.2 is used in all the calculations. The indentation modulus of Cr_3Si was found to be 369 GPa and that of Cr-rich solid solution 311 GPa. For comparison, nanoindentation testing was also conducted on two single crystals, Cr_3Si and Cr-rich solid solution, using the same maximum load of 16 mN. Although the hardness and modulus for the individual lamellae were computed only from those indents which fall entirely within one or the other of the two phases, it is possible that the hardness values are influenced by the adjacent lamellae, especially in the case of the Cr-rich phase, in which the size of the indents is comparable to the width of to the lamellae. Consistent with this, the nanoindentation hardness of the Cr-rich lamellae is slightly higher that of Cr-rich single crystal (Table 7-1). However, for both indentation modulus and nanoindentation hardness, the values obtained using single crystals agree reasonably well with those obtained from the individual phases in the lamellar microstructure (~10%).

Table 7-1. The hardness and elastic modulus of Cr_3Si and Cr-rich solid solution

	Cr_3Si		Cr-rich solid Solution	
	in lamellar microstructure	single crystal	in lamellar microstructure	single crystal
Nanoindentation Hardness (GPa)	21.6	22.5	5.2	4.6
Vicker's Hardness (HV @500g)	-	1210	-	296
Indentation Modulus (GPa)	369	382	269	273

7.2 The hardness and elastic modulus of Cr-Cr_3Si composites

The hardnesses of the directionally solidified Cr-Cr_3Si composites was examined by Vicker's hardness testing on lamellar microstructures with lamellar spacings ranging from ~1.5 μm to 5 μm. Their hardness versus lamellar spacing is plotted in Fig. 7-2, where the hardness of single crystals of Cr_3Si and Cr-rich solid solution are also plotted for comparison. The hardnesses of the directionally solidified Cr-Cr_3Si composites are independent of lamellar spacing. The value of the composite hardness is found to be a simple mixture of the hardness of the two single crystals Cr_3Si and Cr-rich solid solution, namely:

$$HV^C = V_f^{Cr} \cdot HV^{Cr} + V_f^{Cr_3Si} \cdot HV^{Cr_3Si} \qquad (7\text{-}1)$$

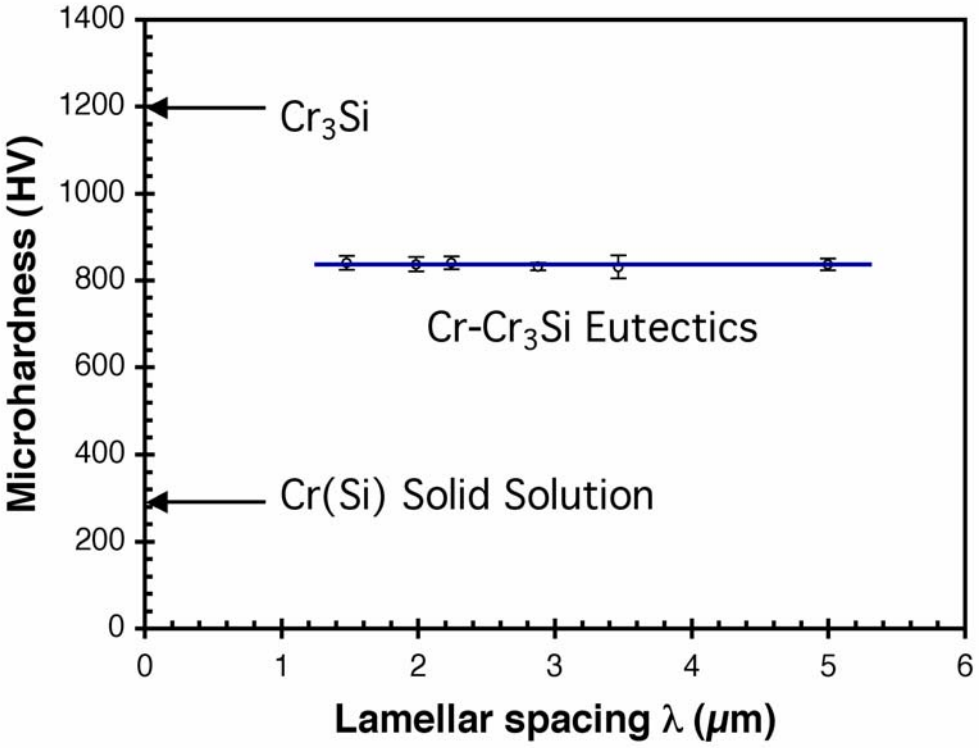

Figure 7-2. The Vicker's hardness of the lamellar Cr-Cr_3Si composite as a function of lamellar spacing. For comparison the hardness of single crystals of Cr-rich solid solution and Cr_3Si are marked as arrows in the figure. All hardnesses obtained at 500g load.

where V_f^{Cr} is the volume fraction of Cr-rich solid solution (0.38), $V_f^{Cr_3Si}$ is the volume fraction of Cr_3Si lamellae (0.62), HV^{Cr} is the Vicker's hardness of Cr-rich solid solution (296), and HV^{Cr_3Si} is the Vicker's hardness of Cr_3Si. Using these data, the composite hardness HV^{C} calculated from Eq. 7-1 is HV860, in good agreement with the experimental observation (HV847±17).

Some interesting observations were made concerning the deformation and cracking behavior during Vicker's indententation. As shown in Fig. 7-3a, the brittle Cr_3Si lamellae cracked whereas the more ductile Cr-rich lamellae deformed plastically. Furthermore, there was no sign of cracking in the direction parallel to the lamellae, indicating that the lamellar interface is not weakly bonded. Collectively, these preliminary results indicate that the toughness of the Cr-Cr_3Si lamellar structure may be better than that of single phase Cr_3Si (Fig. 7-3b) where extensive cracking after indentation was observed, and that the Cr-rich lamellae are effective in stopping cracks nucleated in the brittle Cr_3Si phase.

The Young's modulus of the directional solidified Cr-Cr_3Si composite can be predicted if the volume fraction and elastic modulus of each individual phase is known.For lamellar microstructures, the elastic modulus depends on the lamellar orientation. If all the lamellae in the composite are assumed to be perfectly parallel, the elastic modulus along the lamellar direction is called the Voigt average modulus (iso-strain), E_v [1], given by:

$$E_v^C = V_f^{Cr} \cdot E^{Cr} + V_f^{Cr_3Si} \cdot E^{Cr_3Si} \qquad (7\text{-}2)$$

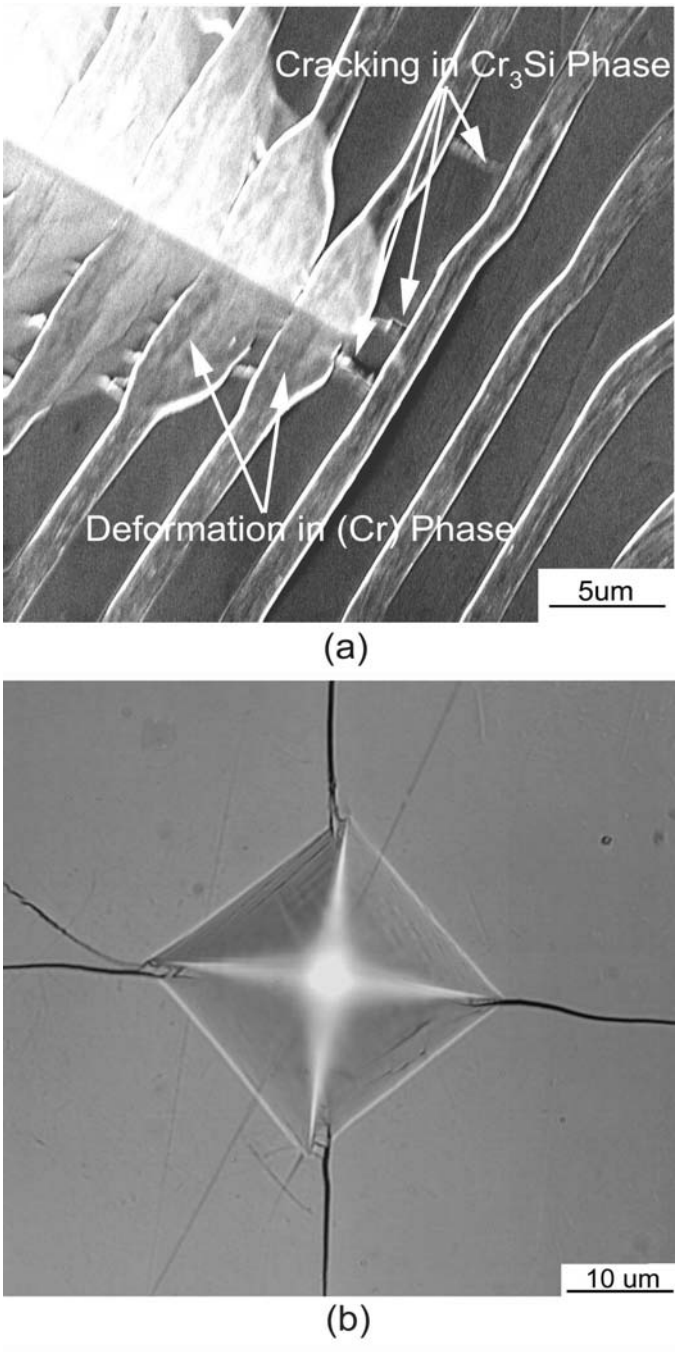

Figure 7-3. Micrographs showing: (a) cracks in Cr_3Si lamellae stopped by the Cr-rich lamellae, and (b) cracks in Cr_3Si single crystal.

where E^{Cr} is the elastic modulus of the Cr-rich solid solution (~269GPa, as shown in Table 6-1), and E^{Cr_3Si} is the elastic modulus of Cr_3Si (~369 GPa). The Voigt average modulus of the composite is therefore 328 GPa.

The elastic modulus perpendicular to the lamellar direction is called the Reuss average modulus (iso-stress), E_R [1], given by:

$$\frac{1}{E_R^C} = \frac{V_f^{Cr}}{E^{Cr}} + \frac{V_f^{Cr_3Si}}{E^{Cr_3Si}} \qquad (7\text{-}3)$$

Therefore, the Reuss average modulus of the composites is 321 GPa. The elastic modulus of randomly oriented lamellar composites is expected to be between these two values 321~328 Gpa.

The Young's modulus of the Cr-Cr_3Si eutectic composites along the growth direction was measured by the ultrasonic technique and found to be 312 GPa, which is reasonably good agreement with the nanoindentation results (within ~5%).

7.3 The fracture toughness of Cr-Cr_3Si composites

The fracture toughnesses of the Cr-rich solid solution, the Cr_3Si intermetallic, and the Cr-Cr_3Si composites were measured by three-point bend test using chevron-notch specimens. Stable crack propagation occurred in all the Cr-Cr_3Si composites and Cr-rich solid solution specimens, but not in the Cr_3Si single crystal specimen in which cracks propagated catastrophically. Figure 7-4 shows a typical load and load point displacement curve. The fracture toughness, $K_{IC,}$ is essentially a measure of the absorbed energy during

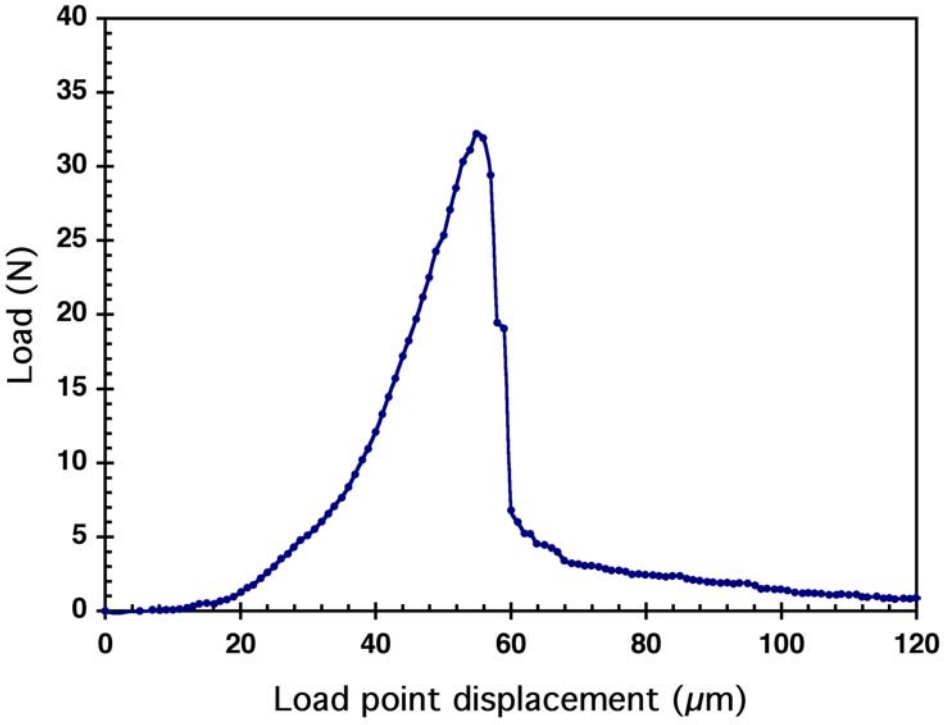

Figure 7-4. Load and load point displacement curve of directionally solidified Cr-Cr_3Si eutectic with lamellar spacing of about 2 μm.

crack propagation given by the area under the load and load point displacement curve in Fig. 7-4. There are several methods to compute the fracture toughness [2-4] using bend tests of chevron-notched specimens. One of these methods relates the fracture toughness to the strain energy release rate, G_{IC}, given by [2]:

$$G_{IC} = \frac{W_f}{A_f} \tag{7-4}$$

where W_f is the absorbed energy (area under the load-load point displacement curve), and A_f is the area swept by the crack. and The fracture toughness is related to the strain energy release rate by [3]:

$$K_{IC} = \left(G_{IC} \cdot E^*\right)^2 \tag{7-5}$$

where E^* is the plane strain Young's modulus given by:

$$E^* = \frac{E}{1-\upsilon^2}. \tag{7-6}$$

A summary of the fracture toughness measurements at room temperature is given in Fig. 7-5. The fracture toughness of single crystal Cr_3Si is very low (~2.6 MPa√m). Combination with a more ductile phase (Cr-rich solid solution) to make a "ductile phase toughened" composites does increase the fracture toughness to some extent. In this study, the maximum fracture toughness of the composite is observed to be 8.5 MPa√m, approximately three times higher than that of single crystal Cr_3Si. This increase in fracture toughness can not be explained by a simple rule of mixtures, which gives a value of only 4.1 MPa√m. The difference is greater than can be explained by simple deviations from the rule of mixtures and suggests that, during fracture of the composites, the

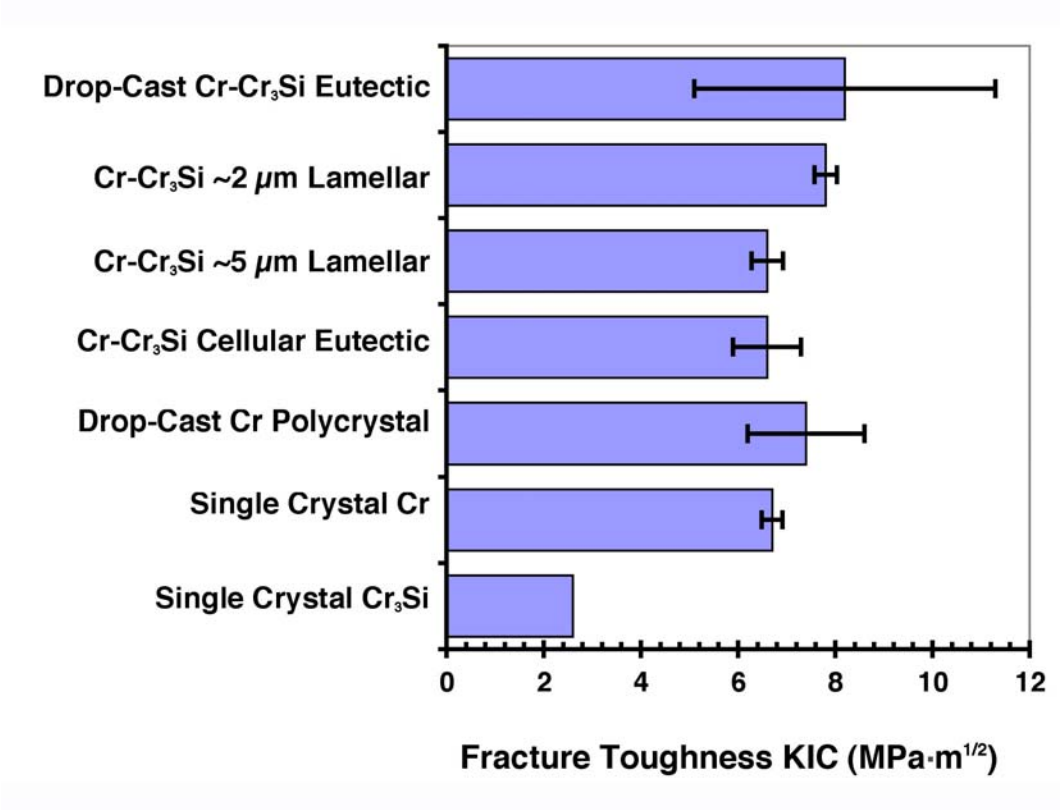

Figure 7-5. Fracture toughness, K_{IC}, of Cr-rich solid solution, single crystal Cr_3Si and Cr-Cr_3Si eutectic.

interfaces may play an important role in absorbing fracture energies. There are several mechanisms to account for this increase in fracture toughness, such as interfacial debonding, pull-out of the debonded lamellae, crack bridging [6,7], etc. Regardless of which of these mechanisms is operating, increasing the number of interfaces (i.e., decreasing the lamellar spacing) is expected to increase the fracture toughness. Consistent with this, Fig. 7-5 shows that the fracture toughness of the lamellar microstructure with spacing ~2 μm is 8.1 MPa√m, which is slightly higher than that of the microstructure with spacing ~5 μm (6.5 MPa√m). In this study, the highest fracture toughness is observed in the drop-cast microstructure, probably because drop cast alloys have the finest structures due to their faster cooling rates. However, the fracture toughness data for the drop cast alloys show more scatter than those for the directionally solidified alloys. A possible explanation for this is that the drop cast alloys have randomly oriented microstructures, in contrast to the well-aligned microstructures in the directionally solidified alloys. Another reason may be that there are more defects (e.g., micro cracks) in the drop-cast alloys.

Fracture surfaces were examined by scanning electron microscopy. Figure 7-6 shows fracture surfaces of single crystal Cr_3Si and Cr-rich solid solution. As can be seen in Fig. 7-6 (a), the fracture surface of the Cr_3Si single crystal is extremely smooth and no features are observed except for some small debris created during the fracture process. In contrast, the Cr-rich solid solution (Fig. 7-6 b) shows steps on its cleavage fracture surface, consistent with its higher toughness compared to Cr_3Si.

Some interesting observations were made when the fracture surfaces of the

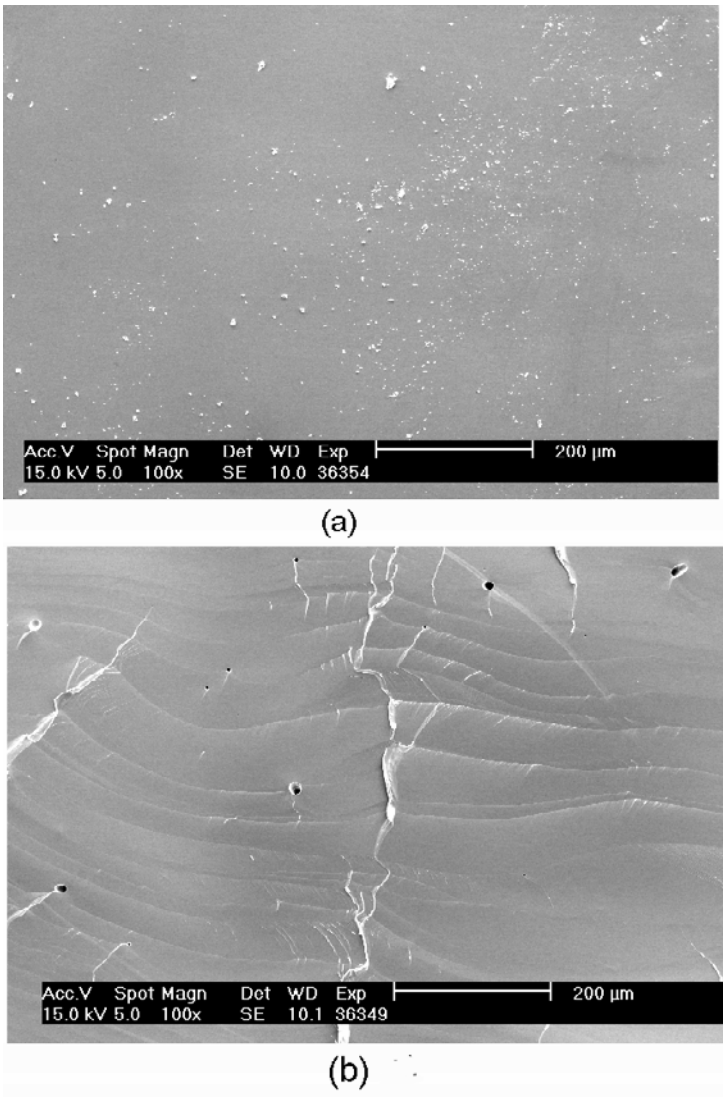

Figure 7-6. Fracture surfaces of (a) single crystal Cr_3Si, and (b) (Cr) single crystal.

directionally solidified Cr-Cr_3Si composites with lamellar spacings of ~5 μm and ~2 μm were examined (Fig. 7-7). As can be seen in this figure, the smooth appearance of the Cr_3Si phase is not different in these two composites. However, the Cr-rich solid solution shows considerably more plastic deformation in the fine lamellar structure (~2 μm) (Fig. 7-7 a) than in coarse lamellar structure (~5 μm) (Fig. 7-7 b). This observation is consistent with the slightly higher fracture toughness of the fine lamellar structure compared to coarse lamellar structure. However, the fracture toughness of this composite is still very low and limits its potential as a structural material.

7.4 Thermal stability of lamellar microstructures

For high-temperature structural applications, the upper temperature limit imay be dictated by microstructural coarsening of the alloys. Since the directionally solidified intermetallic composites discussed in this thesis are being considered for such applications, it is important to consider their stability at elevated temperatures. When compared to arc-melted and drop-cast eutectic alloys, the microstructures of their directionally solidified counterparts tend to be much more stable. One possible reason is that directional solidification occurs very slowly—in hours rather than in seconds as is the case during drop casting—thereby giving time for the structure to approach equilibrium. In addition, during directional solidification, the total energy can be minimized if the two phases adopt low-energy orientation relationships relative to each other. Previous studies have shown that special orientation relationships do exist in most eutectic systems, although the relationships may not be unique. In the Cr-Cr_3Si eutectic

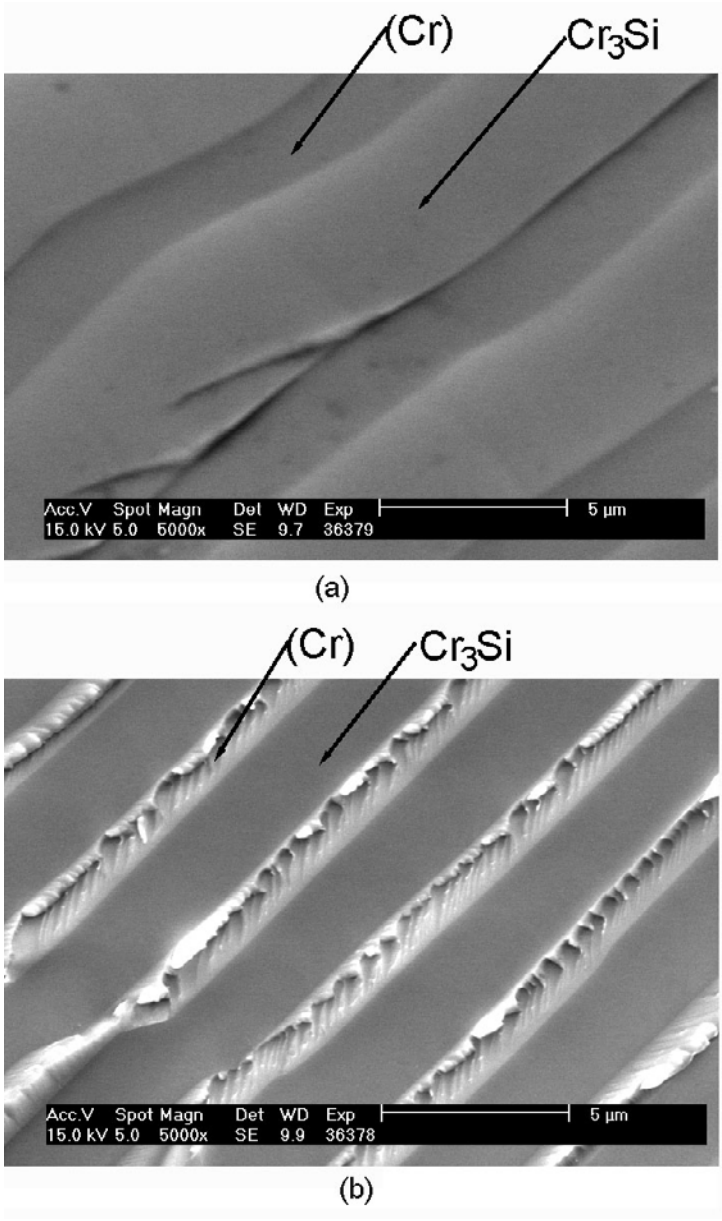

Figure 7-7. Fracture surfaces of directional solidified Cr-Cr_3Si composites with lamellar spacings of (a) ~5 µm, and (b) ~2 µm.

system, for example, four different orientation relationships have been identified In general, the directions and planes tend to be low index. The special orientation relationships are expected to decrease the interfacial energy between the phases, thereby increasing the thermal stability of the eutectic structure.

Figure 7-8 shows the coarsening behavior of a Cr-Cr_3Si eutectic alloy after annealing at 1200ºC. The lamellar structure of the drop-cast alloy (Fig. 7-8a) spheroidizes completely after a 120 h anneal (Fig. 7-8b). In contrast, no visible structural change was observed for a directionally solidified alloy even after much longer annealing times at the same temperature (e.g., 1728 h as shown in Fig. 7-8c).

The driving force for coarsening and spheroidization is the decrease in the total interfacial energy, which is the product of the interfacial area and the unit interfacial energy. Lowering either parameter can slow down the coarsening kinetics. However, the former approach (i.e., make the lamellae or fibers thicker to start with) may compromise mechanical properties because for most materials strength and toughness are likely to be better when the structures are fine. Therefore, decreasing the unit interfacial energy becomes an important way to improve the thermal stability of the eutectic structure. This can be accomplished by microalloying with misfitting elements that segregate to the interphase boundaries and lower their energies.

In binary systems, there is an inverse correlation between solid solubility andgrain boundary segregation potency [8,9]. Solid solubility in turn decreases as the atomic size misfit between the solute and solvent increases (e.g., the Hume-Rothery rules preclude significant solid solubility when the size misfit exceeds 15%). Therefore, elements with

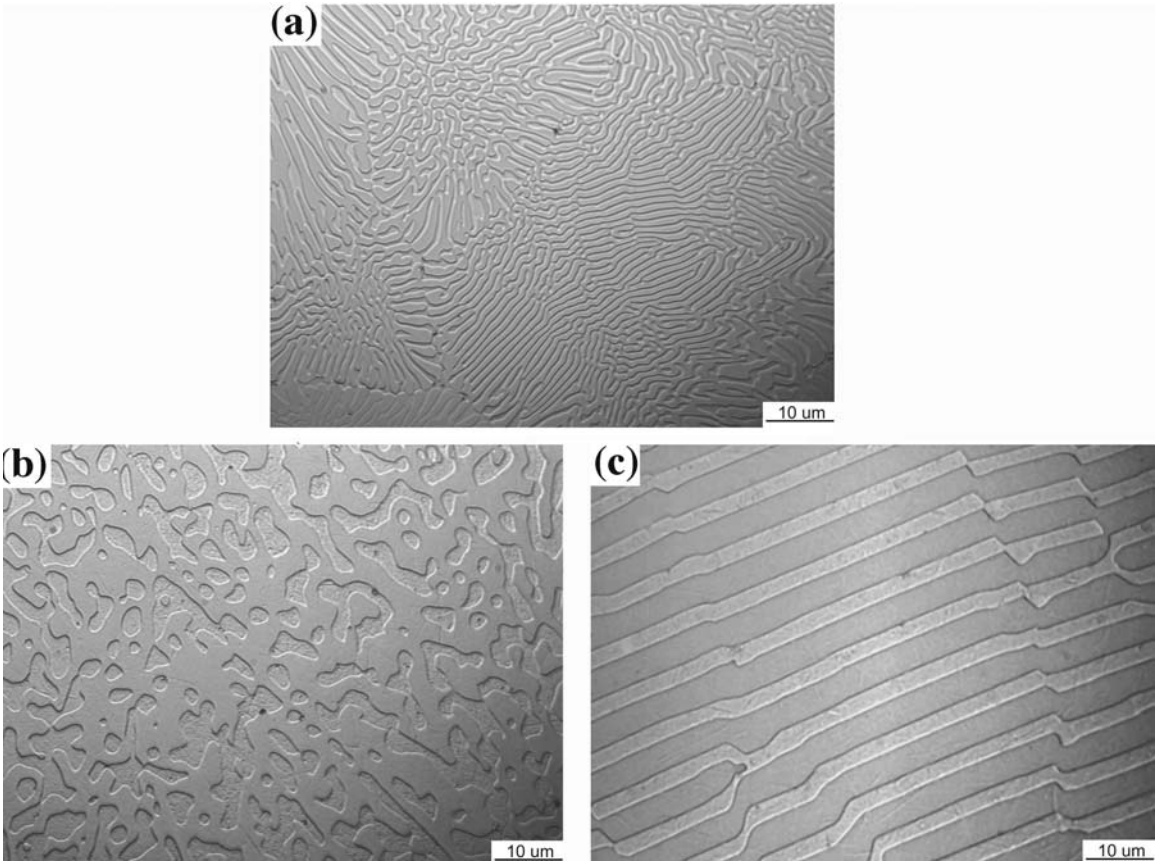

Figure 7-8. Optical micrographs showing coarsening behavior of the lamellar structure of Cr-Cr_3Si alloy after annealing at 1200 ºC: (a) the lamellar structure of the drop cast alloy before annealing, (b) the structure of the drop cast alloy spheroidized after a 120 h anneal, and (c) no visible structure change for a directionally solidified alloy after 1728 h annealing.

large size misfits are expected to segregate strongly to grain boundaries [10]. Similar trends are expected to hold also for interfacial segregation in eutectic alloys. Limited experimental results [11] in the Cr-Cr_3Si eutectic system confirm the above reasoning. It is found that the addition of very small amounts of alloying elements with large size misfits (e.g., Ce and Zr) slow down the coarsening kinetics significantly and improve the thermal stability of the lamellar eutectic structure.

In summary, directional solidification improves the thermal stability of the eutectic structure when compared to that produced by conventional casting. The stability may be further improved by adding very small amounts ("ppm levels") of microalloying elements that segregate to the interphase boundaries and lower their energies.

7.5 Conclusion

The hardness of directionally solidified Cr-Cr_3Si composites is independent of lamellar spacing in this investigation. The predicted value of the composite hardness (HV860) by a simple rule of mixtures of the hardnesses of the two constituent phases, agrees with the experimentally measured hardness of the composite (HV847±17). Vicker's hardness testing indicates that the toughness of the Cr-Cr_3Si lamellar structure is better than that of single phase Cr_3Si, and that the Cr-rich lamellae are effective in stopping cracks nucleated in the brittle Cr_3Si phase.

The Young's modulus of the Cr-Cr_3Si eutectic composites was measured by the ultrasonic technique and found to be 312 GPa, which is reasonably good agreement with the nanoindentation results (within ~5%).

The fracture toughness of single crystal Cr_3Si is very low (~2.6 MPa√m). Combination with a more ductile phase (Cr-rich solid solution) to make "ductile phase toughened" composites does increase the fracture toughness to some extent. In this study, the maximum fracture toughness achieved for the composite is 8.5 MPa√m, The fracture toughness of the lamellar microstructure with fine spacings is slightly higher than that of the microstructure with coarse spacing.

Directional solidification improves the thermal stability of the eutectic structure when compared to that produced by conventional casting. The stability can be further improved by adding very small amounts ("ppm levels") of microalloying elements that segregate to the interphase boundaries and lower their energies.

References:

1. G. E. Dieter, in "Mechanical Metallurgy", 3th edition, (McGraw-Hill, New York, 1986).
2. I. Merkel, U. Messerschmidt, *Materials Science and Engineering A* 151(1992) 131.
3. A. G. Atkins, Y. W. Mai, in "Elastic and Plastic Fracture", (John Wiley & Sons, New York, 1976).
4. D. Munz, R. T. Bubsey, J. L. Shannon, *Journal of American Ceramic Society* 63(1980) 300.
5. D. Munz, J. L. Shanon, R. T. Bubsey, *International Journal of. Fracture* 16(1980) R137.
6. B. Derby, D. A. Hills, C. Ruiz, in "Materials for Engineering: A Fundamental Design Approach", (John Wiley and Sons, Inc, New York, 1992).
7. H. Choe, D. Chen, J. H. Schneibel, R.O. Ritchie, *Intermetallic* 9(2001) 319.
8. M. P. Seah and E. D. Hondros, *Proc. Roy. Soc. A* 335 (1973) 191.
9. E. D. Hondros and M. P. Seah, *Scripta Metall.* 6 (1972) 1007. 24.
10. F. Laves, in "Theory of Alloy Phases", (American Society for Metals, Cleveland 1956), p. 124.
11. E. P. George, H. Bei, K. Serin, G. M. Pharr, *Materials Science Forum*, 426-432(2003) 4579.

Part Eight: Summary and Future Work

Directional solidification allows the production well-aligned lamellar or rod-like microstructures of Cr-Cr_3Si eutectics. The interphase spacing and the volume fractions of the constituent phases can be controlled by adjusting the solidification conditions and alloy compositions. The biggest drawback of these alloys is poor ductility and low fracture toughness under ambient conditions. Combination with a more ductile phase (Cr-rich solid solution) to make "ductile phase toughened" composites does increase the fracture toughness to some extent. However, the fracture toughness of this composite is still very low and limits the structural applications of the material. Additional work is needed to identify and understand alloying effects on strength, toughness, microstructural stability and oxidation resistance.

Vita

Hongbin Bei was born on November 28, 1969 in Zhejiang, China. He studied for four years at Beijing University of Aeronautics and Astronautics (BUAA), and got his Bachelor's degree in Engineering in 1991. From 1991 to 1994, he studied at the General Research Institute for Non-ferrous Metals (GRINM), Beijing, China, and got his Master's degree following which he worked as an assistant engineer and a engineer from 1994 to 2000.

He studied at The University of Tennessee (UTK) for his doctoral degree from August 2000 to December 2003, and was a graduate research assistant during that period.

He is a student member of the American Society for Materials and Materials Research Society.